MODELLING THE ONSET OF DYNAMIC FRICTION
Importance of the Vertical Dimension

by

JØRGEN TRØMBORG

THESIS

for the degree of

MASTER OF SCIENCE

(Master i Fysikk, studieretning Computational physics)

Faculty of Mathematics and Natural Sciences
University of Oslo

June 2011

Det matematisk-naturvitenskapelige fakultet
Universitetet i Oslo

Abstract

The last decade has seen major advances in the experimental study of the onset of dynamic friction. Optical methods give access to the sliding interface before and during sliding onset, enabling characterisation of the *local* response to external shear. Treating the sliding interface as an extended system, experimentalists have probed the evolution of slip with high spatial resolution. Cameras operating at the order of 100 kHz have enabled direct study of the fast crack/rupture fronts associated with the transition from local pinning to shear displacement.

The spatiotemporal resolution goes beyond the phenomenological descriptions of the *global* frictional response, i.e. the net resistance to shear motion. Models of the friction of extended systems have a longstanding history in the earthquake community and as models of global friction motivated by the microscopic formation and breaking of contacts. Some of these models have been adapted to the study of sliding onset and investigated numerically. However, their quantitative predictive power has been poor.

In this thesis I study deterministic spring–block models of an elastic slider under dry friction. I apply Amontons–Coulomb friction at the block level. First, I study a one-dimensional model and investigate the length of precursors as a function of the driving force. Analytical expressions for point and uniform driving are found and shown to be in excellent agreement with simulation results. Qualitative agreement with experiments is demonstrated. The effect of a friction-induced torque is studied for uniform driving, and the output form the model is compared to a recently proposed theory.

I then study a two-dimensional model that includes the direction of sliding and the direction out of the sliding plane, the vertical. By comparison to the one-dimensional model, I show that successful prediction of the experimental results depends crucially on accurate representation of the forces associated with elastic deformations of the slider. This can be obtained in the two-dimensional model if realistic boundary conditions are applied.

The statics of sliding onset are the measures that correspond to the states the sliding system comes to rest in, for example the arrest point of a local slip zone, the interfacial shear and normal stress profiles and the length and number of precursors. The dynamics of sliding onset are the rapid time dynamics, for example the speed of the front of a growing slip zone. The statics are reproduced remarkably well in my two-dimensional model, while the dynamics still lack important features of the experimental results. This indicates that the statics depend only weakly on the dynamics, and that they could be studied independently of the fast time evolution. Conversely, the dynamics, although not reproducing the range of experimental observations, are shown to depend strongly on the local stresses and the details of the friction law, i.e. cannot be predicted independently of the statics.

Acknowledgements

I remember discussing possible thesis topics with Professor Anders Malthe–Sørenssen on many occasions before as well as after he became my supervisor. A point he often made was that he prefers groups of students to work on closely related topics, because this gives the best results. The actual topic is less important, he would say, because you are not bound to it afterwards. No one requires you to keep working on it after you finish your degree.

Eventually, we settled on friction, and for a year I have had the pleasure of collaborating with David Skålid Amundsen and Kjetil Thøgersen. David and I started our bachelor's degrees at the same time, and we have been learning physics together for nigh on five years. Kjetil and I had our first courses together at the start of our master's studies two years ago. For the thesis work, the three of us have been sharing an office. Valuable opinions on findings, alternative solution strategies for problems and suggestions for new lines of investigation have been shared freely by both, and I have benefited greatly from our conversations.

Almost from the start, Doctor Julien Scheibert has been part of our frequent meetings with Anders. We are all indebted to him for his willingness to discuss and consider the tiniest details, his mental library of the friction literature and his experimentalist viewpoint. I was pleased to hear that he too would be listed as my supervisor.

I am grateful to Anders for his extensive advice on the thesis, on careers within and outside of academia and on life in general.

Finally, to friends, family and my love, Anette: thank you for your support and for taking my mind off friction when I need it.

Oslo, 1 June 2011
Jørgen Trømborg

Preface

As mentioned in the acknowledgements, I carried out the research for this thesis in collaboration with two other master's students, David Skålid Amundsen and Kjetil Thøgersen. Initially, David, Kjetil and I studied the same model, which is the 1D model that we all present in our theses. It was clear from the beginning that we would work on closely related, but distinct, models; the simple form of the 1D model served as a common point of reference and as a stepping stone for identifying interesting lines of investigation.

An obvious way to branch out was to extend the model from 1D to 2D, either by including the whole sliding plane, or by including the sliding and out-of-plane directions. I have studied the latter option. David has studied the 2D model of the whole sliding plane; he is also the one to have pursued the 1D model the furthest of us. His thesis shares the title of mine, as does Kjetil's, and has the subtitle *A study of rupture velocities* [1]. Kjetil has adapted the model to the microscopic scale, and studied the shearing properties of rough surfaces. The subtitle of his thesis is *Contact mechanics* [54]. Both theses are available through the University of Oslo's digital repository at `http://duo.uio.no`.

The research article [56] is based on the main findings in this thesis, which I will also present at the Gordon Research Conference *Adhesion, Science of* in July 2011.

Contents

List of symbols

η	Coefficient of damping	50
μ_k	Coefficient of dynamic/kinetic friction	
μ_s	Coefficient of static friction	
μ_s^{global}	Global coefficient of static friction	64
ν	Poisson's ratio	26
σ	Normal stress	25
τ	Shear stress	26
θ	Parameter controlling non-uniformity of normal load	50
ξ_μ	Characteristic length in slip weakening friction laws	115
A	Geometric/apparent contact area	26
A_{real}	Real area of contact	26
B	Breadth of slider	48
E	Young's modulus	25
f_i	Friction force on node i	50
F_X	External shear force	21
F_Z	Normal force on top of slider, in equilibrium equal and opposite to W	32
g	1D: parameter controlling the friction-induced torque	67
H	Height of slider	48
h	Pushing height where F_X is applied	66
i, j	Discretisation indices, $i = \sqrt{-1}$ when this is clear from the context	
K	Stiffness of the driving spring	22
k	1+1D: stiffness of horizontal and vertical springs connecting nodes	75
k	1D: stiffness of springs connecting nodes	49
$\bar{K}$	1D: stiffness of spring connecting each node to driving plate	65
k_{ps}	1+1D: stiffness of bottom potential surface	83
L	Length of slider	48
l	Distance between neighbour nodes	75
L_p	Length of precursor	37
M	Mass of slider	49
m	Mass of a node	49
N	1D: number of blocks	49
N_{sliding}	Number of nodes sliding at any given time	53
N_p	Number of precursors	94
N_x, N_z	1+1D: number of nodes in x- and z-directions	76
t	Time	
Δt	Time step length	
V	Driving speed of the trailing end of the driving spring	22
v	1D: local sliding velocity, $v_i = \dot{x}_i$	61
v_{crack}	Velocity of crack/rupture front	39

W	Normal force on slider from track, in equilibrium equal and opposite to F_Z	21
w_i	Normal force on node i	50
x	1D: position of node relative to its position in the unstrained chain	50
x, y, z	Experiment: external shear, transverse and normal load directions	33
x, z	1+1D: external shear and normal load directions	76

Chapter 1

Introduction

1.1 The physicist's toolbox

Physics is the study of the mathematical relationships in nature; a physicist seeks to express his findings in the language of mathematics. Doing physics is a bridging process: on one side is nature, from which stems the observations that theory seeks to explain and predict. On the other side are the theories, cast in mathematical form. Physics is about developing and testing these theories, and it is about using them to gain insight into the natural processes that they describe. To do this, the physicist employs a number of tools: experiments, hand calculations and the computer.

Nature is a messy system to study. Typically, something happening in nature involves a lot of physical processes. Bird flight, for instance, at the least involves gravity, mechanics, fluid mechanics, electromagnetism and thermodynamics. Trying to puzzle out what is going on directly is a hopelessly complicated task. *Experiments*, therefore, are constructed in such a way as to isolate the physical processes from each other. To understand gravity you don't study a bird in flight, you study the fall of simple objects and the motion of the planets.

Hand calculations retain their importance even as computers become abundantly available. Performing calculations by hand gives you a unique feel for the underlying mathematics. Quite apart from the fact that computers did not exist when much of physics was discovered, one might suspect that the beautiful simplicity of theories like Newton's mechanics and Maxwell's electromagnetism was made possible by the mathematical intuition that hand calculations help build.

The *computer* is used in both the predicting-system-behaviour and abstraction-to-theory forms of physics. For instance, it allows solution of otherwise intractable equations and performing calculations that would take too long by hand. Theory development can be aided by identifying patterns in large amounts of experimental data. Gould et al. [30] give the following useful categorisation of the ways in which the computer is used in physics.

- *Numerical analysis* is the solution of well-defined mathematical problems to produce numerical (in contrast to symbolic) solutions.

- *Symbolic manipulation* software can perform operations like differentiation, integration, matrix inversion and power series expansion, returning exact symbolic solutions.

- *Visual representation* of complicated numerical data sets and symbolic expressions can increase the understanding of results.
- *Computer simulation* is used to study the behaviour of a model. Simulations frequently use numerical analysis and visualisation, and sometimes symbolic manipulation. While the above three are usually used in a given-the-question-produce-the-answer work mode, simulation describes more exploratory study where new questions arise as the work progresses.
- *Collection and analysis of data* and *real-time control* using one or more computers are important in the instrumentation of many experiments.

This thesis is a computer simulation project which uses all of the above tools. Albeit I have not performed any experiments myself, the link to recent experimental advances is strong: I seek to model a series of friction experiments that have been published in the last few years. Simulation is used to investigate the behaviour of the models I make, and insight from these investigations is used to modify the models. Sometimes these modifications enhance the agreement with experiment and are kept; sometimes they do not and are discarded. Hand calculations are used during implementation and analysis.

1.2 The science of friction

The force resisting relative motion of solid surfaces is called *friction*. It is a macroscopic quantity that lumps the effects of a number of microscopic processes into a single term. Friction has enormous practical interest because of the ubiquity of solid surfaces in actual or potential relative motion. It is part of the wider field *tribology*, which is the science and technology of interacting surfaces in relative motion. In addition to friction, Dawson [23] lists the study of lubricants, lubrication, wear and bearings as examples of fields belonging within tribology. Like friction, all of these are familiar parts of our daily lives, even if we seldom pause to consider them in detail.

By the above definition, tribology and its subject areas are vast fields that are concerned with practically every man-made device. There are moving parts in cars, computers and refrigerators. Over time the moving parts are degraded by wear, which occurs by the plucking off of small parts of the surfaces. Lubrication, which also modifies the friction force, can prolong the lifetime of machines by separating the solid objects from each other. The lubricant is typically a fluid that enters the space between the objects; solid lubricants also exist, e.g. graphite. Further, friction is important in situations where nothing moves: without friction you could not tie your shoes or lean against the wall without falling over. Moreover, tribology is of relevance in biology (e.g. joints), geology (e.g. earthquakes) and fracture mechanics (the fracture creates surfaces that are in contact). Attempting an exhaustive listing of applications is, of course, futile.

The study of friction can be motivated in numerous ways. Dawson makes the interesting observation that whereas sudden failure of machines due to breakage is rare, gradual failure due to friction related wear is nearly universal. We are sophisticated when it comes to the strength of what we create, but less sophisticated when it comes to the lifetime. There is much to gain, economically and environmentally, from reducing the amount of energy and equipment lost to friction and related processes. By understanding friction we can hope to control it.

In this thesis I take the view of fundamental research, that friction is an interesting subject of study in and of itself. There are no immediate technological applications of

my findings. I shall not be dealing with wear, or with lubrication. Rather, my topic is dry friction, i.e. the sliding surfaces are in direct contact, with no lubricant in between. Still an enormous body of theory remains. An important further restriction: I will not be considering the atomic/molecular scale. I could go on narrowing the subject area down bit by bit, but allow me now to invert the perspective and state what I *will* be treating.

My computer simulations have the goal of reproducing the statics and dynamics of recent laboratory experiments on the sliding initiation of the multicontact interface between two elastic blocks. The blocks are of centimetre scale, and the spatial details are on the millimetre scale. The experiments have been carried out on blocks of the same material, poly(methyl methacrylate) (PMMA), but my results should have a more general validity.

1.3 Structure of the thesis

This document is arranged in four parts. Part I opens with an introduction to the established theory of friction, Chapter 2, and continues in Chapter 3 with a summary of the experiments I model and of existing numerical studies of friction. The main body of the document is Part II, which has three chapters. Chapter 4 is concerned with a one-dimensional spring–block model, and in Chapter 5 I extend this model by adding to it the vertical dimension. Chapter 6 is a brief treatment of a simple modification of the local friction law, common to both preceding chapters. A summary of my findings and the conclusions I draw from them are given in Part III, while Part IV contains the appendices.

The layout is adapted to print, i.e. when possible, figures and the text that refers to them appear on the same double page. As the ratio of figures to text is large, this means that occasionally, a figure will appear before the first point in the text where it is mentioned. For the best reading experience on screen, therefore, I recommend displaying the document as it appears in print, i.e. showing pages 2 and 3 together, 4 and 5 together, and so on.

Part I

STATE OF THE SCIENCE OF FRICTION

Chapter 2

Theory of friction

The scientific study of friction has at least two objectives: to quantify the frictional resistance to motion, and to explain it. In this chapter I will introduce the theory of dry friction, treating both quantification and explanation. The theory does not apply to lubricated surfaces, for which the properties of the lubricant are important.

2.1 Empirical friction laws

2.1.1 Amontons–Coulomb friction

Progress at quantifying friction was made by da Vinci, Amontons and Coulomb, centuries apart, and the Amontons–Coulomb friction laws continue to be a successful approximation in a wide range of applications. They are the solid friction theory typically taught in high school and undergraduate university courses. The principal observations are that friction is, perhaps counter intuitively, independent of the geometric contact area between the sliding objects, but is proportional to the normal force between them. Figure 2.1 illustrates the way da Vinci investigated the influence of the geometric contact area.

In modern language (Baumberger and Caroli [4]): when a solid block lying on a track with a nominally planar interface is submitted to a normal force W and a tangential force F_X,

- no motion occurs as long as F_X is smaller than some threshold F_s,

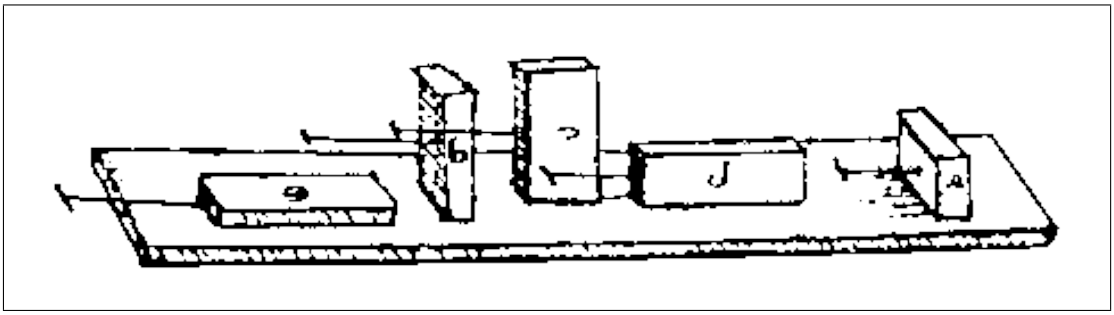

Figure 2.1: Sketch from da Vinci's notebooks showing his investigation of how the frictional resistance to motion depends on the geometric contact area. The friction force is the same for all five orientations of the sliding block.

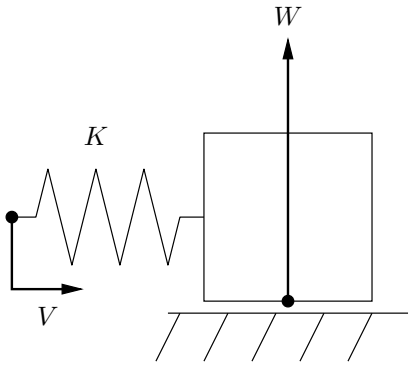

Figure 2.2: A typical friction experiment. The stiffness K can represent an actual spring or an effective stiffness of the loading apparatus.

- sliding is dissipative, and the corresponding dynamic/kinetic friction force F_k is constant,
- the values of F_s and F_k are proportional to W and, for a given W, independent of the macroscopic (apparent) contact area. The frictional behaviour of a couple of materials is characterised by two numbers, the friction coefficients

$$\mu_s = \frac{F_s}{W}, \tag{2.1a}$$

$$\mu_k = \frac{F_k}{W}. \tag{2.1b}$$

Corrections to these laws are numerous, and some of them will be presented in the following section.

2.1.2 Rate and state constitutive laws

Baumberger and Caroli [4] review the present understanding of solid friction. The description stays within the framework of finding a factor of proportionality between the normal load and the friction force, but the friction coefficients are no longer constants. In particular,

- the static friction threshold increases with the time of stationary contact,
- for low sliding velocities, in steady sliding, μ_k depends on the sliding velocity,
- friction depends on the sliding history.

These observations have been made in experiments with sliding systems like the one in Figure 2.2. A block is pushed at the trailing edge by a spring or loading stage of stiffness K, whose free end is driven at speed V. The driving force F_X is the force in the spring. One commonly observes the sliding regimes shown in Figure 2.3. In Figure 2.3a the system enters a steady sliding regime: the block moves at the driving speed and the force in the driving spring equals the dynamic friction force at this driving velocity. Figures 2.3b and 2.3c show dynamic instability: the block alternates between sticking periods in which F_X builds up, and fast sliding events. In experiments the system can be brought into the steady sliding regime by increasing V and/or K. A calculation showing that if friction follows the Amontons–Coulomb laws only regular stick–slip is possible is given in Appendix B.1.

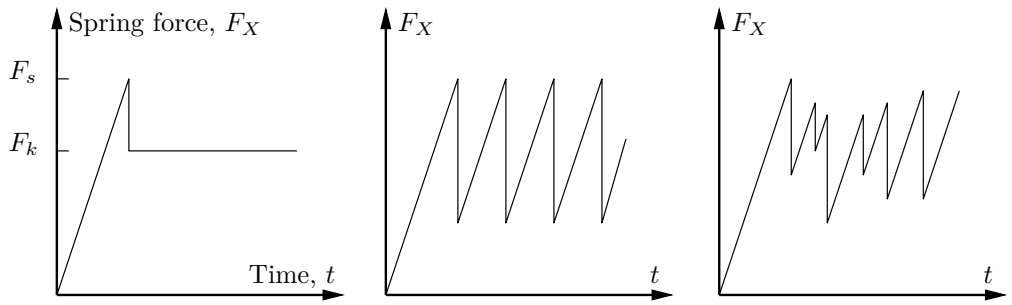

(a) Steady sliding **(b)** Regular stick–slip. **(c)** Chaotic stick–slip.

Figure 2.3: Three different sliding regimes for the system in Figure 2.2. Adapted from Fig. 3.2 of [43].

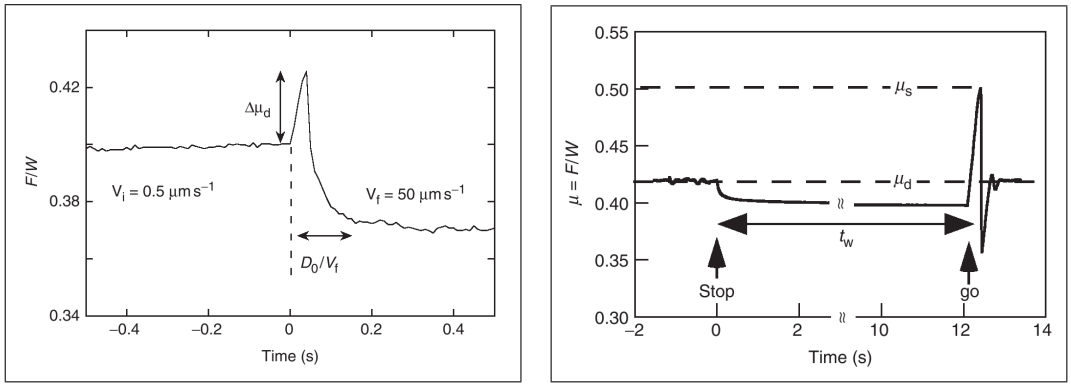

(a) Velocity dependence of kinetic friction in steady sliding. D_0 is a characteristic length of the transient. At $t = 0$, the driving velocity was changed from V_i to V_f.

(b) A stop-and-go experiment. The value of μ_s, taken to be the peak value of μ, depends on the waiting time t_w. The driving velocity is the same before and after the waiting period.

Figure 2.4: F is my F_X, μ_d is my μ_k. The interface is PMMA on PMMA. Taken from Baumberger and Caroli [4].

Figure 2.4a shows clearly that the friction force depends on the driving velocity. In steady sliding, $F_X = F_k$, and since two distinct levels of F_X are observed one concludes that F_k depends on V. The figure also shows that there is a transient response upon increasing V. The system's approach to the new dynamic friction level is controlled by a characteristic length D_0.

A similar type of experiment, aptly named stop-and-go, is shown in Figure 2.4b. While in the steady sliding regime, the driving stage is stopped and held for a controllable time t_w; then, driving is resumed at the same velocity. By varying t_w in a series of stop-and-go experiments, the time strengthening of μ_s can be studied.

The goal of making rate and state constitutive equations is to incorporate the observed frictional behaviour in a single or a few equations, with few adjustable parameters. The *rate* variable is the sliding velocity of the centre of mass, $\dot{x}_{CM}$. The *state* variable often lacks a physical interpretation ([4]). A good review was given by Marone [37], which I follow here.

The idea of rate and state friction laws is attributed to Dieterich [24]. He performed

experiments where the loading rate was systematically varied as in Figure 2.4a, and he investigated the effect of loading rate on static friction in stop-and-go experiments. In modern terms his constitutive equations take the form

$$\mu\left(\dot{x}_{CM}, \vartheta\right) = \mu_0 + \mathfrak{a} \ln\left(\frac{\dot{x}_{CM}}{V_0}\right) + \mathfrak{b}\left(\frac{V_0 \vartheta}{D_0}\right), \tag{2.2a}$$

$$\dot{\vartheta} = 1 - \left(\frac{\dot{x}_{CM}\vartheta}{D_0}\right). \tag{2.2b}$$

Note that for $\dot{x}_{CM} = 0$, $\vartheta = t$, which justifies interpretation of this state variable as a "time-like" variable. The empirical coefficients $\mathfrak{a}$ and $\mathfrak{b}$ are positive and of order 10^{-2}. V_0 is a reference velocity in the range (0.1–100 µm/s).

Ruina [49] analysed Dieterich's and other forms of the evolution of the state variable ϑ. He proposed another form of equation (2.2b), namely

$$\dot{\vartheta} = -\frac{\dot{x}_{CM}\vartheta}{D_0} \ln\left(\frac{\dot{x}_{CM}\vartheta}{D_0}\right). \tag{2.3}$$

Microscopically, the two forms have a different interpretation: Dieterich's form emphasises the average contact lifetime, while in Ruina's form, any change in friction requires slip; however, distinguishing between the laws in the laboratory has proven difficult. According to Scholz [52], the rate and state relationship presently in best agreement with experimental observations is equations (2.2), which is somewhat ambiguously called the Dieterich–Ruina law.

The rate and state friction laws, like the Amontons–Coulomb laws, are macroscopic relationships. The sliding system is assumed to be adequately described by one or a few degrees of freedom. In recent years, experimentalists have probed the details of the processes at the sliding interfaces that are ignored by macroscopic descriptions. I will return to this in Chapter 3. I have not applied rate and state friction laws in this work.

2.1.3 Slip or velocity dependence, ageing

In numerical work it is often desirable to keep the constitutive relations simple. Consequently, in the numerical literature a full rate and state description is often abandoned in favour of simpler relationships that extend the Amontons–Coulomb laws. In slip weakening friction laws the discontinuous transition from static to dynamic friction is regularised by introducing some characteristic distance over which the friction coefficient changes. In Chapter 6 I apply a slip weakening modification of the Amontons–Coulomb laws. In velocity dependent friction laws there can be a similar regularisation dependent on the sliding object's speed, and there can be velocity strengthening regimes, typically for high sliding velocities. For examples of slip and velocity weakening friction laws, see e.g. [20, 28]. Ageing refers to the time strengthening of μ_s, which can also be included in a friction law even if no *rate* dependence is considered.

2.2 Simple theory of linear elasticity

An object subject to friction and other external contact forces does not move as a rigid body. The way the object deforms is the subject of elasticity theory. For the systems I will study, the linear theory will be sufficiently accurate. Even though results and discussions will often be given in the terms of the discrete models I study, i.e. forces

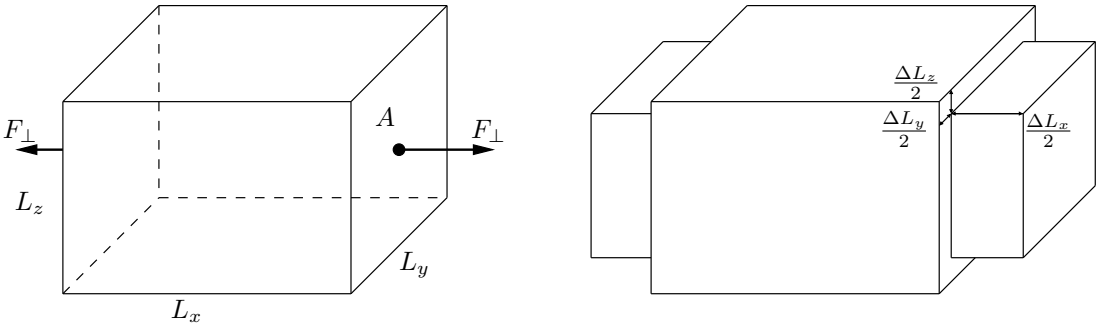

Figure 2.5: A prismatic bar (shown here in a nearly cubic case) under uniform tension $F_\perp$ in the x-direction. The forces act on the entire yz-planes. The left part shows the dimensions of the bar before the forces are applied. The right part illustrates that as the bar becomes longer in tension, the lateral dimensions contract. The strains have been exaggerated for clarity.

and displacements, sometimes it will be useful to express them as stresses and strains. Also, linear elasticity theory is needed in order to determine the relation between model parameters and experimental material properties. Finally, the microscopic theory of friction uses the language of elasticity theory: stress, elastic and plastic material response and material strength are important concepts in the modern understanding of friction. A very brief introduction to the theory of elasticity will be given here; a more extensive treatment can be found in e.g. [55, 59].

2.2.1 Definitions and basic relationships

To introduce the concepts of *stress* and *strain*, consider a prismatic bar submitted to tension by forces distributed uniformly over the ends as shown in Figure 2.5. In general, stress and strain are local quantities, but in this highly symmetric case they will be spatially uniform. Stress is force per area: the normal stress σ equals the normal force $F_\perp$ divided by the cross-sectional area A,

$$\sigma = \frac{F_\perp}{A}. \tag{2.4}$$

Tension is produced by forces acting away from the bar (pull). If the forces act towards the bar (push) the bar is in compression, an example of which is a bar supporting some weight on top, e.g. the legs of a table. As a result of this tension/compression the bar will deform. In linear elasticity the deformation ΔL is assumed to be small compared to the unstressed length L. The strain is the ratio between them:

$$\epsilon = \frac{\Delta L}{L}. \tag{2.5}$$

As long as linear elasticity theory is obeyed, there is a linear relation between the stress and the strain, this is known as Hooke's law. The modulus E of elasticity in tension/compression is called Young's modulus and is given by

$$E = \frac{\sigma}{\epsilon} = \frac{F_\perp}{A}\frac{L}{\Delta L}. \tag{2.6}$$

For many materials the value of E is the same in tension and compression; concrete is a well known exception.

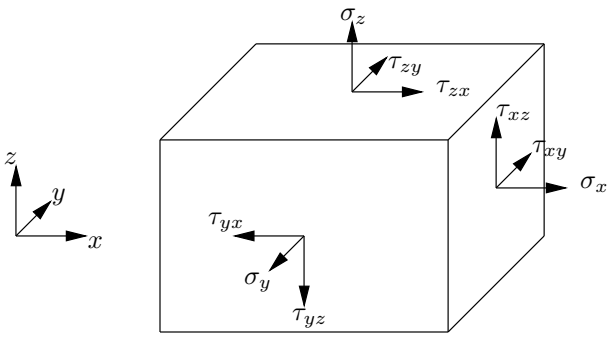

Figure 2.6: The components of stress. The positive directions are parallel to the coordinate axes if the surface normal is along the positive axis, and reversed if the surface normal has a direction opposite to the positive axis. Adapted from Timoshenko and Goodier [55].

As shown in Figure 2.5 the strain in the direction parallel to the forces is accompanied by lateral strains of opposite sign; as the bar becomes longer in tension, it also becomes thinner. Poisson's ratio ν is the ratio of these strains. If the forces act in the x-direction then

$$\begin{aligned} \nu &= -\frac{\epsilon_y}{\epsilon_x} \\ &= -\frac{\Delta L_y / L_y}{\Delta L_x / L_x}, \end{aligned} \tag{2.7}$$

with ΔL_x and ΔL_y the length changes in the x- and y-directions, respectively. A similar expression holds for the z-direction. If the system is isotropic, ν and E do not depend on the direction of the forces.

In pure tension/compression the forces are perpendicular to the surfaces on which they act, but this need not always be the case. Forces acting parallel to the surfaces give rise to shear stresses and strains. Any inclined force can be decomposed as one normal and two orthogonal shearing forces. If $\hat{\mathbf{e}}_i$ is the normal to the surface, a common notation is to write σ_i for the normal stress and τ_{ij} and τ_{ik} for the two shearing stresses. (Note that the first index is given by the surface normal; the direction of the stress is coded in the second index.) Figure 2.6 illustrates this. Sometimes one defines $\tau_{ii} \equiv \sigma_i$ to facilitate matrix notation and/or the Einstein summation convention.

2.2.2 Plastic deformation

For real materials, the linear relationship between stress and strain is approximately correct for small stresses and strains only. The stress at which proportionality breaks down is called the proportional limit. Beyond this point is the elastic limit or yield stress, up to which the deformations are reversible: if the elastic limit is not exceeded, the material regains its original shape upon removal of the load. If the stress is increased further, the material starts to deform plastically: it no longer returns to its original shape when the load is removed. A sample flowing plastically in tension eventually ruptures.

2.3 Microscopic description (Bowden and Tabor)

The modern understanding of friction is due to Bowden and Tabor [12]. I follow the introduction by Scholz [52]. The crucial point is that *friction is controlled by interactions at the points of intimate contact, whose area A_{real} is proportional to the load W and independent of the geometric contact area A.*

Unless extremely carefully prepared, real surfaces are *rough*: the variation in surface height is large compared to molecular dimensions. When two surfaces are brought into

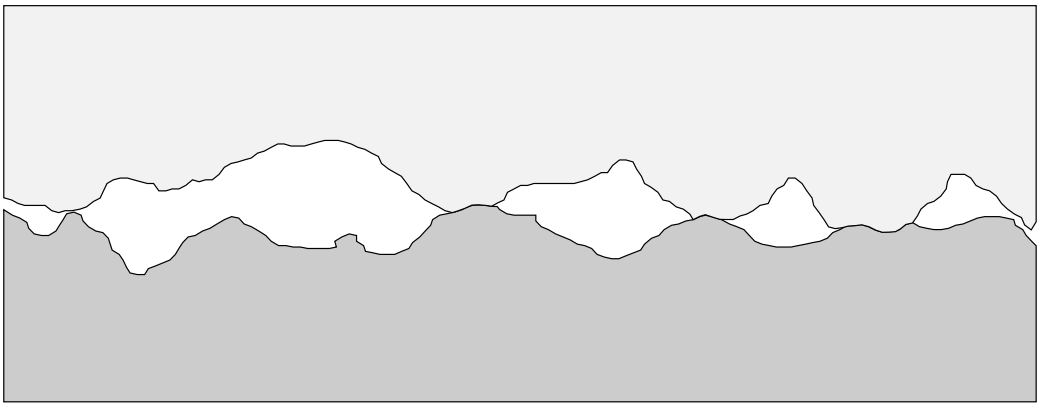

Figure 2.7: Two rough surfaces brought together are in intimate contact only at the asperity tips.

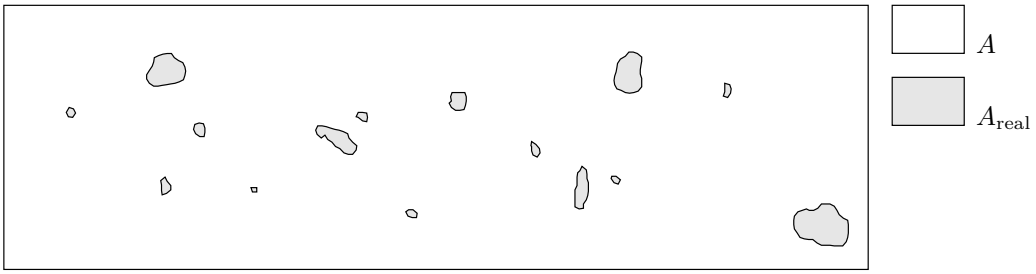

Figure 2.8: The real area of contact is much smaller than the apparent, geometric contact area.

contact, they touch only at the summits, which are called asperities. Figure 2.7 is a sketch of two rough surfaces in contact, viewed along the surface plane. Figure 2.8 is a similar sketch, in top view, illustrating the difference between the real and apparent contact area.

When the surfaces are first brought together, A_{real} is negligible. If a normal load is applied, the normal stress required to support it at the points of contact, called junctions, is enormous. Consequently, the touching asperities deform, and A_{real} grows as existing junctions grow in size and new junctions form. Assuming that the stress at the junctions gives fully plastic flow, the mean pressure σ_Y is determined by the hardness of the softer material: under fully plastic flow the real pressure $\sigma_{\text{real}} = W/A_{\text{real}}$ equals the mean pressure that the asperities can bear. It follows that

$$A_{\text{real}} = \frac{1}{\sigma_Y} W. \tag{2.8}$$

Archard [2] and Greenwood and Williamson [31] showed that proportionality between A_{real} and W can also be realised when the asperities deform elastically.

Friction is determined by the resistance to shear of the junctions: away from the junctions, the inter-material distance is much larger than the range of molecular forces. Processes that give shear resistance include cold welding and subsequent breaking of the welds, ploughing of the softer material by the harder asperities, and brittle failure of the asperities. The relative importance of the processes depends on the materials in contact: Bowden and Tabor [12] were studying metals and focused on cold welding, while Scholz [52] suggests that brittle failure is more relevant to rock friction.

Although not universally true, it is not unreasonable to assume that the frictional strength of each junction is proportional to its individual area, so that in sum the friction force is

$$f \propto A_{\text{real}}. \tag{2.9}$$

Combining this with equation (2.8) immediately gives $f \propto W$. Thus, the fundamental relationship in the Amontons–Coulomb laws is explained.

The asperity picture is consistent with the observed difference between the static and dynamic friction levels, and the time strengthening of μ_s. The picture is that during sliding, junctions continuously form and break, they rejuvenate. When sliding stops, the junctions are allowed to grow, and become stronger.

Baumberger and Caroli [4] point out that two classes of sliding interfaces should be distinguished, namely interfaces between

- *rough, hard* solids, which do not come into intimate molecular contact except at the asperity tips (as long as the apparent pressure $\sigma = W/A$ is well below elastic moduli, like E),
- *smooth* and/or *soft* solids which do get into intimate contact everywhere.

The above explanation naturally applies only to the former type of interface.

2.4 Outstanding questions

Despite the successes of the rate and state constitutive equations and the asperity picture of Bowden and Tabor [12], being such a wide field friction has an extensive list of outstanding questions. I will name but a few here, some of them taken from Urbakh et al. [57].

a) How can we control friction in practice? Sometimes low/zero friction is desirable, as in bearings, sometimes high friction is desirable, like between the tyres and the road when braking. We are far from ignorant, lubrication being an obvious example of friction control, but how can we improve? Can we control dry friction by clever micro-structuring of the contacting surfaces?

b) How to bridge the gap between the scales? Friction is important from micro-mechanical applications, e.g. computer disk heads, to earthquake prediction. At the atomic level it is due to electromagnetic interactions. Can we make a common framework for describing friction at multiple time and length scales?

c) Can the parameters in the phenomenological relationships be calculated from first principles or molecular dynamics simulations?

d) How are friction and wear related? Friction and wear at micro- and nanoscales is generally smaller than at macroscales (Bhushan [10]). Can a better understanding of the small scales lead to insights that allow significant improvements in macroscopic applications?

e) How are the static and kinetic friction forces determined by molecule–molecule and, on larger scales, asperity–asperity interactions?

f) What really happens when sliding initiates at a solid surface?

g) What hidden information is contained in chaotic as opposed to regular periodic motion of a frictional interface?

Of course, these very general questions will not be addressed directly in this thesis. The questions I seek to answer have a more limited scope and are given at the end of Chapter 3.

Chapter 3

Recent experiments

The friction laws presented in Chapter 2 consider a single degree of freedom, the relative sliding velocity of the slider and the track/base. They do not describe any of the processes occurring at the sliding interface. This is linked with the intrinsic difficulty of measuring any of these processes: the sliding interface by definition is surrounded by solid material. Inserting a sensor would introduce a defect or inhomogeneity that would likely disturb the motion. In what has been presented so far, therefore, the *onset of sliding*, which will be the major topic of this thesis, is resolved neither in space nor time: either the centre of mass of the slider is stationary with respect to the track, or it is moving with some speed.

During the last decade, however, advances in camera technology and the novel idea of using *transparent* blocks in the sliding experiments have made the sliding interface directly accessible. In this chapter I present the experiments and experimental measures that I will seek to explain in later chapters. They have been carried out by the group of Jay Fineberg at the Racah Institute of Physics in Jerusalem [7, 8, 45–48] and by Maegawa, Suzuki, and Nakano from Yokohama University and Toyota Motor Corporation [36]. Recent experiments that I will not try to model include the study of sphere on plane contacts in, e.g., [22, 51]; microstructured interfaces in, e.g., [9, 58]; and gel–glass interfaces in, e.g., [5].

For the experiments I seek to explain I will first give a brief introduction to how the measurements were conducted, and then include figures that show selected results. I will not give an exhaustive display of the experimental results that I will use in this work, preferring to defer their introduction until I am ready to compare my simulations to them.

3.1 Experimental setup

At the most basic level, the experiments consist of subjecting two blocks of the transparent, brittle material poly(methyl methacrylate) (PMMA), known commercially as Plexiglas, to normal and tangential loading forces and observing the dynamics of the interface between them. The system is schematically depicted in Figure 3.1. For clarity, I have excluded the loading and measurement devices from the figure. Typically, the lower block, called the *base* or *track* interchangeably, is glued to a support made of a much stiffer material, like aluminium. The upper block is called the *slider*, and a vertical force F_Z acts on the top surface of the slider. It can be uniformly or nonuniformly distributed. It extends over the whole top surface. The tangential loading force F_X can be localised or extended depending on the details of the coupling of the loading device to the sliding system.

The PMMA blocks were roughened with sandpaper, giving rough, hard solids for which the asperity picture of Section 2.3 is applicable. The two blocks therefore touch only at the asperities. Light passing from one block to the other one will usually pass from PMMA to air and then to PMMA; only at the junctions does the light pass directly from PMMA to PMMA. When illuminating the whole apparent contact with a laser sheet at an angle well above the critical angle for total internal reflection, the ratio of transmitted to incident light is a direct measure of the real to geometric contact area. Figure 3.2 illustrates this measurement technique.

The details of the measurements can be found in [45, 46]. The light was captured at rates of 30 or 100 kHz as 1280×16 or 1280×4 pixels in the $x \times y$-directions. Each pixel includes light from multiple junctions. The output variable is the transmitted intensity as a function of space and time, $I_{\text{trans}}(x, y, t)$, proportional to the real contact area $A_{\text{real}}(x, y, t)$.

In addition to $I_{\text{trans}}(x, y, t)$ and measures derived from it, macroscopic data was acquired by traditional means. The global loading forces F_X and F_Z were measured directly by applying them through S-beam load cells. As well as providing force data, the load cells have a known stiffness that, if low, becomes the stiffness of the loading apparatus. The local normal and shear stresses adjacent to the sliding interface were measured indirectly by use of strain gauge rosettes mounted 2 mm from the bottom of the slider, on the xz-face. Ideally, one would have access to the stresses *at* the sliding interface, but this has not been obtained in the current experiments: for stresses, the challenge of taking measurements in between the solid blocks has not been overcome.

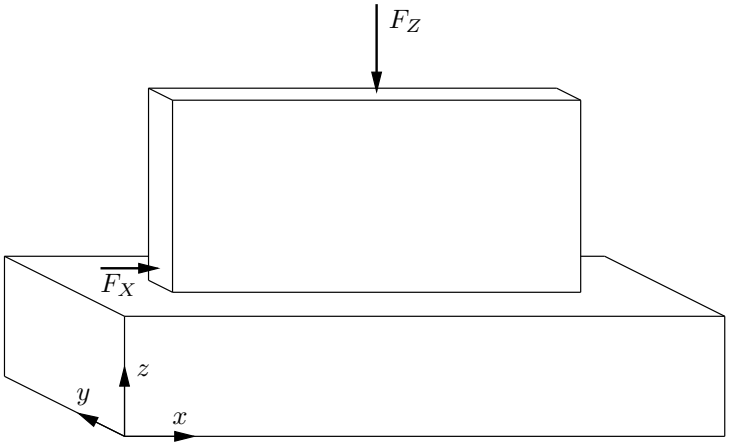

Figure 3.1: Sketch of the experimental setup I am modelling (not to scale). In equilibrium the normal force F_Z is balanced by the net normal force W on the slider from the track and F_X is balanced by friction (not shown).

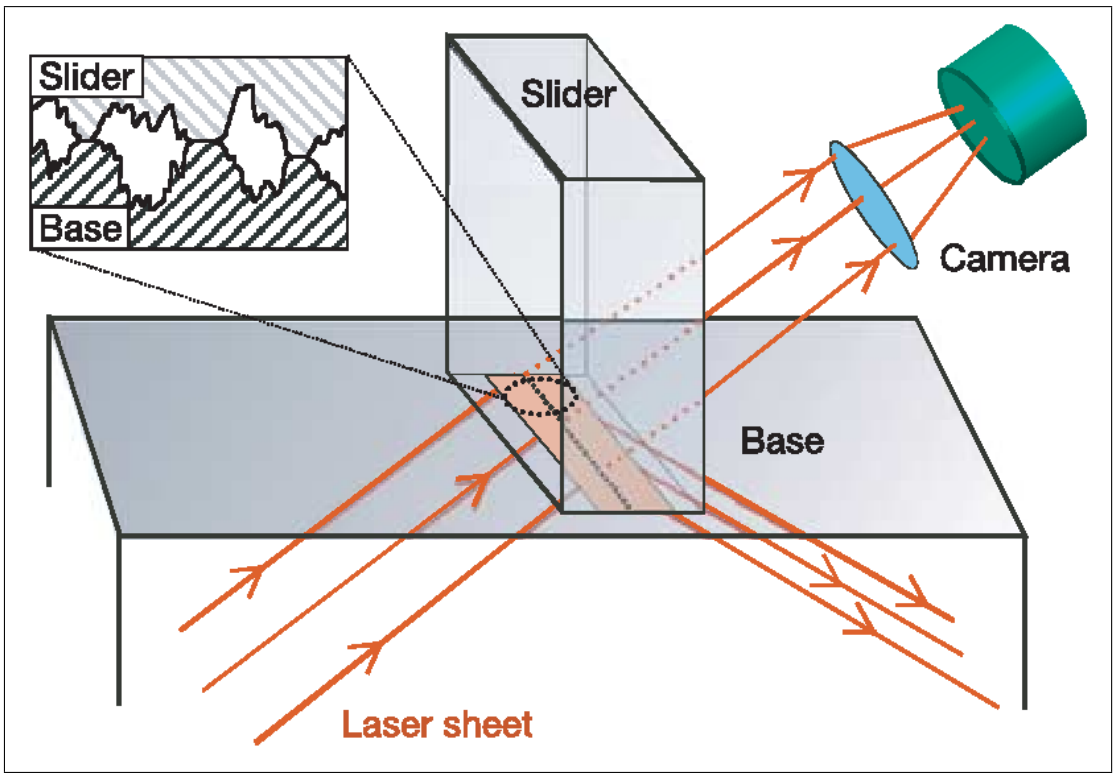

Figure 3.2: Measuring the local area of contact by utilising total internal reflection at PMMA–air interfaces. Taken from Rubinstein et al. [45].

3.2 Experimental results

3.2.1 Loading curve

The loading curve is the function $F_X(t)$; experimental loading curves are shown in Figure 3.3. In Figure 3.3a the normal load was $F_Z = 3.3$ kN, while in Figure 3.3b, $F_Z = 400$ N.

The global trend is a quasi-linear increase of F_X up to a maximum value where stick–slip starts. The driving velocity V is small compared to the internal dynamics, and sudden drops in F_X are associated with each movement of the slider; the stick periods are interspersed with fast slip/sliding events.

Macroscopic sliding occurred for the first time at ca 65 and 2.8 s, indicated by the dotted vertical line in Figure 3.3b. The many small drops in F_X *prior* to macroscopic sliding are associated with partial slip events, in which slip occurred at the trailing edge while the leading edge remained pinned. I return to this in Section 3.2.3.

3.2.2 Crack-like detachment fronts

From the local real area of contact $A_{\text{real}}(x, y, t)$ one can deduce whether a given part of the interface has been set in motion: if the slider moves, the junctions are renewed and the contact area changes. Figure 3.4 shows $A_{\text{real}}(x, y)$, normalised by the value at the start of the event, for six time instants bracketing the sliding onset. The figure shows that at $t = 0.7$ ms, measured from the start of the event, the contact area has been modified over the left half of the interface while remaining unchanged over the right half. This shows that the slider does not move as a rigid body; instead, sliding initiates at the trailing edge and propagates towards the leading edge as a rupture/crack front. The same observation was made by Baumberger et al. [5], who studied a gel–glass interface.

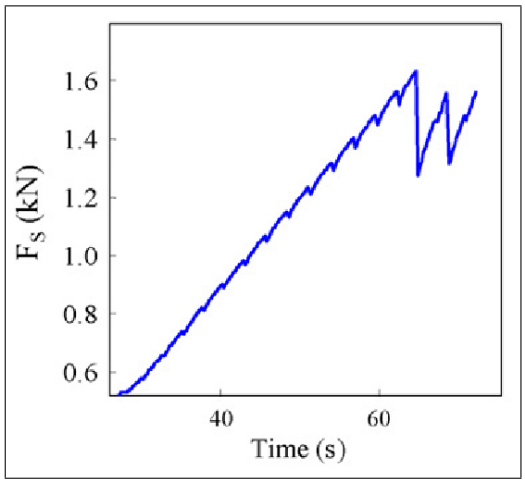

(a) F_S is the same as my F_X. Taken from Rubinstein et al. [48].

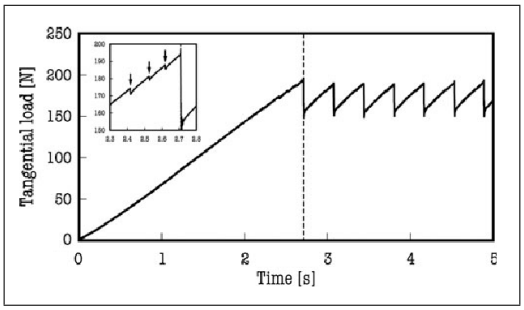

(b) The inset shows the loading curve in the interval 2.4–2.8 s, at forces 150–200 N. Taken from Maegawa et al. [36]. The time axis's ticks and label have been copied from the bottom part of the full figure.

Figure 3.3: Examples of loading curves from experiment. Different normal loads F_Z and loading rates V were applied in the two experiments.

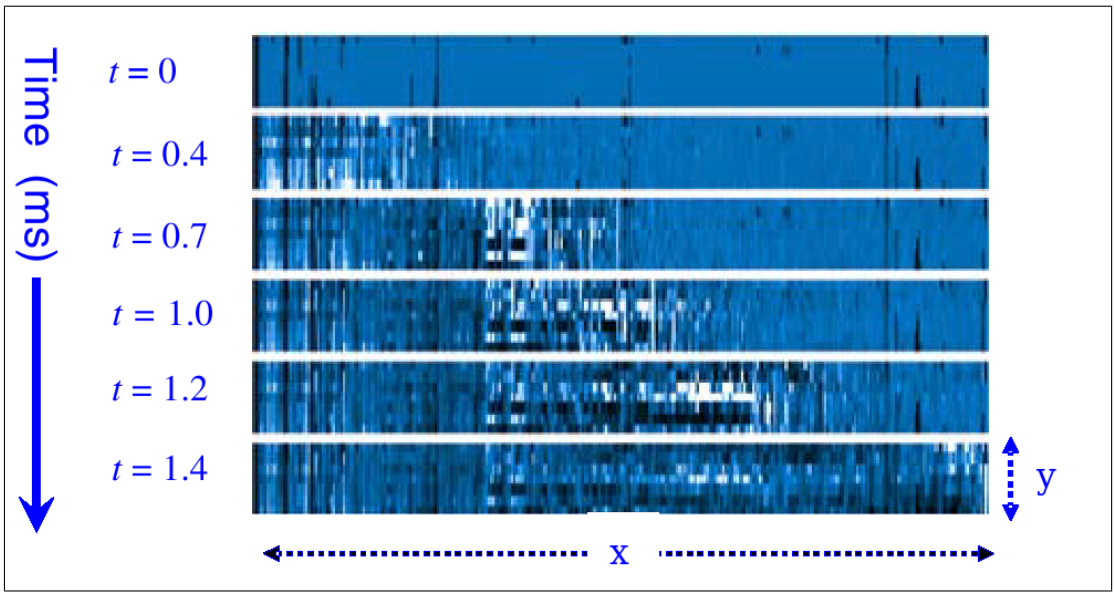

Figure 3.4: Photographs of the slider–track contact area normalised by the values at $t = 0$, with t measured from the start of the event. The spatial resolution is 1280×16 pixels, and the $x \times y$ scale of each photograph is 140×6 mm^2. Darker (lighter) shades correspond to a decrease (increase) in real contact area. Taken from Rubinstein et al. [48]. I have renamed the spatial directions to x and y.

Bennewitz et al. [9] studied the tangential strain in a regular array of pyramidal tips sheared against a glass surface and observed compression of the tip array, also indicative of the trailing edge moving before the leading edge.

A single figure containing the information of every photograph from an event can be made by averaging each image along the y-direction. This is justified because the sample is shorter in the y-direction than in the x- (front propagation) direction by design, so that the fronts can be considered one-dimensional along the interface. The resulting $A_{\text{real}}(x, t)$ is shown in Figure 3.5. This gives a clearer view of how the rupture traversed the interface. It started as a fast (sub-Rayleigh) front at the trailing edge. At about 0.06 m it split in two: one even faster (intersonic) front and a slower front. While the intersonic front hardly affected the real contact area, this was significantly changed by the passage of the slow front. At 0.12 m the slow front changed back to a fast front that eventually reached the leading edge. The interplay between these fronts, whose speeds differ by an order of magnitude, remains poorly understood.

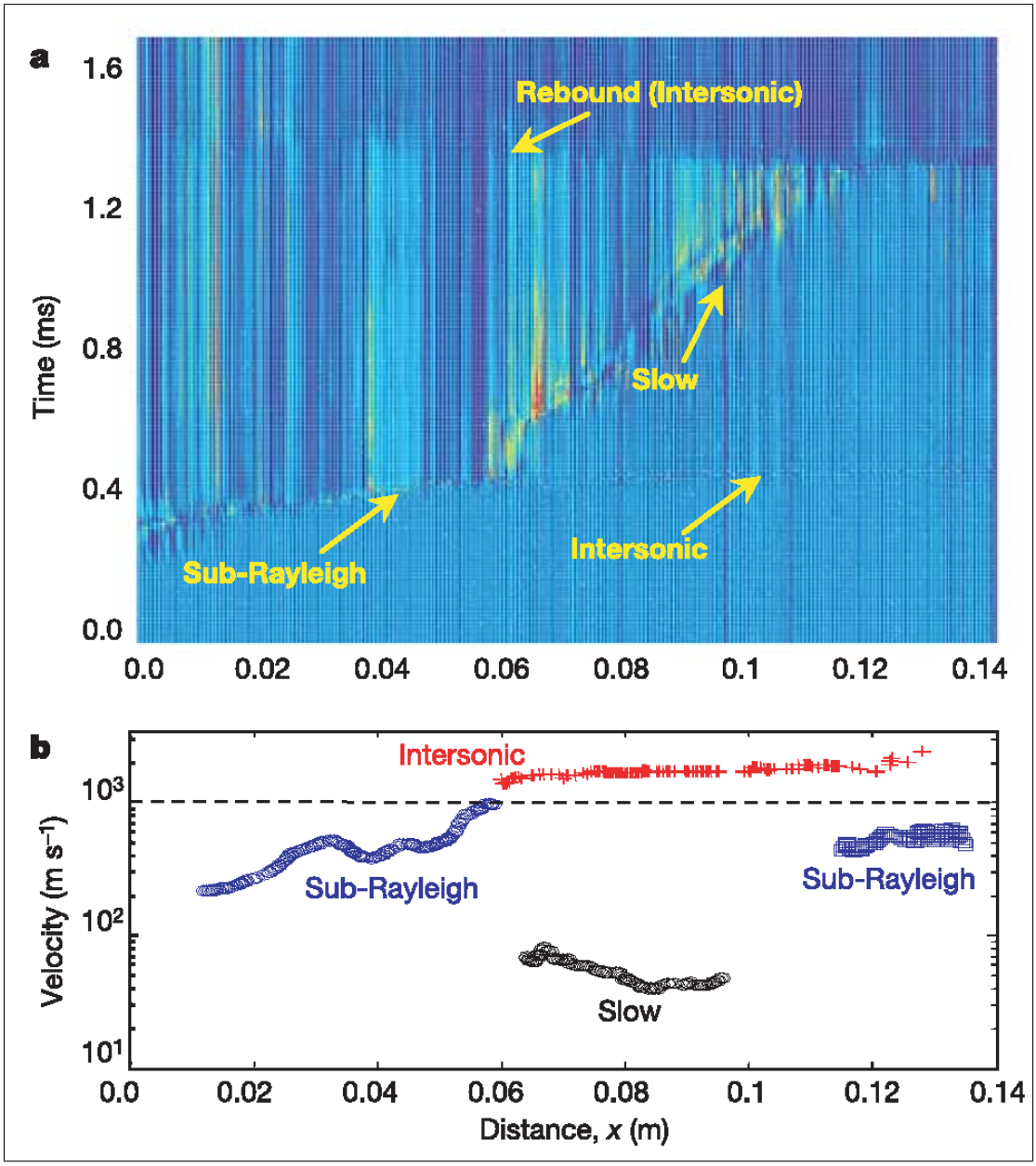

Figure 3.5: (a) combines photographs like those in Figure 3.4 into a single figure by averaging each image along the y-direction. Each horizontal line is $A_{\text{real}}(x, t = \text{constant})$. Successive lines (upwards) are separated by 10 μs. Colder (hotter) colours correspond to a decrease (increase) in contact area. Each rupture front is seen as an abrupt change in colour. The front velocity is the inverse of the slope: fronts with a small slope are fast, as they propagate far in a short time; fronts with a bigger slope are slow, as they take longer to propagate the same distance. (b) shows the velocities of the labelled fronts. They are grouped according to the range of velocities in which they lie. The rebound front is not shown in (b). Note that the velocities of the fronts differ by an order of magnitude, and that the slow front is six orders of magnitude faster than the driving velocity $V = 10$ μm/s. The dashed line is the Rayleigh wave speed V_R (Rayleigh waves are surface acoustic waves). Taken from Rubinstein et al. [45].

3.2.3 Precursors to global sliding

Every rupture front does not traverse the entire interface: they can arrest before reaching the leading edge. The slip event is then called a *precursor*. Its length L_p is simply the distance from the leftmost to the rightmost point that slipped. As long as all precursors nucleate at or near the trailing edge, L_p is just the x-value at the rightmost point.

Figure 3.6a is similar to Figure 3.5, but note the different scale of the temporal axes. Where Figure 3.5 brackets a single event, Figure 3.6a contains the whole experiment. By taking the temporal derivative $|\mathrm{d}A_{\mathrm{real}}(x,t)/\mathrm{d}t|$ one obtains Figure 3.6b, from which L_p is measured.

In the previous section we saw that the slider does not move as a rigid body, but that instead, sliding starts at a nucleation point (the trailing edge). The leading edge remained pinned for some time while the rupture front propagated. Now, Figure 3.6 shows that the slipping region can re-attach without reaching the leading edge at all. Successive precursors invade the interface in discrete steps, as seen by the increasing length over which $A_{\mathrm{real}}(x,t)$ changes in each event.

Since each precursor occurred at a well defined time t, the force that triggered it, $F_X(t)$, can be found. The set of points (F_X, L_p) for an experiment can be plotted, as in the inset of Figure 3.6. This is what I will call an L_p–F_X curve. The defining properties of an L_p–F_X curve are the number of precursors and the shape of the curve. The inset of Figure 3.6 has 16 points. The shape is a more or less linear trend with a low slope, followed by a transition to higher slope at half the sample length ($L = 20$ cm).

A localised slip event that arrests before reaching the leading edge leaves some strain "frozen" at the interface. The corresponding stress can affect the nucleation and propagation of the next rupture front. Since the first precursor to reach the leading edge is a global sliding event that triggers macroscopic sliding, understanding precursors could help understand the global static friction threshold.

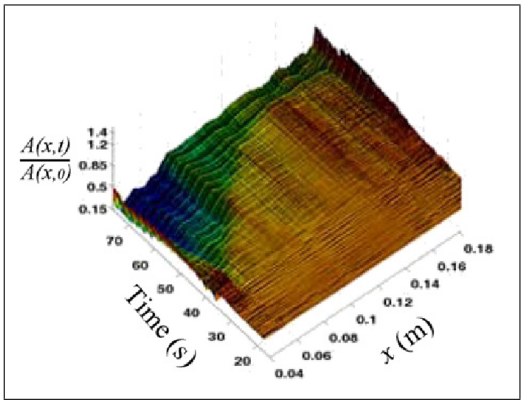

(a) The evolution of the real contact area. $A(x,0) = A_{\mathrm{real}}(x,0)$ is the spatially uniform value at the start of the experiment. Taken from Rubinstein et al. [48].

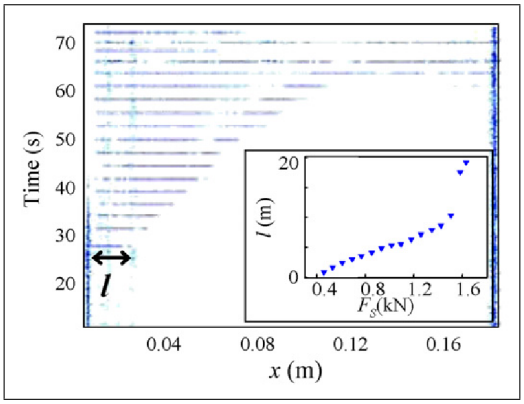

(b) The temporal derivative, $|\mathrm{d}A_{\mathrm{real}}(x,t)/\mathrm{d}t|$ of the data in (a). In the inset, l is my L_p and F_S is my F_X. The unit on the ordinate axis should be cm. The value of F_S is determined from the loading curve in Figure 3.3a; the value at event initiation (before the drop) is used. Taken from Rubinstein et al. [48].

Figure 3.6: Determining the length L_p of precursors.

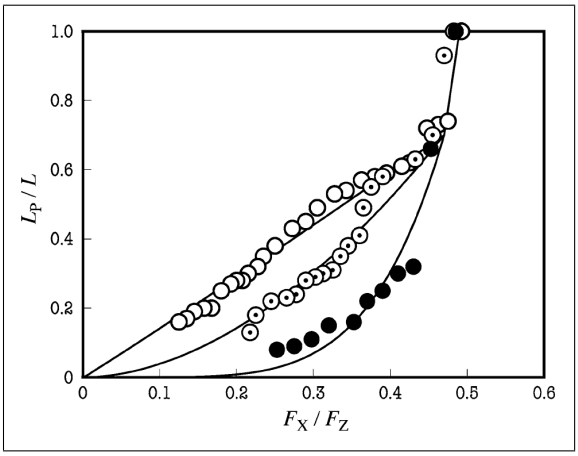

Figure 3.7: Experimental relationship between the length of precursors and the driving force, taken from Maegawa et al. [36]. Uniform normal loading (dotted circles) and two opposite non-uniform loading conditions (open circles and filled circles).

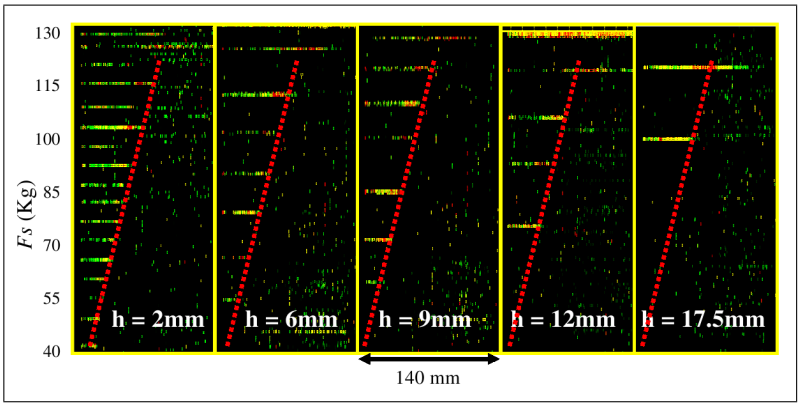

Figure 3.8: The number of precursors depends on the external loading conditions. The figure shows $|\mathrm{d}A_{\mathrm{real}}(x,t)/\mathrm{d}t|$, from which L_p is seen as the length of the light stripes. The five experiments differ only in the height h at which F_S (my F_X) was applied. Taken from Rubinstein et al. [48].

The L_p–F_X curve is not a property of the interface alone, but depends strongly on the external loading conditions. For instance, the distribution of the normal load F_Z affects both the number of precursors and the shape of the curve (Figure 3.7), while the height h above the interface at which F_X is applied affects the number of precursors only (Figure 3.8). I return to both points in later chapters. The prediction of L_p–F_X curves will be a major topic in this thesis.

3.2.4 Crack front velocities

Figure 3.5 showed a rupture front travelling at sub-Rayleigh speed splitting in two branches: an intersonic front and a slow front. The slow front later changed into another sub-Rayleigh front. What governs the speed of a rupture front? In pursuit of the answer to this question, Ben-David et al. [7] measured the shear and normal stress profiles close to the sliding interface and compared the local shear to normal stress ratio before rupture to the instantaneous front speed at the same locations.

As mentioned, the local normal stress $\sigma(x)$ and the local shear stress $\tau(x)$ can be measured adjacent to the interface with strain gauge rosettes. Figure 3.9 shows the change in these quantities with increasing external loads, before any global sliding occurs.

The crack front or rupture front is the boundary between the slipping and pinned

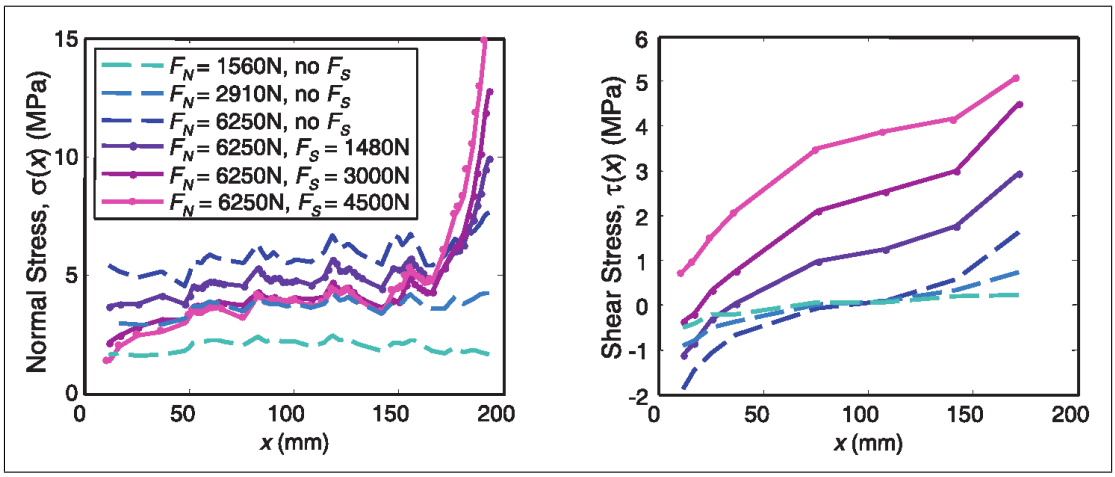

Figure 3.9: An example of the changes in $\sigma(x)$ and $\tau(x)$ with changing external load. F_N is my F_Z, F_S is my F_X, both were uniformly applied in this experiment. Measurement points are connected by lines for clarity. The antisymmetric $\tau(x)$ profile for $F_S = F_X = 0$ arises because of differential Poisson expansion frustrated at the interface (the slider and the track have different dimensions). Taken from Ben-David et al. [7].

parts of the interface. At the start of each event, this boundary moves from the nucleation point towards the edges of the sample at a velocity $v_{\text{crack}}(x)$ that is local (varies with x), particular to that event, and not well understood. Figure 3.10 shows v_{crack} at specific locations (x) as a function of the ratio of the shear to normal stress before the event, $\tau(x)/\sigma(x)$. A roughly linear trend can be discerned in the slow and sub-Rayleigh regimes, but there is a high degree of variation in the data. Also of considerable interest is the fact that τ/σ takes values as high as 2, meaning that the local stress ratio can exceed the global static friction coefficient of 0.5 by a factor of four.

3.3 Multi degree of freedom models

So far, I have shown in this chapter that modern experiments are probing the spatiotemporal details of sliding initiation. Obviously, models that can reproduce or give insight into these results must consider the spatial extension of the interface.

3.3.1 Earthquake models

Within the earthquake community there exists a large body of numerical works on the friction of extended systems. The idea motivating these studies is that a common type of earthquake, those occurring in the upper ten kilometres or so of the Earth's crust, is controlled by friction ([13, 21]). Slow deformations in the mantle drive tectonic motion, and because the tectonic plates cannot slide freely against each other, but are pinned by friction, stresses build up. When stress is suddenly and violently released, earthquakes occur.

Extended frictional systems are used as models of earthquake faults. This dates at least back to a 1967 work of Burridge and Knopoff [19], in which a 1D chain of blocks connected by springs was studied in the laboratory and in a computer model (Figure 3.11). In general form, the model consists of a chain of masses and equations prescribing

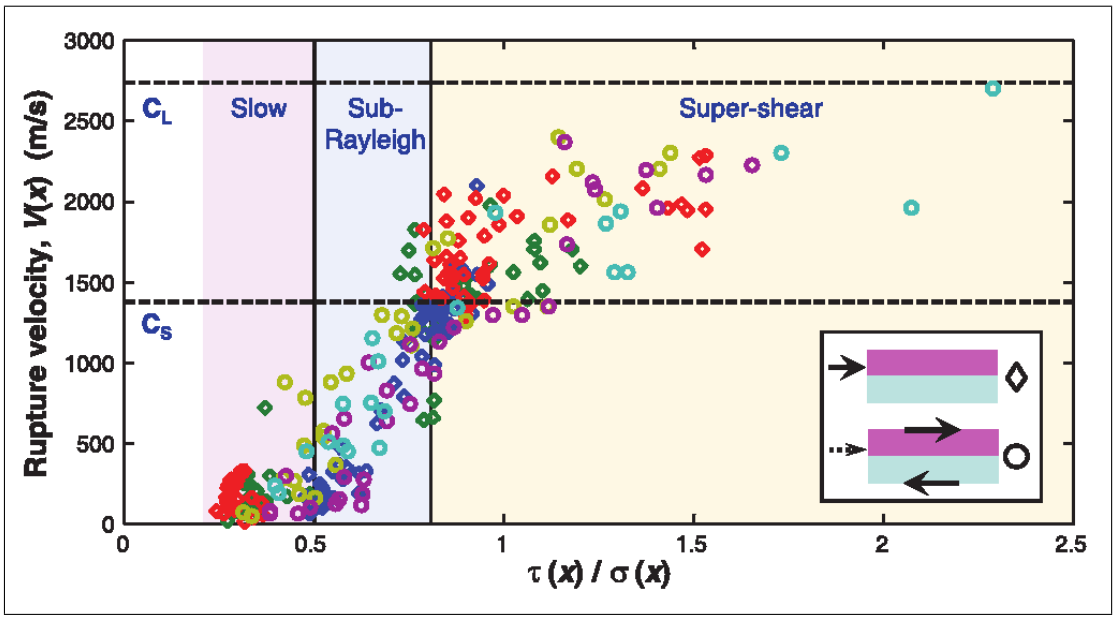

Figure 3.10: $V(x)$ is my $v_{\mathrm{crack}}(x)$, the crack front velocity, here presented for 287 different system-sized slip fronts. Shear was applied at the edge (diamonds) or predominantly uniformly (circles). Measurements were performed at strain gauge rosettes located away from the edges of the $L = 200$ mm sample at $x = 108$ mm (red), 142 mm (green), 172 mm (blue), 77 mm (magenta), 108 mm (yellow) and 142 mm (light blue). Dashed lines indicate longitudinal (C_L) and shear (C_S) wave speeds. Taken from Ben-David et al. [7].

- the interaction between the masses,
- the friction law for each mass,
- other external forces on the masses.

Spring–block models are obtained when the only interactions between the masses are springs connecting neighbouring blocks. In the Burridge–Knopoff model, all the inter-block springs are equal. The external load is applied through coupling by another set of equal springs to a rigid driving block. The model is fully time dynamical. Many variants, using different friction laws for the constituent blocks, have been studied. Commonly asked questions are:

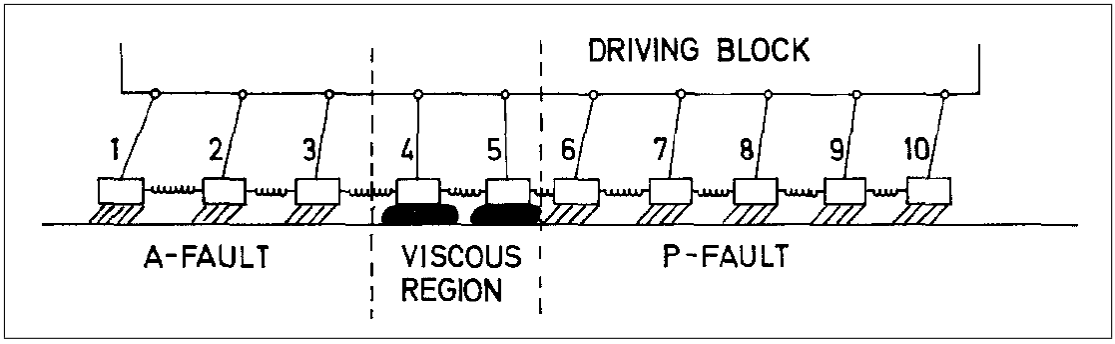

Figure 3.11: Original sketch of the spring-block model of an earthquake fault by Burridge and Knopoff [19].

- what is the distribution of event amplitudes (length, duration, energy released)?
- given the event history, can you predict the occurrence of the next big event?
- what types of friction law give instability?

In 1994 Carlson et al. [21] reviewed the ongoing studies of the Burridge–Knopoff-like models.

Another approach is to study cellular automata, or "sand pile" models, where there is no real time dynamics, and much larger system sizes can be handled. Again, the interest has primarily been in event sizes and distributions, and in the concept of self-organised criticality, introduced by Bak et al. [3] and followed up by Olami et al. [40] and many others. Neither the time dynamical nor the quasi-static approaches have been concerned with the modelling of the onset of friction; geological systems are presumably not in the transient phase of stress build-up, but well into the stick–slip regime.

3.3.2 Models of boundary lubrication (Persson)

Persson [41, 42, 43] has developed a theoretical/numerical framework for studying slider–track friction in boundary lubrication, where the lubrication layer has molecular dimensions. In this model the lubrication layer can be in a fluid or a solid state, with the whole layer taking on a granular structure with pinned, solid "islands" surrounded by fluid. The numerical model he derives is equivalent to the Burridge–Knopoff model, but the physical interpretation of the blocks is different, being in this model the pinned islands.

In Persson's model the masses of the blocks are determined by the extent of what he calls *stress domains*; the sum of the masses is not equal to the mass of the slider. I return to this subtle point in Section 4.6.

Braun and Peyrard [14, 15, 16] developed and applied a master equation framework applicable to friction governed by the breaking and formation of local contacts, i.e. the earthquake models and Persson's model.

3.3.3 Models in fracture mechanics

The cracking, or rupture, of the interface binding two solids together has been studied as a problem in fracture mechanics. A good list of references is provided by Shi et al. [53]. Common topics of interest are:

- under what conditions can the rupture propagate?
- how does the rupture propagate (crack-like, pulse-like)?
- what is the speed of rupture propagation?
- what is the energy partition between radiation (seismic waves) and dissipation?

As seen in Figure 3.5 the rupture speed can change as the front propagates; Dunham [25] summarises the work on the transition from sub-Rayleigh to supershear speeds.

As with earthquake models, the main body of work has not been concerned with the friction and sliding initiation of laboratory samples. It is not uncommon to disregard the nucleation process altogether in favour of studying only the propagation of the crack. The crack nucleation point is then imposed directly, which in finite element calculation

simplifies the choice of mesh (see e.g. [53]). In theoretical studies, e.g. [34, 39], only the speed of sustained ruptures was considered.

Gerde and Marder [29] studied self-healing cracks at the interface between an elastic slider and a rigid track, and proposed that they give an alternative to the asperity picture in explaining the proportionality between the sliding threshold and the normal load. They did not consider sliding onset.

3.3.4 Models of sliding onset

In an attempt to build a numerical model accounting for the experimental observation that global sliding is preceded by precursors as well as the interplay between the slow, sub-Rayleigh and supershear fronts, Braun et al. [18] in 2009 introduced a Burridge–Knopoff-like model and focused their analysis on the onset of sliding. The model is similar to that of Burridge and Knopoff in that it consists of a linear chain of inertial blocks connected by springs. It differs from the original in that

- external shear is applied on a single block, located at the edge of the sample
- in place of a simple friction law, each block is connected to the track by an ensemble of springs, each with given stiffness, breaking strength and waiting time for reattachment.

The use of an ensemble of springs in place of the more commonly used empirical friction laws is based on work by Braun and Röder [17] and Filippov et al. [27].

Braun et al. [18] were able to observe precursors to sliding as well as interacting fronts propagating at different velocities. However, in their published results the number and length of precursors was very different from the experiments, the loading curve was significantly different because of the long duration of the events and the speed of the observed fronts was not studied quantitatively. Unpublished work by Malthe-Sørenssen and his students indicate that overcoming these discrepancies is not merely a matter of changing the values of parameters in the model.

In 2010, Maegawa et al. [36] studied the onset of sliding, focusing on the influence of normal loading on the length and number of precursors. The experimental part of their paper was mentioned above. They also included a numerical model similar to the Burridge–Knopoff model, but again, the external shear was applied at a single block. The model predicted the correct ordering of the L_p–F_X curves for different loading conditions, but failed to predict the correct shape of the curves and the number of precursors. The model also has additional fundamental shortcomings related to the number of blocks included and the continuity of the shear and normal stress profiles that will be discussed in Chapter 4, where I study their model and extend it.

Scheibert and Dysthe [50] studied L_p–F_X curves in a 1D model of a long and thin elastic block under uniform shear load by assuming simple laws for the evolution of the shear and normal stresses along the interface.

Very recently (March 2011), Bouchbinder et al. [11] studied a model where they include the real contact area, and observed analogies to the slow rupture fronts.

I do not know of any work studying sliding onset with a 2D model.

3.4 Outstanding questions

As a summary of Sections 3.2 and 3.3, the following is an incomplete set of outstanding questions regarding the onset of frictional sliding.

a) How can you predict the correct shape and number of precursors in the L_p–F_X curve of a given experiment? On what does it depend?

b) What is the coupling between the statics (L_p–F_X, stress profiles) and the dynamics (rupture fronts)?

c) What determines the speed of a rupture front? What is the mechanism that makes a fast front slow down, or a slow front speed up? Is it the same mechanism, or two different processes?

d) What is the physics governing the slow fronts? Under what conditions can you observe them in a numerical simulation?

e) Where will a rupture front stop?

f) How can the local shear to normal stress ratio τ/σ exceed the static friction threshold by a factor of four?

g) What information do you need in order to predict the triggering time and amplitude of the next event? In terms of earthquake models: to predict the next earthquake? And given this information, can you perturb the system to make the event smaller, i.e. can you relieve stress and turn the big earthquakes into many small ones?

Answers to (a) and (b) are found in this thesis. Progress is made on (c) and (f), while (d), (e) and (g) remain open questions.

Part II

NUMERICAL MODELS

Chapter 4

1D model

Analytical models for the global frictional behaviour of a sliding system were discussed in Chapter 2, along with their microscopic origins. The models incorporated a single degree of freedom: the velocity of the centre of mass of the slider. In Chapter 3, recent experiments with a high spatial and temporal resolution were shown to give results that could not be described by such macroscopic friction laws. The lack of theoretical and numerical understanding of these results was pointed out in Section 3.3.

I started working on this thesis by implementing the model of Maegawa et al. [36]. In this chapter I begin by motivating the approximations that take the full 3D experimental setup to a simple 1D model. I then describe the model in detail and extend it from what Maegawa et al. used. Section 4.2 presents some of the technicalities of implementing the model in a computer program. Results are given and discussed in Sections 4.3 to 4.5. In Section 4.6 I discuss a strong resolution dependence of the side driven 1D model. Then, I introduce a top driven version of the model in Section 4.7 and study it in Sections 4.8 to 4.10. Finally, Section 4.12 gives a brief summary of the 1D model. A full summary can be found in Section 7.1.1.

The 1D model serves as an important tool to build intuition. Its simplicity, a weakness when it comes to quantitative comparison with experiments, is at the same time a strength in that it makes the model easier to analyse. For instance, the analytical calculations in Section 4.4.1 develop ideas that are used to understand the two-dimensional model of Chapter 5, and the 1D model is an important reference more indirectly as well: when a measure agrees well with experiment in the two-dimensional model, but not in 1D, this indicates that the second dimension is important in explaining the experimental result in question.

4.1 A 1D spring-block model with side driving

4.1.1 Deduction of the model

The full experimental setup consists of two three-dimensional blocks of PMMA, the apparatus in which they are mounted, load cells and motors that apply the external loads, and the camera and other sensors. The PMMA blocks are rough, so their interface is made up of myriad junctions. Assumptions and simplifications serve the purpose of extracting from this complicated setup a numerically tractable model system. The ultimate simplification is to consider only the centre of mass of the slider and let the forces act in this point, i.e. to return to the models of Chapter 2; the 1D model *can*

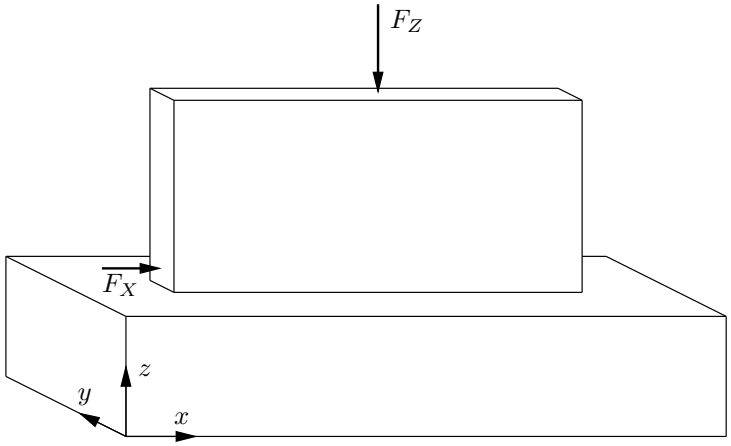

Figure 4.1: Sketch of the experimental setup (not to scale). F_X is applied through a spring. F_Z acts along the entire upper surface of the slider, not necessarily uniformly. The same as Figure 3.1.

be introduced as an extension of this point-like model. Here, I will start with the experimental setup and simplify it bit by bit.

The first details to be ignored are the sensors and the frame holding the setup together. The frame is presumably much stiffer than the blocks, so that it deforms negligibly during the experiment. Next, the load cells are assumed to have well defined compliances, i.e. treated as springs in their Hookean regime. The remaining model system resembles Figure 4.1. The slider has length L, breadth B and height H in the x-, y- and z-directions. There are no external forces acting in the y-direction, and $L > H \gg B$, so the next simplification is to ignore the breadth. This has profound implications on the modelling of the interface between the two blocks: in only two dimensions, you cannot hope to accurately represent the junctions. For instance, the ratio of the size of asperities to the extent of the interface changes dramatically. This is fine, because I was not planning to keep the asperities in the model.

We are down to a two-dimensional system that is often denoted as 1+1D because it consists of one dimension in the plane of the interface plus the dimension out of this plane. (If the vertical dimension had been ignored instead, the notation would be 2+0D.) The main interest is in studying the deformation occurring along the interface between the slider and track. Ignoring the asperities, this interface is completely flat. The slider is not displaced in the vertical direction, but this dimension is still important as a pathway for elastic interactions between distant parts of the interface. I will ignore the vertical direction for simplicity; in Chapter 5 I return it to the model system. As there is no physical argument to mandate dropping it, I am not surprised that it turns out to be very important.

Only the x-direction remains, and so there can be no distinction between the slider and the track: there is only the interface left. We know that friction acts along this interface, and that it can deform. When deformed, there will be restoring forces acting to maintain the natural length. Because friction is proportional to the normal force, the forces in the vertical direction cannot be ignored completely, but must enter in the frictional strength.

A 1D spring–block model fulfils the remaining requirements of deformation, restoring forces and a local frictional strength. So does a continuum description discretised by the finite element method (FEM). I have chosen a spring–block model for ease of implementation and extension of the model, and for ease of comparison with the existing numerical studies of sliding onset by Braun et al. [18] and Maegawa et al. [36]. Because the external shear force is applied at the slider, I have used the stiffness of the slider to

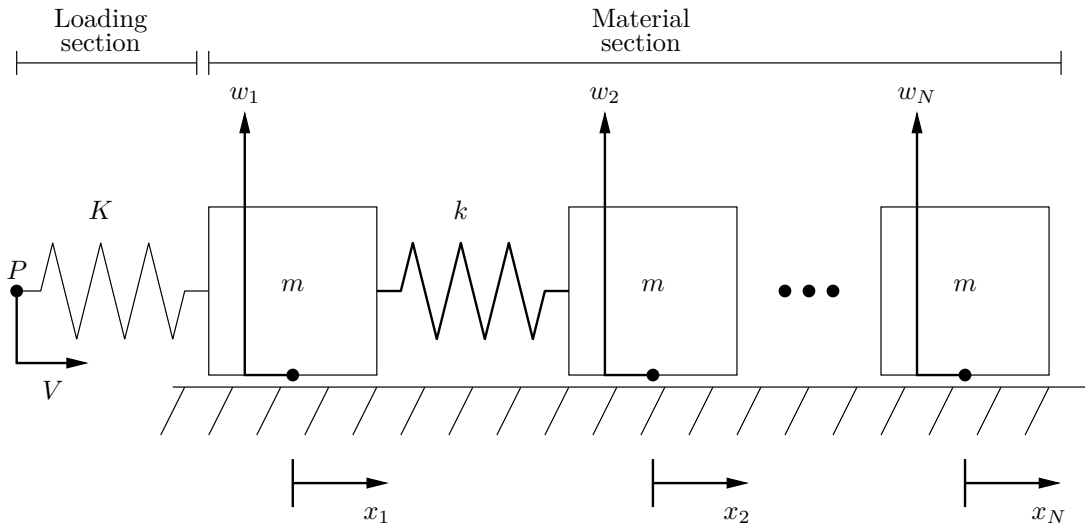

Figure 4.2: Model of the sliding system. The point P moves to the right with speed V. Adapted from [36].

determine the restoring forces. In the following section I give a complete description of the numerical model.

4.1.2 Equations and parameters of the model

Consider a line of N blocks of total mass M, connected in series with springs of equal stiffness k. A suitable coordinate transformation will remove the equilibrium length of the springs from the problem. Each block couples to the track through the Amontons–Coulomb laws with $\mu_s > \mu_k$. A driving force F_X is applied to the leftmost block through coupling via a spring of stiffness K to a point P moving with small and fixed velocity V to the right. The point and the spring of stiffness K are the loading section of the model, while the blocks and the interconnecting springs are the material section, see Figure 4.2.

The mass of each block is $m = M/N$. For a material of Young's modulus E, a specimen of length L, height H, breadth B and cross-sectional area $A = BH$ has a spring constant of

$$k' = \frac{EA}{L}. \tag{4.1}$$

In order for the model to reproduce this value regardless of N, the $(N-1)$ springs coupling the blocks, which are connected in series, must each have stiffness

$$k = (N-1)k' = (N-1)\frac{EA}{L}. \tag{4.2}$$

A discussion of this stiffness can be found in Section 4.6.

The equations of motion for the ith block are given by Newton's second law as

$$\begin{cases} m\ddot{x}_1 &= k(x_2 - x_1) &+ F_X &+ f_1 &+ F_{\eta,1}, \\ m\ddot{x}_i &= k(x_{i-1} - 2x_i + x_{i+1}) & &+ f_i &+ F_{\eta,i}, \quad \text{for } 2 \le i \le N-1, \\ m\ddot{x}_N &= k(x_{N-1} - x_N) & &+ f_N &+ F_{\eta,N}, \end{cases} \tag{4.3}$$

where x_i denotes the position of the ith block relative to its initial position, F_X is the force from the driving spring,

$$F_X = K(X - x_1) = K(Vt - x_1), \tag{4.4}$$

and the friction on the ith block is

$$f_i = \begin{cases} f_s^{(i)} & \text{when } \dot{x}_i = 0, \\ -f_k^{(i)} & \text{when } \dot{x}_i > 0, \\ f_k^{(i)} & \text{when } \dot{x}_i < 0. \end{cases} \tag{4.5}$$

As long as the static friction threshold is not exceeded, the static friction exactly balances the sum of the other forces and with w_i as the normal load on block i

$$-\mu_s w_i = -f_{\mathrm{s,max}}^{(i)} \le f_{\mathrm{s}}^{(i)} \le f_{\mathrm{s,max}}^{(i)} = \mu_s w_i. \tag{4.6}$$

The kinetic friction is

$$f_k^{(i)} = \mu_k w_i. \tag{4.7}$$

The normal load is distributed linearly across the blocks by setting

$$w_i = \frac{F_Z}{N}\left(1 + \frac{2i - N - 1}{N - 1}\theta\right), \tag{4.8}$$

where $\theta \in (-1, 1)$ is a parameter determining the non-uniformity. $\theta = 0$ gives uniform loading. Finally, a damping force $\eta(v_{i+1} - v_i)$, where η is an adjustable parameter and $v_i = \dot{x}_i$, acts on block i from block $i + 1$, so that the damping force on block i is

$$F_{\eta,i} = \eta(v_{i-1} - 2v_i + v_{i+1}). \tag{4.9}$$

The equations of motion (4.3) are solved forwards in time by the fourth order Runge–Kutta (RK4) method on a uniform temporal grid of resolution Δt. The RK4 method is described in Appendix A. Appendix C.2 discusses how the runtime of the code can be reduced with no changes to the output.

Table 4.1 lists the most frequently used parameter values for the 1D model. When presenting results, I will usually state only the values of parameters that differ from Table 4.1.

4.2 Numerical preparations

4.2.1 Time step length

The numerical solution of a differential equation differs from the analytical solution because of truncation error and round-off error. The time step length Δt must be chosen small enough to ensure stability and the desired accuracy.

The motion of a block from it slips to it re-sticks will have much in common with that of a harmonic oscillator. It starts at rest from a position where the spring on its left is compressed and stores elastic energy. It accelerates until the net force on it is zero, then starts decelerating as the net force becomes negative. If the neighbouring blocks are moving too, the motion becomes more complicated, but nevertheless, it's going to be oscillatory, albeit not necessarily a complete period. *The time step length should be small enough that the motion of each block is well resolved*, i.e. sampled by many time steps. A time scale for this is the period $T = 2\pi\sqrt{\frac{m}{k}}$ of a simple harmonic oscillator with mass m and stiffness k. With $\Delta t \ll T$, stability is obtained.

Macroscopic	Slider	L	100 mm
		H	20 mm
		B	5 mm
		A	100 mm^2
		E	2.5 GPa
		M	0.012 kg
	Loading	F_Z	400 N
		K	0.8 MN/m
		V	0.1 mm/s
		θ	
Microscopic		μ_s	0.7
		μ_k	0.45
Numerical		N	
		m	M/N
		k	$(N-1)EA/L$
		Δt	10^{-7} s
		η	$\sqrt{0.1}\sqrt{km}$

Table 4.1: Typical parameters used in the 1D model. An empty field means that the variable in question does not have a single, most common value. Macroscopic and microscopic parameters are taken from Maegawa et al. [36].

4.2.2 Initial conditions

The time evolution of the system is not given by the governing equations (4.3) alone. The initial conditions, i.e. the state of the system at $t = 0$ must also be given. Experimentally, the system is at rest before loading starts, and unless one has knowledge of the initial shear force profile, letting every spring have its equilibrium length is the natural choice. This gives the simple initial conditions

$$x_i(0) = v_i(0) = 0 \qquad \forall i, \tag{4.10}$$

which I will use unless otherwise stated.

A more general initial condition is to have a controlled shear force profile. I will use the notation

$$\tau_i = F_i^{\text{tot}} - f_i \tag{4.11}$$

to denote the external shear force on a node, where F_i^{tot} is the net force on the node including friction. The initial conditions can then be $\tau_i(0) = F_{\text{desired},i}, v_i(0) = 0\,\forall i$.

The simplest shear profiles to set up are those for which $F_X = \sum_i F_{\text{desired},i} = 0$. Assuming the system is initially stably at rest (no acceleration), $F_X = 0$ implies $\sum_i f_i = 0$. Since the shear and friction force on each node are equal in magnitude and opposite in sign, this implies $\sum_i \tau_i = 0$, which is consistent with Newton's third law, as all the shear forces are internal forces. To assign a given shear force profile, start at either end and pick an arbitrary position for the end node. Then place its neighbour so that the force on the end node has the desired value. For instance, if $x_1 = 0$ is chosen,

$$x_2 = \frac{F_{\text{desired},1}}{k}, \tag{4.12a}$$

$$x_3 = \frac{F_{\text{desired},2}}{k} - x_1 + 2x_2. \tag{4.12b}$$

Successively selecting the positions in this way one can assign any initial force to all nodes save the last one, which has no unplaced neighbour that can be used to adjust the force. Luckily, $\sum_i \tau_i = 0$ guarantees that the force on the Nth node equals $F_{\text{desired},N}$.

To have $\sum_i F_{\text{desired},i} = C \neq 0$ implies $\sum_i f_i = -C$ and $F_X = C$. The same scheme as outlined above can be used, provided that

$$x_2 = \frac{F_{\text{desired},1} - F_X}{k}. \tag{4.13}$$

4.2.3 Verifying the implementation

When writing computer programs, it is common for errors to appear inadvertently. A standard way to try to root them out is to compare the output from the program with analytical solutions, where available. In this section, I verify that my code correctly reproduces the initial motion of the leftmost block.

Solving for the motion of the leftmost block is fairly straightforward as long as the second block in the line remains at rest. The calculation follows the steps of Appendix B.1, in which the motion of a single block under Amontons–Coulomb friction are found to be regular stick–slip.

For $\eta = 0$ the equations of motion for the first block are, from sliding initiation at $t_0 = \frac{\mu_s w_1}{KV}$ and as long as $x_2 = 0$,

$$m\ddot{x}_1 = K(Vt - x_1) - kx_1 - \mu_k w_1. \tag{4.14}$$

The general solution is

$$x_1(t) = C\sin(\tilde{\omega}t + \phi) + \frac{KVt}{K+k} - \frac{\mu_k w_1}{K+k}, \tag{4.15}$$

where $\tilde{\omega} = \sqrt{\frac{K+k}{m}}$ and C and ϕ are determined by the initial conditions

$$0 = x_1(t_0) = C\sin(\tilde{\omega}t_0 + \phi) + \frac{(\mu_s - \mu_k)w_1}{K+k}, \tag{4.16a}$$

$$0 = \dot{x}_1(t_0) = \tilde{\omega}C\cos(\tilde{\omega}t_0 + \phi) + \frac{KV}{K+k}. \tag{4.16b}$$

Moving all terms with C to the left, then squaring and summing the initial conditions gives

$$C^2 = \left[\frac{(\mu_s - \mu_k)w_1}{K+k}\right]^2 + \left[\frac{KV}{\tilde{\omega}(K+k)}\right]^2 \tag{4.17}$$

$$C = \pm\left(\left[\frac{(\mu_s - \mu_k)w_1}{K+k}\right]^2 + \left[\frac{KV}{\tilde{\omega}(K+k)}\right]^2\right)^{1/2}. \tag{4.18}$$

The value of ϕ follows from equation (4.16a) and is

$$\phi = -\tilde{\omega}t_0 - \arcsin\left(\frac{(\mu_s - \mu_k)w_1}{C(K+k)}\right). \tag{4.19}$$

Figure 4.3 shows that the numerical solution agrees well with the analytical solution, verifying the implementation. The agreement is better for smaller steps in time. The

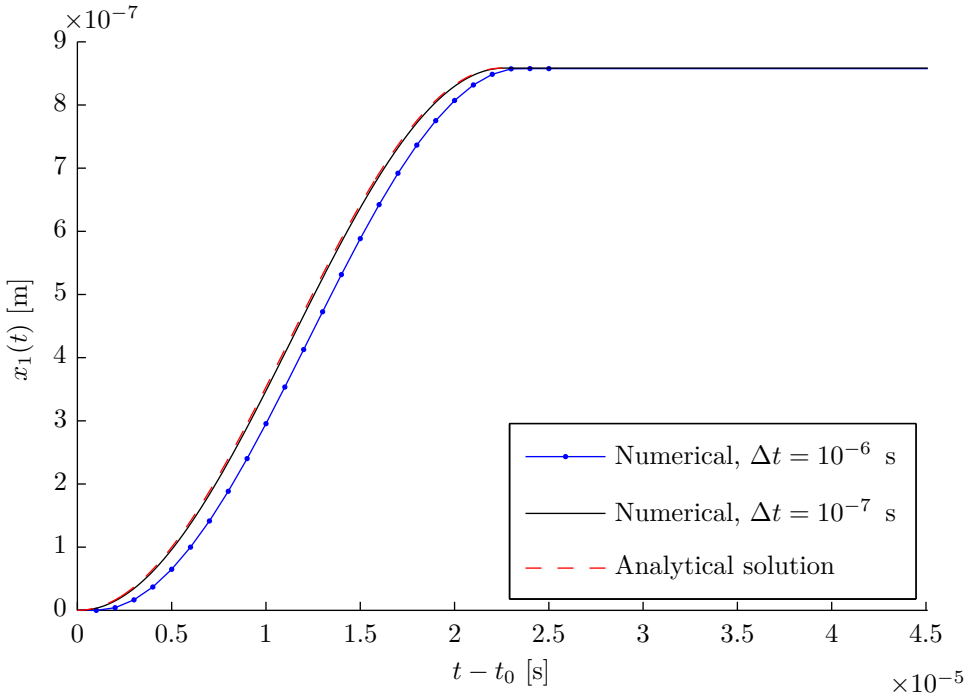

Figure 4.3: Verifying that the numerical solution approaches the analytical solution when $\Delta t \to 0$. The graphs show the initial motion of the leftmost block in the side driven 1D model when $N = 10$ and $\eta = 0$. A coarse time scale is $2\pi\sqrt{m/k} = 5 \cdot 10^{-5}$ s.

time resolution required depends on the accuracy demanded, but as mentioned in Section 4.2.1 it is necessary to ensure that each block motion (from start to stop) is resolved in time. The time scale for the oscillatory motion of the blocks is roughly $2\pi\sqrt{m/k}$, and for a time step of this order or larger, the numerical integration is unstable and unbounded fluctuations occur in the solution. I hold that for $N = 10$, Figure 4.3 shows that $\Delta t = 10^{-6}$ s is a sufficient time resolution. Going to $\Delta t = 10^{-7}$ s will improve the agreement with the analytical solution, but due to the simplicity of the model, I don't expect the additional accuracy to add any value to the *physics*.

In Section 4.3.1, output from the model will be compared to the published results of Maegawa et al. [36], providing another check of the implementation.

4.3 First results

4.3.1 Loading curve and number of sliding blocks

The first results that I present are the loading curve $F_X(t)$ and the number of blocks that are sliding at any given time, N_{sliding}. Experimental loading curves were presented in Section 3.2.1, Figure 3.3. The side driven 1D model with $N = 10$ produces Figure 4.4, which has the same features: a quasi-linear global trend followed by a stick–slip regime, and smaller relaxations preceding the onset of global sliding.

The slip events always nucleate at the trailing edge of the system. This is clear from the way the system is driven: force is transferred from the loading section to the first block from the left only, and this block has to move before any force is transferred to the second block, etc. Combining the top and bottom parts of the figure, therefore, shows

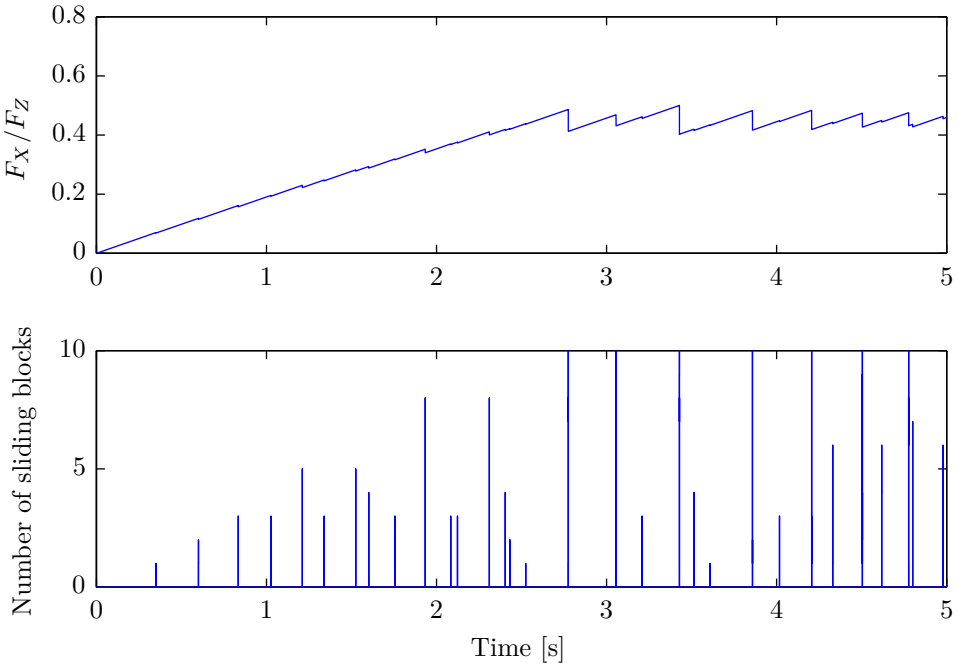

Figure 4.4: The force from the driving stage (top) and the number of blocks that are sliding at any point in time (bottom). Global sliding is preceded by a number of precursors, i.e. local slip events where some blocks are moving while the others remain at rest. $N = 10$, $\theta = 0$, $\Delta t = 10^{-8}$ s, $\eta = 0$, remaining parameters as in Table 4.1. The result is in agreement with Fig. 10 of Maegawa et al. [36], which I show in Figure 4.6.

that the length of the precursors tends to increase with increasing F_X/F_Z until global sliding occurs. The measure L_p versus F_X will be studied in Section 4.4.

Figure 4.4 shows a separation of time scales: the force from the loading section drops so quickly at each event that the event duration is not resolved in time. Figure 4.5 is a closer look at the first global sliding event and shows that the dynamics of each event is richer than one would perhaps expect from looking at the complete time series only. From the two figures one finds that the time between events is of the order 0.1 s, while the event duration is of the order 1 ms, a hundred times shorter and in agreement with Figure 3.4. This is what is meant by a slowly driven system; when the event duration is much shorter than the loading period between events, the change in the loading force due to the motion of the point P during each event is negligible.

Figure 4.4 should be compared to Figure 4.6, which is the simulation result published by Maegawa et al. [36]. As I use the same parameters one would naively expect that the figures should be exactly equal. Indeed, the shape of the loading curve is nearly the same, and so is the pattern in the number of sliding blocks (increasing number of blocks in later events, with some smaller events in between). An exact match is not obtained, however. Because there is no randomness in the model, minor differences in roundoff error and the fine details of the implementation of the starting and stopping of each block become important. The details of my implementation can be found in Appendix C.1. There is also a minor difference in the value of k (compare equation (4.2) to their equation (10)), but the differences between the figures remain even if k is chosen according to their equation.

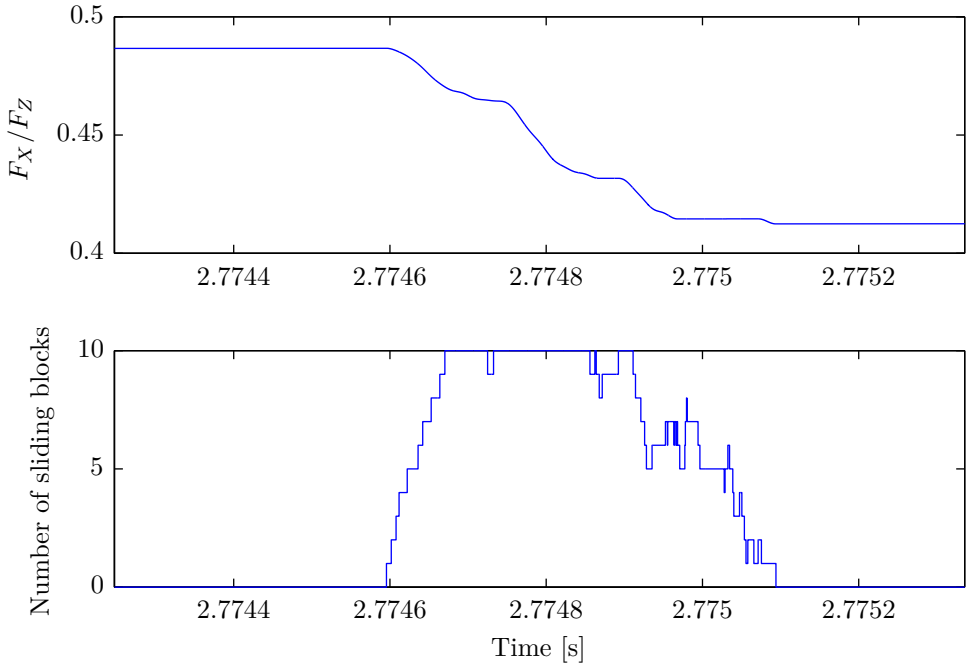

Figure 4.5: A closer look at the first global sliding event in Figure 4.4 shows that the dynamics of each event is richer than Figure 4.4 suggests.

Figures 4.4 and 4.6 compare well to the experimental data in Figure 3.3b, which is promising.

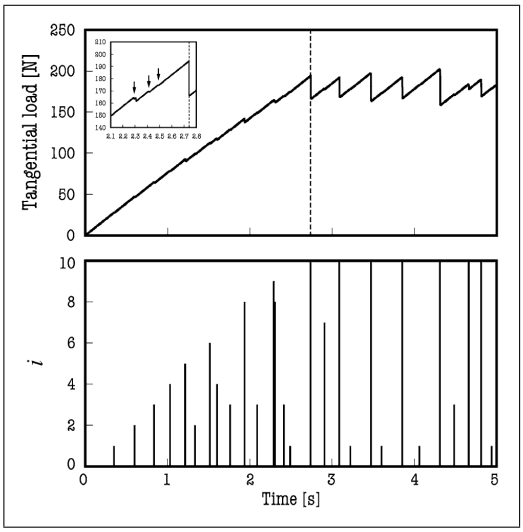

Figure 4.6: The same output as Figure 4.4, taken from the article of Maegawa et al. [36]. Because there is no randomness in the model, differences in roundoff error and the exact implementation of the starting and stopping of each block gives differences in the number of sliding blocks, here denoted i.

4.3.2 Damping: a simple improvement of the model

Shear and normal force profiles are used to study the triggering and arrest of sliding events. With Amontons–Coulomb friction the relationship becomes particularly clear: events trigger when the external shear force on a node (excluding friction) exceeds the static friction threshold, and they arrest when the propagating pulse fails to bring the force on the next node in line above this threshold.

Figure 4.7 shows the shear force distribution during the precursor phase. In the model of Maegawa et al. [36], $\eta = 0$ always, and this gives Figure 4.7a. The shear force is highly discontinuous, with alternating local maxima and minima with only a few grid points in between. This result is independent of N in that the distance between local extremes remains on the grid spacing whatever the resolution, and is unphysical as it implies a strong dependence on the discrete grid.

To reduce the number and amplitude of these discontinuities, I have followed Knopoff and Ni [33] and introduced a damping on the relative motion of the blocks. It appeared without motivation in equation (4.9) and Table 4.1. In Appendix B.2 and B.3 I derive the dispersion relation of the model with damping, and use this to determine the appropriate magnitude of η. The conclusion is that the mode with the highest frequency is damped the most, and that this mode is critically damped at $\eta = \sqrt{km}$ (equation (B.33)). A suitable level of underdamping is obtained with $\eta/\sqrt{km} = \sqrt{0.1}$. Figure 4.7b shows that the discontinuities in the shear force profile are smoothed out by the introduction of damping. Note that to the left of the arrest point, the shear force lies at the kinetic friction level. This observation will be used in Section 4.4 to predict the length of precursors.

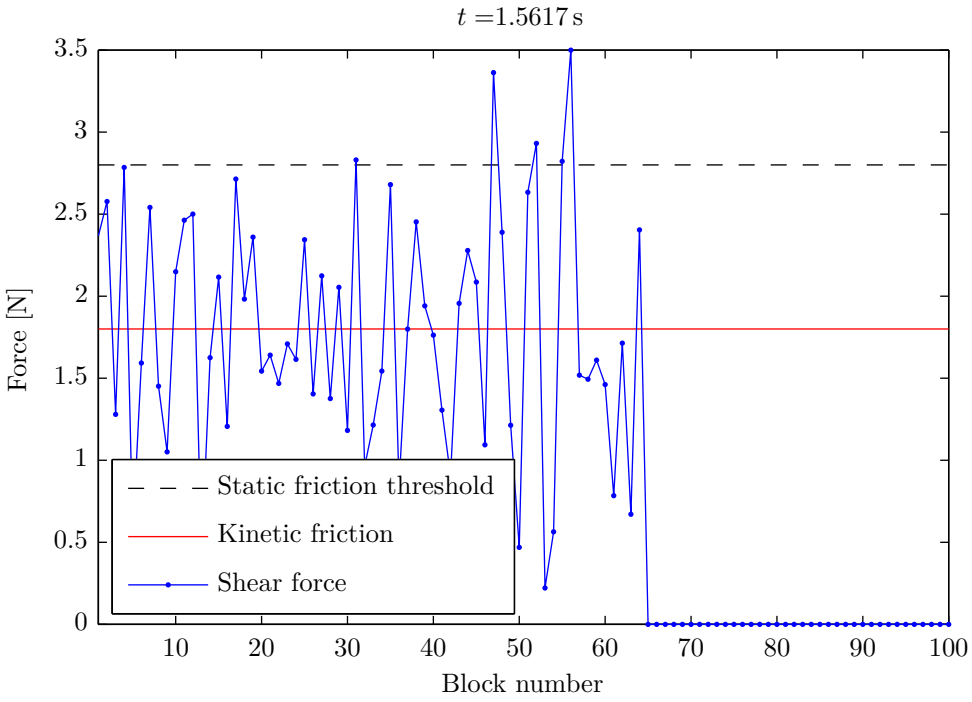

(a) No damping term.

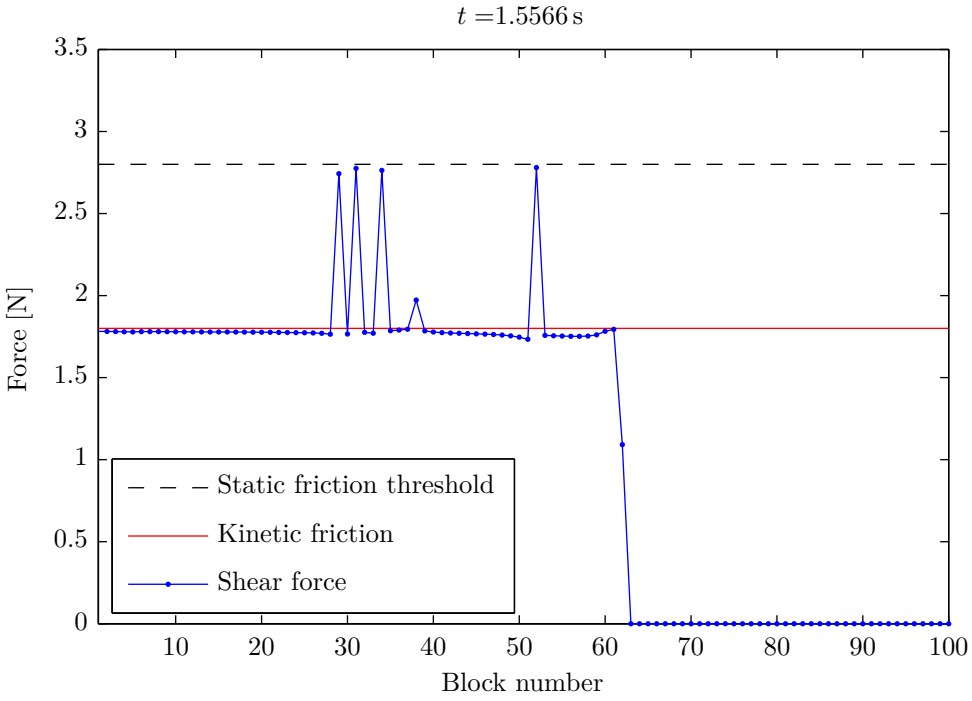

(b) Damping $\eta = \sqrt{0.1}\sqrt{km}$.

Figure 4.7: Damping of the relative motion of the blocks largely removes the unphysical oscillations in the shear force distribution. $N = 100$, $\theta = 0$, $\Delta t = 10^{-8}$ s. The snapshots have been taken *during* events, which is particularly clear in (a): shear forces larger than the static friction threshold are due to inertial effects and can only occur when the system is out of equilibrium.

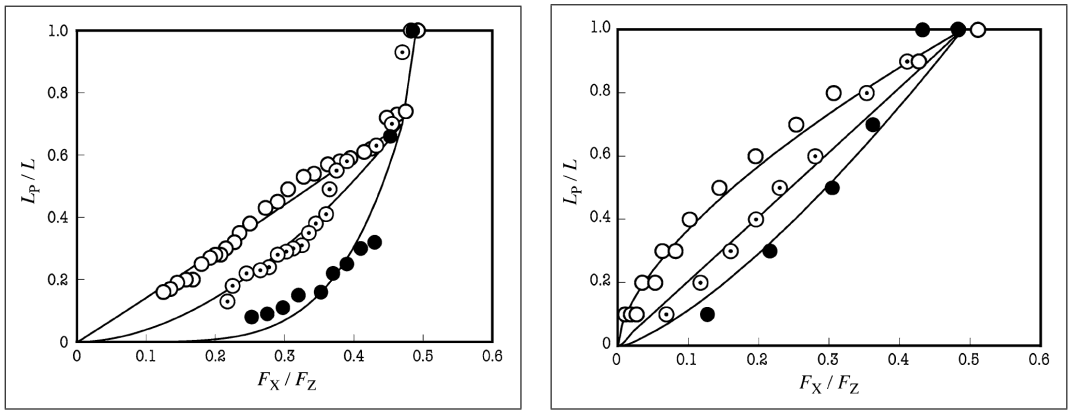

(a) Experimental results. **(b)** Simulation results.

Figure 4.8: Relationships between the length of precursors and the driving force, taken from Maegawa et al. [36]. Uniform normal loading (dotted circles) and two opposite non-uniform loading conditions corresponding to $\theta = 0.833$ (open circles) and $\theta = -0.833$ (filled circles). (a) is the same as Figure 3.7.

4.4 Length of precursors in the side driven model

Figure 4.8a shows the length L_p of precursors as a function of the driving force F_X as measured by Maegawa et al. [36] in their experiments. The same relationship can be measured in the model. At least two definitions of L_p are possible:

- L_p equals the maximum number of blocks moving at the same instant in time during the event
- L_p is the position of the rightmost block to move during the event.

The former is the one adopted by Maegawa et al. in their simulations, while I have adopted the latter, which I believe is most similar to the experimental measure. One should remember that all events nucleate at the trailing (left) edge; since the starting point is always the same, measuring the rightmost point means measuring the extent of the event. The two definitions are subtly different because the first blocks to start sliding sometimes stop sliding while the event continues to propagate towards the leading edge.

Figure 4.9 shows L_p–F_X for the 1D model. A major discrepancy with Figure 4.8 is the number of precursors, which is much higher in my numerical results. As will be discussed in Section 4.6 the number of events scales linearly with N, a shortcoming of the side driven 1D model that was not addressed by Maegawa et al.. The shapes of the curves are N independent, but also compare poorly to the experimental results. For $\theta = 0.833$ the curvature is much too large, for $\theta = -0.833$ the numerical result is slowly varying while the experimental curve has a sudden change in slope near $F_X/F_Z = 0.45$, and overall, the quantitative fit is poor. Even so, the results are interesting, in particular because they can be predicted analytically, as indicated by the drawn lines.

4.4.1 Analytical prediction of L_p–F_X

When the whole block is at rest between events, force balance requires $\sum_i f_i = -F_X$. Additionally, local force balance requires f_i to exactly cancel the force on node i from

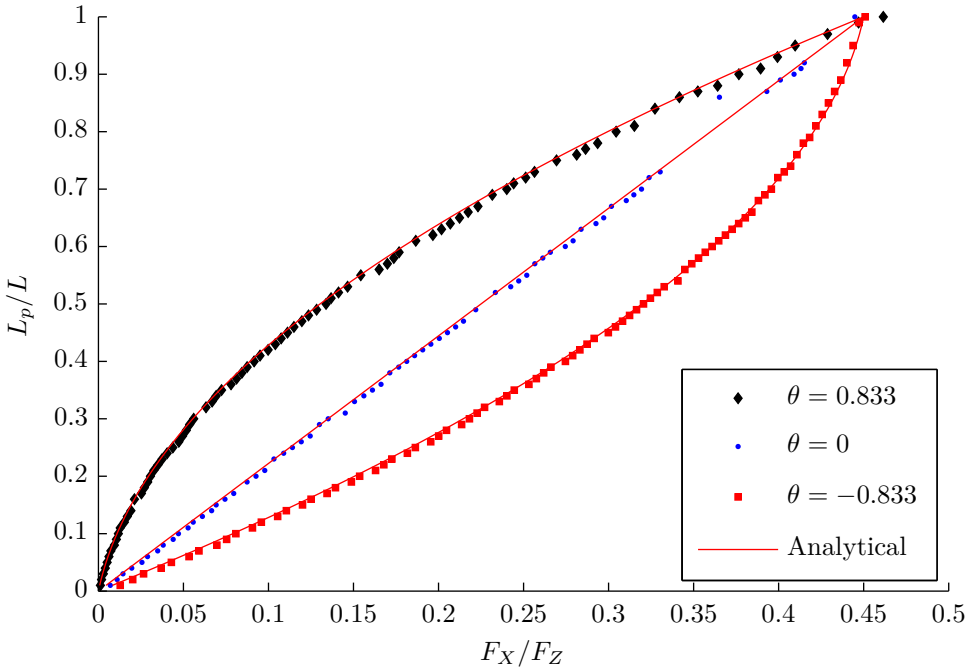

Figure 4.9: The effect of non-uniform static loading on the length of precursors. Precursors shorter than the ones preceding them have not been included in the figure. $N = 100$, $\Delta t = 10^{-8}$ s, other parameters as in Table 4.1. The analytical predictions are derived in Section 4.4.1. F_X was measured at the triggering time of the events.

the springs connected to it. In the side driven model this means that f_i remains at its initial value until block $(i-1)$ starts moving. If j is the index of the block on the end of the precursor,

$$F_X = -\left(\sum_{i=1}^{j+1} f_i^{\text{modified by precursor}} + \sum_{i=j+2}^{N} f_i^{\text{still has initial value}}\right). \tag{4.20}$$

Note that for large N, F_X takes approximately the same value before and after each event; this will be shown in Section 4.6.

The L_p–F_X relationship now follows from the assumption that along the precursor $f_i \approx -\mu_k w_i$. The assumption is based on output from the simulations, which shows this behaviour, see Figure 4.7b. There are deviations, a typical example of which is a spike at the end of the precursor or in the middle of the sample where the spring forces just failed to surpass the static friction threshold, but on average the approximation is good. When N is large the deviations can be neglected. For each j one can now find the corresponding force by the summation

$$\boxed{F_X = -\left(\sum_{i=1}^{j} \mu_k w_i + \sum_{i=j+1}^{N} f_i^{\text{initial}}\right).} \tag{4.21a}$$

Note that moving f_{j+1} between the sums is a one-node effect and as such is unimportant.

With the jth block being on the end of the precursor, the length of the precursor is

$$\boxed{L_p = \frac{j-1}{N-1} L \approx \frac{j}{N} L,} \tag{4.21b}$$

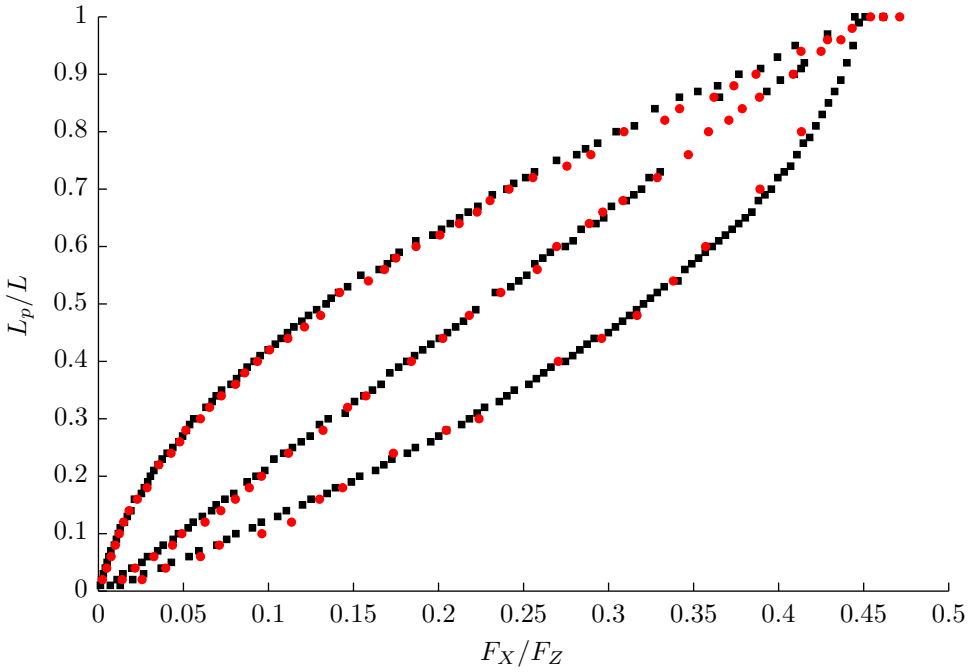

Figure 4.10: Rescaling L_p–F_X with L and F_Z produces a data collapse. Black squares are the data from Figure 4.9. Red circles are data for $L = 1000$ mm, $F_Z = 150$ N, $N = 50$, $\Delta t = 10^{-7}$ s, $\theta = 0, \pm 0.833$, other parameters as in Table 4.1. Precursors shorter than the ones preceding them have not been included in the figure. F_X was measured at the triggering time of the events.

where the $(j-1)$ reflects that in physical coordinates the leftmost block is at 0 and the rightmost is at L. For large N, the approximation is good.

For $j = 1, 2, \ldots, N$, equations (4.21a) and (4.21b) predict the L_p–F_X curve. Figure 4.9 shows that this analytical solution is in excellent agreement with the simulation results.

4.4.2 Rescaling with L and F_Z

To make the results of the previous section more general, rescale L_p and F_X with L and F_Z, respectively. In this way, data collapse is obtained for simulations made with different L and F_Z values, as confirmed by Figure 4.10.

That L_p should be scaled by L follows directly from equation (4.21b). Simply divide by L and observe that the right hand side becomes independent of all physical variables.

The rescaling of equation (4.21a) is a bit more subtle. The first term is straightforward: $w_i \propto F_Z$ by equation (4.8). The second term vanishes if $f_i^{\text{initial}} = 0$ for all i. It is also proportional to F_Z if a nonzero initial friction is introduced to imitate frustrated Poisson expansion as in Section 4.4.3. If the initial friction is not proportional to F_Z, rescaling F_X by F_Z will fail to produce data collapse.

4.4.3 L_p–F_X with an initial shear force profile

In the experiments, Poisson expansion gives rise to a nonzero initial shear force profile at the sliding interface even with $F_X = 0$, see Figure 3.9, from Ben-David et al. [7]. By

equation (4.21a), the agreement between the model results and Figure 4.8a should improve if the initial shear force profile is chosen to match the experimental one. Maegawa et al. [36] do not report the shear force profile, and of course, one cannot expect the profiles in experiments with different loading mechanisms and geometries to be equal, but nevertheless, a good idea of the quantitative importance of the initial force profile can be obtained by imposing a profile similar to Figure 3.9. If the approach proves successful, an estimate of the relevant initial force profile can be obtained e.g. by finite element calculations; the boundary condition between the slider and the track is complete frictional pinning (full stick).

As the normal load is increased to its desired value, the slider's natural deformation is different from that of the track because of geometric mismatch. However, friction at the interface pins the slider to the track, storing elastic energy. The difference in the slider and track elongation because of geometric mismatch can be approximated by equations (2.6) and (2.7) in the forms

$$\frac{\Delta L_z}{L_z} = \frac{1}{E}\frac{F_Z}{L_x L_y} \tag{4.22}$$

$$\Delta L_x = -\nu\frac{\Delta L_z}{L_z}L_x \tag{4.23}$$

$$= -\frac{\nu}{E}\frac{F_Z}{L_y}, \tag{4.24}$$

with ΔL_x positive because F_Z acts in compression. The formula predicts that the track, being thicker in the transverse direction, will tend to elongate less than the slider. In the 1D model there is no Poisson expansion, but the initial shear stress profile can be included by assigning a relative displacement of the blocks, as explained in Section 4.2.2.

The top part of Figure 4.11 shows the model with

$$F_{\mathrm{desired},i} = 0.9\mu_s w_1 \left(2\frac{i-1}{N-1} - 0.5\right)^q \tag{4.25}$$

which is close to the maximum asymmetry that can be assigned without exceeding the static friction threshold anywhere. L_p–F_X curves for different q are shown in the bottom part of Figure 4.11. The agreement with experiment is better than in Figure 4.9. The shape of the curve is nearest to experiment for $q = 1$ in that the slope changes significantly as L_p approaches L. However, this initial condition does not fit well with the experimental ones in Figure 3.9, and for $q = 3$ and $q = 5$, the change of L_p–F_X is much smaller. In summary, imposing a realistic initial shear force changes the shape of L_p–F_X, but the effect is not sufficient to explain the experimental results.

4.5 Crack front velocities

In Section 3.2.4 I defined the crack front or rupture front as the boundary between the slipping and pinned parts of the sliding interface. Experimentally, its position as a function of time is obtained from $A_{\mathrm{real}}(x,t)$ data like those in Figure 3.5. In numerical models with a well defined static friction threshold, like the present model, the crack front can e.g. be obtained from a space-time plot of the local sliding velocity v (Figure 4.12): a pinned node has $v = 0$ while a slipping node has $v \neq 0$.

The crack front velocity v_{crack} is the inverse of the slope between the slipping and pinned regions in Figure 4.12. A front that moves far in a short time interval is fast; a

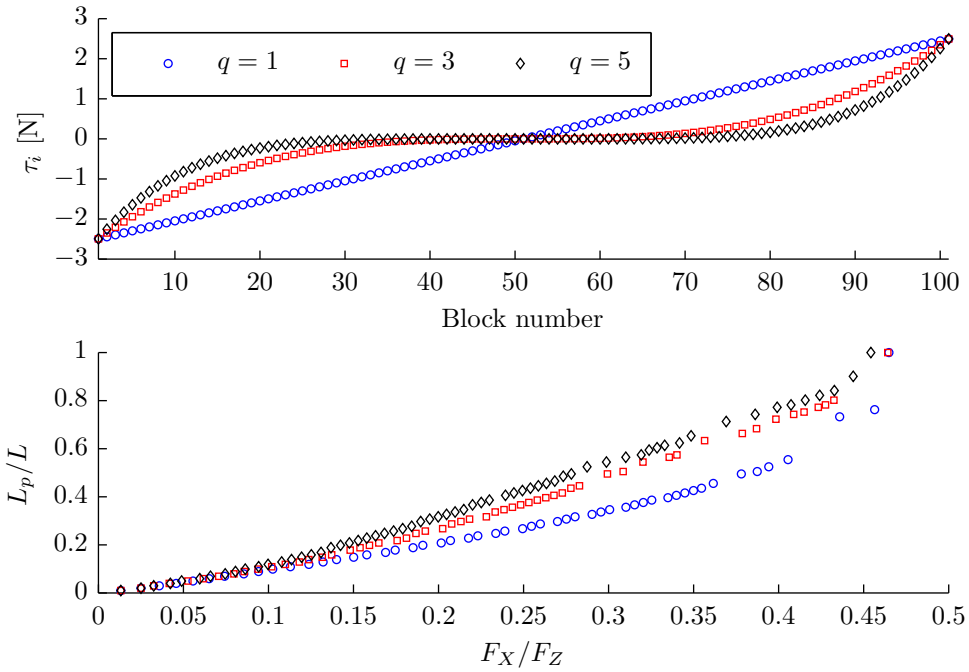

Figure 4.11: The effect of the initial shear force profile on the length of precursors. Precursors shorter than the ones preceding them have not been included in the figure. $N = 101$, $\Delta t = 10^{-8}$ s, other parameters as in Table 4.1.

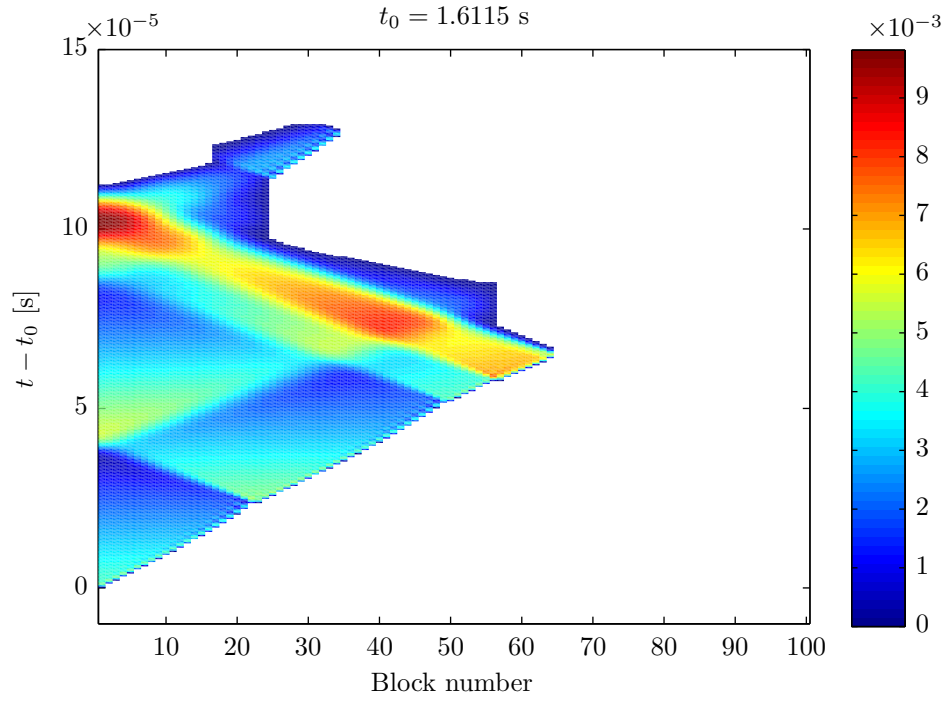

Figure 4.12: A space-time plot of the local slipping velocity. The colourbar represents $v(x,t)$ in m/s. $N = 100$, $\theta = 0$, $\Delta t = 10^{-8}$ s, other parameters as in Table 4.1.

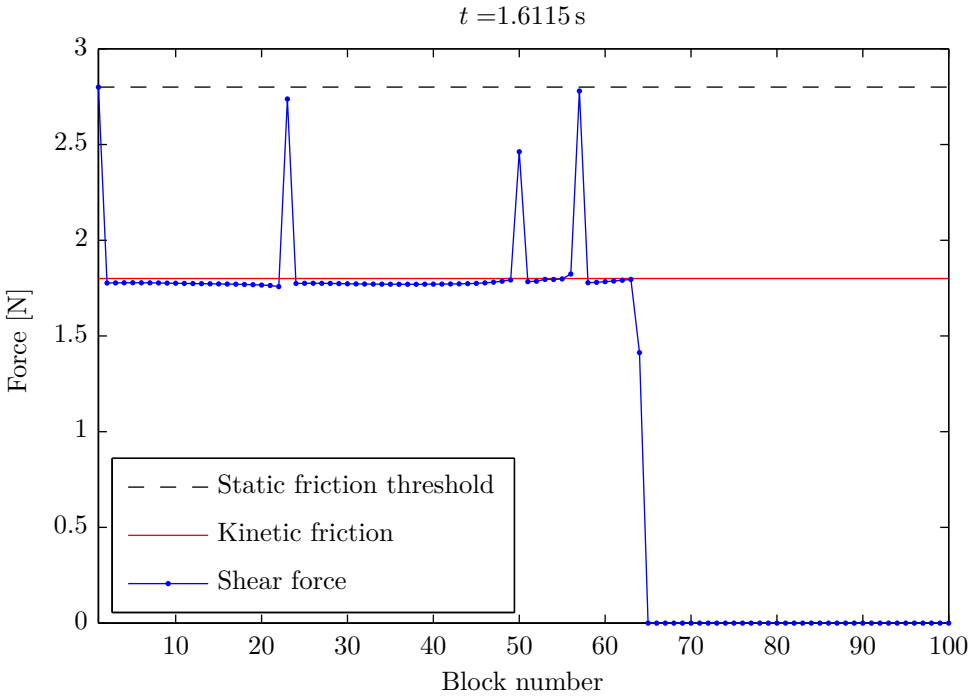

Figure 4.13: The shear force distribution immediately before the event in Figure 4.12.

front that takes a long time to traverse the interface is slow. From the figure one can see three distinct locations where the crack front velocity changed by a small amount. At the same locations, disturbances travelling back towards the trailing edge originated. Figure 4.13 shows that these locations are in fact the positions of local changes in the shear force profile.

Amundsen [1] has made an extensive study of the crack front velocities in the present model. Knopoff et al. [34] and Muratov [39] studied the effect of the prestress τ at event nucleation, in the top driven model introduced in Section 4.7. My treatment of the crack front velocities will be focusing on the 1+1D model that is introduced in Chapter 5.

4.6 Artefacts of the side driven model

In Section 4.3.1, Figure 4.4, the loading curve was seen to agree well with the experimental loading curve. However, this result is not robust to changes in the resolution. Figure 4.14 repeats Figure 4.4 for easy comparison with its $N = 100$ counterpart. For $N = 100$, the stick–slip curve has become almost flat, and the number of events has increased tenfold. Clearly, the choice of N greatly influences the behaviour of the system.

The combination of the properties that

- the model is one-dimensional
- static friction exactly cancels the sum of other forces on each node
- external load is imposed on the leftmost node only

implies the pathological behaviour that there is no transfer of force along the interface until slip occurs. This is fundamentally different from experiments, in which the dimension out of the plane of the interface serves as a pathway for force/stress transfer. To

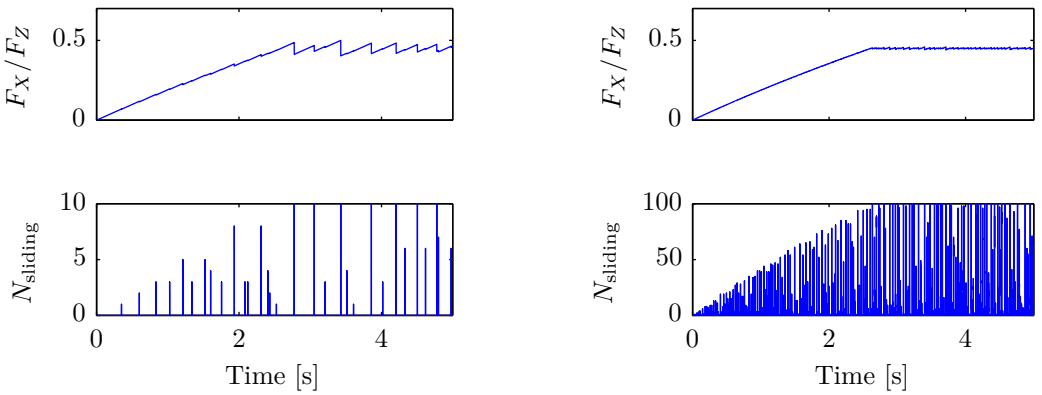

(a) $N = 10$, same data as Figure 4.4.

(b) $N = 100$, $\theta = 0$, $\Delta t = 10^{-8}$ s, $\eta = 0$, remaining parameters as in Table 4.1.

Figure 4.14: In the side driven 1D model, the number of events increases with N, and the results become resolution dependent.

put it plainly: when one part of the slider slips, the bulk is deformed, and this will affect the stress at the interface also away from the slipped region.

The differences between $N = 10$ and $N = 100$ shown in Figure 4.14a and 4.14b are due to the lack of force transfer. Let the *loading zone* be the part of the sample in which the force changes because of the loading between events. Obviously, in the present model the loading zone is just the leftmost block, on which the driving force acts. Now, the force increment required to nucleate an event equals the force increment required to push this node above the static friction threshold, which is proportional to $w_1 \propto 1/N$. Part of this force is relaxed upon the movement of the leftmost block, and part is transferred to the next block in line. The associated change in the loading curve is of the order of the force increment, and so tends to zero as N is increased.

The force at the onset of global sliding, the global static friction threshold $\mu_s^{\text{global}} F_Z$, is nearly independent of N. Under the approximation $\tau_i = -f_i \approx \mu_k w_i$ along the precursors, $\mu_s^{\text{global}} \approx \mu_k$. Since the force increment between events goes like $1/N$, then, the number of events must be proportional to N. Amundsen [1] investigates the N dependence in more detail and finds that the number of events, and therefore also the amplitude of the drops in F_X, is indeed linear. This model, therefore, cannot be used to understand the number of any type of event.

In Section 4.1.2 I chose the local mass and stiffness according to the properties of the whole slider: $m = M/N$, $k = (N-1)EA/L$. I did not argue that this was the best way to choose m and k, and in fact, I am not sure that it is. From the viewpoint that the model is a discretisation of the 3D slider, the blocks of the model become very thin slices as N becomes large. To put it another way: with $l = L/(N-1)$ as the distance between / size of each node, $m \propto l$ in the model, while in 3D, $m \propto l^3$ would be the scaling. For large N the blocks are, perhaps, too massive, and choosing m according to the stress domain picture of Persson [42] might be more appropriate. Persson also argues for another choice of k, but I hold that reproducing the stiffness of the whole slider is important because it couples to the slip length of events, and therefore to the relaxation of the force in the driving spring.

Changing m changes the internal time scale of the system. Since I use $\eta \propto \sqrt{km}$,

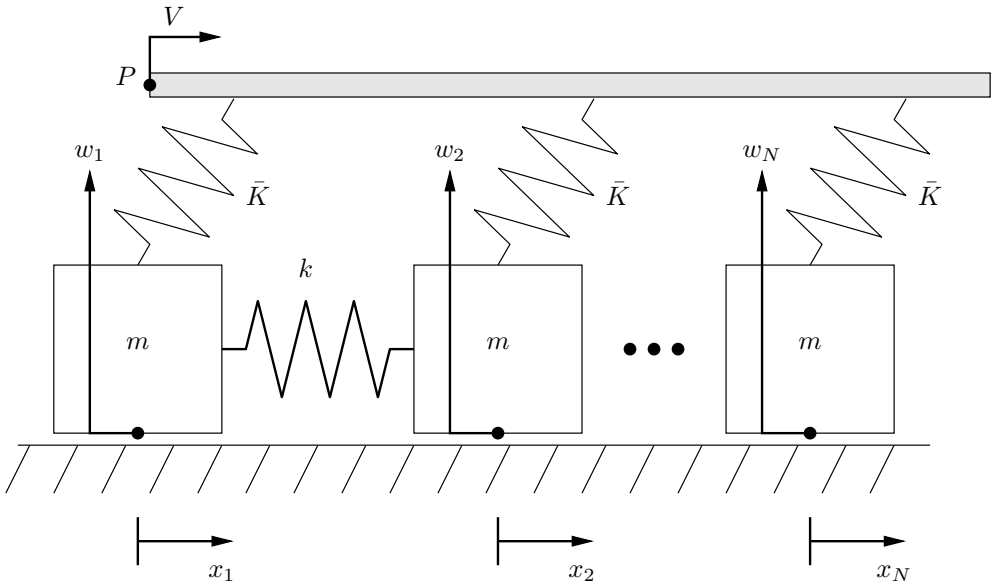

Figure 4.15: A spring-block system driven from the top. The rigid rod, one point on which is labelled P, moves to the right with constant speed V. The model is strictly one-dimensional, all forces are directed along the x-axis.

the relative importance of damping and inertia stays the same. I have stayed with $m = M/N$.

4.7 A 1D spring-block model with top/uniform driving

The side driven model has strong resolution dependence because the driving force is applied in a single point. All slip/sliding events must nucleate at the trailing edge, because no force is transmitted to the second block before the trailing edge (first) block is displaced. To get a model which incorporates the possibility for other nucleation sites, I have modified the loading section slightly, so that every block is coupled to the driving stage with its own spring. This is the other extreme of loading conditions, as it gives uniform driving of all nodes. This remedies the problem that the number of events scales with N.

The top driven version of the model is very similar to the homogeneous Burridge–Knopoff model, which has been studied extensively in the global sliding regime (Section 3.3.1). Here, I study the *onset* of sliding only.

I implemented uniform driving by coupling every node to a rigid plate. The model is still one-dimensional: the springs coupling the blocks to the top plate only exert force along the axis of displacement of the plate. The springs between the blocks and the driving plate are connected in parallel, and to mimic the force on the system as the point P moves in the side driven model, each of them is assigned a stiffness $\bar{K} = K/N$. The system is shown in Figure 4.15.

The equations of motion change slightly with respect to (4.3) and become

$$\begin{cases} m\ddot{x}_1 &= k(x_2 - x_1) &+ F_{X,1} &+ f_1 &+ F_{\eta,1}, & \\ m\ddot{x}_i &= k(x_{i-1} - 2x_i + x_{i+1}) &+ F_{X,i} &+ f_i &+ F_{\eta,i}, & \text{for } 2 \le i \le N-1, \\ m\ddot{x}_N &= k(x_{N-1} - x_N) &+ F_{X,N} &+ f_N &+ F_{\eta,N}, & \end{cases} \tag{4.26}$$

with

$$F_{X,i} = \bar{K}(X - x_i) = \bar{K}(Vt - x_i) \qquad \forall i. \tag{4.27}$$

Unless some non-uniformity or disorder is introduced all the blocks will reach their static friction threshold at the same time, and no relative displacement of the blocks will occur. The options include

- using $\theta \neq 0$, which gives a static, non-uniform normal loading,
- incorporating the effect of torque on the normal force profile, which gives a dynamic non-uniformity,
- letting μ_s be different for each block and choosing $\mu_{s,i}$ from a probability distribution.

The first option is straightforward. Including the effect of loading torque requires some calculations that I will make in the following section. The simulations I have performed with disorder in the friction coefficients have not been pursued enough to give interesting results, and I will not discuss them here.

4.8 Friction-induced torque

In this section I do not consider the 1D model, but the more general case of a block subject to a driving force and a counteracting friction. The subject of interest is the effect friction-induced torque has on the normal force distribution, which is also studied by Scheibert and Dysthe [50].

For an object at rest, the distribution of the normal force W across the interface supporting the object is not fixed by requiring the net force and net torque to be zero. Consider, for instance, a cube lying on a flat track under the influence of gravity and normal force alone. Gravity exerts no torque about the centre of mass, since the gravitational force has no arm with respect to this point. For any symmetrical distribution of the normal force, not necessarily uniform, the net force and net torque will be zero. More complicated distributions that match the zero force and torque criteria can easily be constructed as well.

Even so, apart from edge effects there is no obvious reason to assume that the normal force is non-uniformly distributed (on a scale much larger than the size of asperities) unless we know something of how the block came to rest. This changes when we start pushing the block. Consider e.g. the situation shown in Figure 4.16, in which a slider of height H and length L is pushed to the right by a force F_X acting in a point at height h above the slider-to-track interface. The driving force exerts a torque

$$\boldsymbol{\tau} = \mathbf{r} \times \mathbf{F}, \tag{4.28}$$

$$\tau_{F_X} = F_X \left(h - \frac{H}{2} \right) \tag{4.29}$$

along the y-axis. When $h > H/2$ the torque is in the positive y-direction, whereas for $h < H/2$ the torque is in the negative y-direction. Friction acts at all points along the interface, but since all these points have the same arm with respect to the centre of mass, the total torque due to friction is simply

$$\tau_f = -f\frac{H}{2} = F_X \frac{H}{2}, \tag{4.30}$$

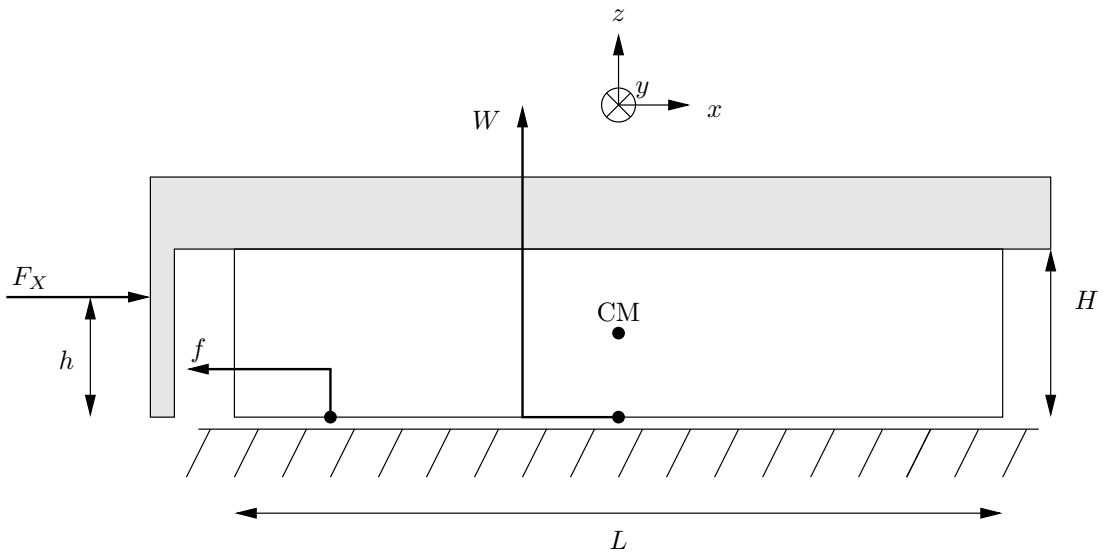

Figure 4.16: The forces acting on a block at rest. The friction force F_f and normal force W are distributed along the entire interface. The grey object is a rigid plate to which the sliding block is glued. The driving force can be applied at any height above the slider-to-track interface. Adapted from Scheibert and Dysthe [50].

where the second equality holds while the block remains at rest, since F_X and f are the only forces acting in the x-direction. The sum of these torques must be balanced exactly by an asymmetry in the distribution of the normal force if the block is to remain at rest.

Assuming a linear distribution of the normal force, which is a good approximation if the sample is long and thin (see Fig. 2 of [50]), makes the problem analytically tractable. Writing the normal force within an interval of width $\mathrm{d}x$ at point x as

$$w(x) = \bar{w}(x)\,\mathrm{d}x = \left(F_Z + g\frac{x}{L/2}F_X\right)\frac{\mathrm{d}x}{L}, \tag{4.31}$$

i.e. splitting the normal force into a constant and a linear term, will be convenient when returning to the 1D model. The total normal force on the block is

$$W = \int_{-L/2}^{L/2} \bar{w}(x)\,\mathrm{d}x. \tag{4.32}$$

The constant term in equation (4.31) gives no net contribution to the torque. Multiplying the linear term by x, the arm of the normal force at point x, and integrating along the interface gives

$$\tau_W = \int_{-L/2}^{L/2} g\frac{2x}{L}F_X x\frac{\mathrm{d}x}{L} \tag{4.33}$$

$$= g\frac{LF_X}{6}, \tag{4.34}$$

in the negative y-direction for positive values of g. This should balance the torques from

the driving force and friction, i.e.

$$\tau_{F_X} + \tau_f + \tau_W = 0 \tag{4.35}$$

$$F_X \left(h - \frac{H}{2} \right) + F_X \frac{H}{2} - g \frac{L F_X}{6} = 0 \tag{4.36}$$

$$g = \frac{6h}{L}. \tag{4.37}$$

The discrete versions of equations (4.31) and (4.32) are

$$w_i = \frac{F_Z}{N} + \frac{g}{N} \frac{2i - N - 1}{N - 1} F_X, \qquad W = \sum_{i=1}^{N} w_i. \tag{4.38}$$

Recall that W is equal to F_Z, but oppositely directed.

4.9 Comparison with the model of Scheibert and Dysthe

As was mentioned above, if no friction-induced torque is applied and the static load is uniform, there will be no precursors. As g increases this stays true until, for some value of g, the first slip event arrests before reaching the leading edge. If lifting of the trailing edge ($w_1 < 0$) is to be avoided (not a necessary condition, but a convenient one), the limiting value of g is determined by the maximum value of F_X, which is $F_X = \mu_s^{\text{global}} F_Z \approx \mu_k F_Z$, so that

$$g < \frac{F_Z}{\mu_k} \tag{4.39}$$

should be fulfilled. This limits the number of precursors that can be obtained by increasing g.

Another way to increase the number of events is to let μ_s approach μ_k. With $\mu_s = 0.55$, $\mu_k = 0.45$ and $g = 1.2$, the top driven model produces Figures 4.17 and 4.18. This value of g corresponds to $h = 20$ mm in equation (4.37), which equals H, the height of the sample in [36].

Scheibert and Dysthe [50] proposed an analytical solution of essentially the same physical system: an elastic block uniformly coupled to a rigid driving stage, and a friction-induced torque affecting the normal force profile. Even though the exact loading conditions are dissimilar, it is interesting to compare the output from the present model to their theory. Their main assumptions are that:

- the normal force profile is linear and depends on F_X as in equation (4.31).
- In each event, triggered by $\tau > \mu_s \sigma$ occurring in principle anywhere but in practice at the trailing edge, the part of the slider where $\tau > \mu_k \sigma$ relaxes to $\tau = \mu_k \sigma$. There is no change in τ along the rest of the slider, on the right side of the precursor arrest point.

Of course, their first assumption cannot be tested in the present model, as the normal force has to be imposed directly here as well.

Figure 4.18 violates the second assumption in two important regards. Firstly, the event propagated into the region where $\tau < \mu_k \sigma$, which is clear from comparing the panels from the same event. Secondly, the shear force along the precursor, although

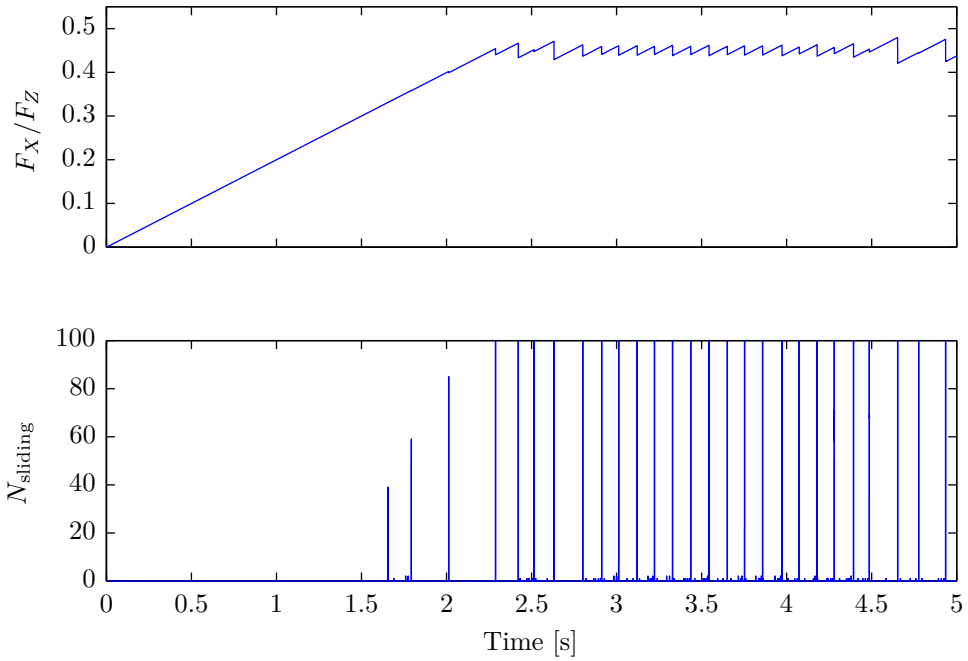

Figure 4.17: The loading curve and the number of sliding blocks in the top driven model with torque. $N = 100$, $\mu_s = 0.55$, $g = 1.2$, $\theta = 0$, remaining parameters as in Table 4.1.

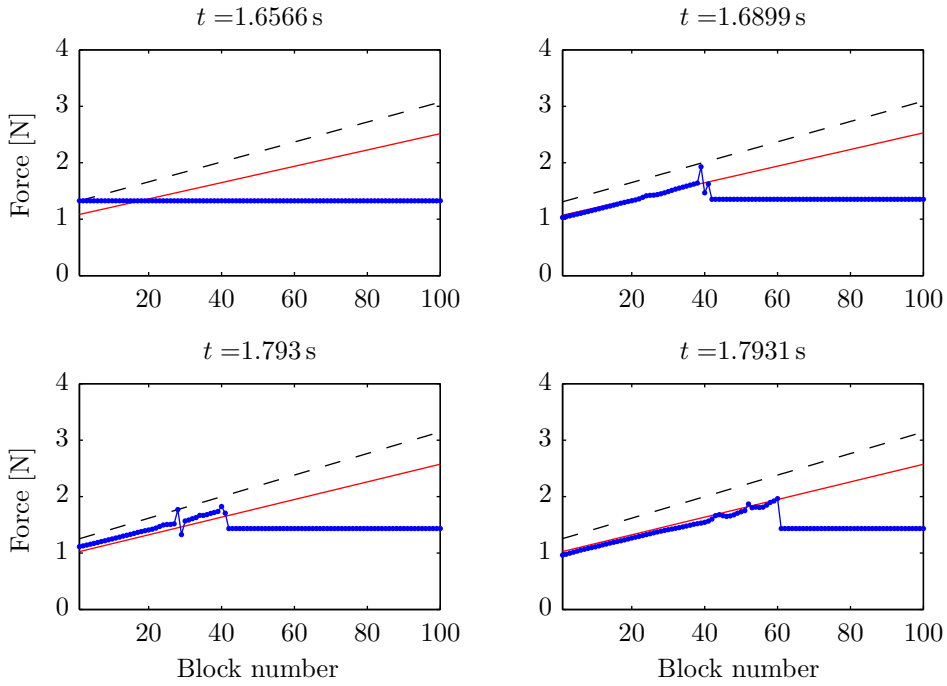

Figure 4.18: Evolution of the shear force (blue, with markers), dynamic friction level (red, drawn) and static friction threshold (black, dashed) in the top driven model with torque, for the same simulation as Figure 4.17. The two topmost panels show the triggering and arrest state of the first event. The two bottommost panels show the triggering and arrest state of the fifth event. The second through fourth events each involve only a few nodes, and they are hardly visible in Figure 4.17. $N = 100$, $\mu_s = 0.55$, $g = 1.2$, $\theta = 0$, remaining parameters as in Table 4.1.

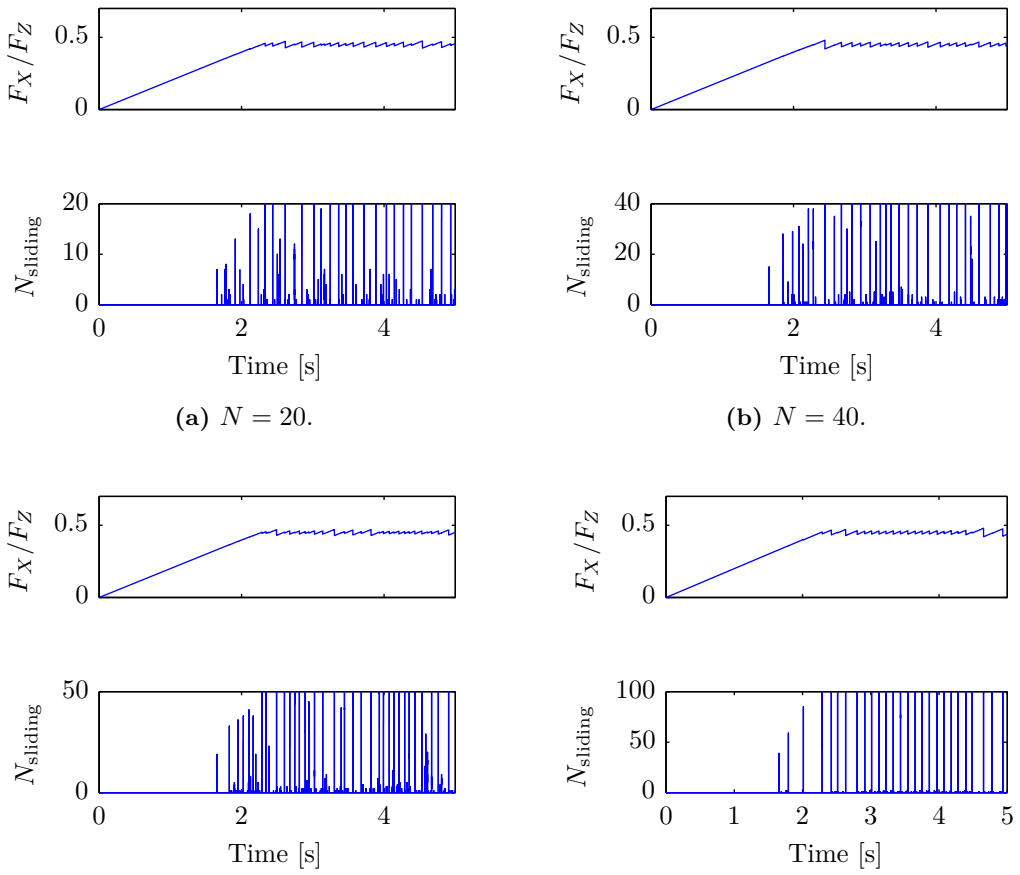

(a) $N = 20$. **(b)** $N = 40$.

(c) $N = 50$. **(d)** $N = 100$, same data as Figure 4.17.

Figure 4.19: In the top driven 1D model, the number of events does not *scale* with N (the details can still vary, though). $\mu_s = 0.55$, $g = 1.2$, $\theta = 0$, remaining parameters as in Table 4.1. In (d), the system apparently entered a nearly periodic stick–slip regime. Compare this figure to Figure 4.14.

close to $\mu_k\sigma$ along most of the precursor, has a spike at the end associated with the first block that did not overcome the static friction threshold; there are no such spikes in [50]. In the present model these spikes are typical, but not universal, as the bottom right panel shows. The presence of spikes in the shear force profile dominates the triggering of the following events. The assumption that each event nucleates at the trailing edge therefore breaks down and, unfortunately, means that the sequence of events will be highly different in the present model and in the theory of Scheibert and Dysthe.

Figure 4.19 shows that for uniform load, the number of events does not scale with N. It should be compared to Figure 4.14, which shows results for side driving.

4.10 Length of precursors in the top driven model

Figure 4.20 shows L_p–F_X for the top driven model with $g = 0$. I use $g = 0$ to make the comparison with results from the side driven model more straightforward. With no friction-induced torque there are no precursors for $\theta = 0$; in order to have precursors that nucleate at the trailing edge, $\theta > 0$ must be used. The scheme for predicting L_p–F_X is different from the side driven case, because equation (4.20) is no longer valid when all the blocks are influenced directly by the external loading force. One can proceed as follows.

Assume any value for F_X. Since the driving springs never detach, one can find the shear force on each block in two steps: first *assuming* that the block did not slip, and then allowing it to slip and obtain the dynamic friction value, if the block is found to have moved. In the first step, the friction force on each block is

$$f_i^{\text{assumed}} = f_i^{\text{initial}} + \frac{F_X}{N}. \tag{4.40}$$

If the force F_X is sufficiently large one will find that $f_i^{\text{assumed}} > \mu_s w_i$ near the trailing edge. In the next step, the force on all such nodes is set to $f_i = \mu_k w_i$. The excess force, the value of which will be discussed shortly, is then placed on the neighbours to the right, distributed such that they too have $f_i = \mu_k w_i$. This will require a well-defined number of nodes (unless $F_X > \mu_k F_Z$, in which case one will find that the event reaches the leading edge and therefore is not a precursor). The length L_p corresponding to the chosen value of F_X is simply the rightmost node that had to be assigned the dynamic friction level. Figure 4.21 illustrates the scheme. When a node moves, the amount of force it transfers to its neighbours depends on the relative importance of the internal springs of stiffness k and the driving spring of stiffness $\bar{K}$. If $k \gg \bar{K}$, the block's movement is halted by the forces from its neighbours well before there is any significant change in the driving force on it (unless the event is a global one). This is the case for the parameters in Table 4.1, and justifies the assumption of equal areas in Figure 4.21.

The analytical solution scheme agrees well with the simulation output. For uniform shear driving, no experimental data for L_p–F_X is available for comparison.

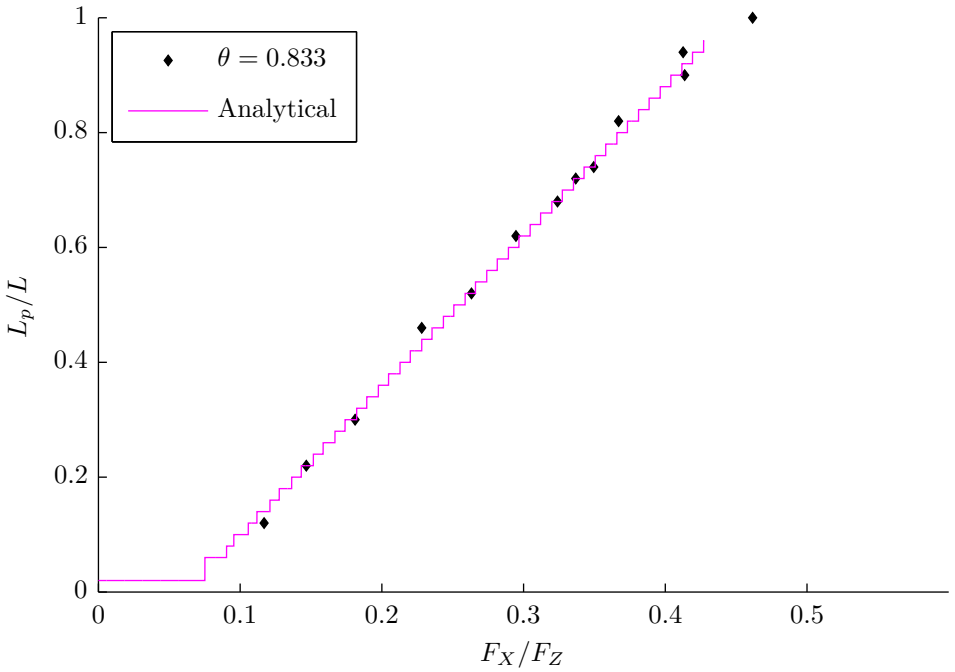

Figure 4.20: The length of precursors in the top driven model. $N = 50$, $\theta = 0.833$, $\Delta t = 10^{-7}$ s, $g = 0$, remaining parameters as in Table 4.1. The discreteness in the analytical solution is due to the discreteness of the lattice.

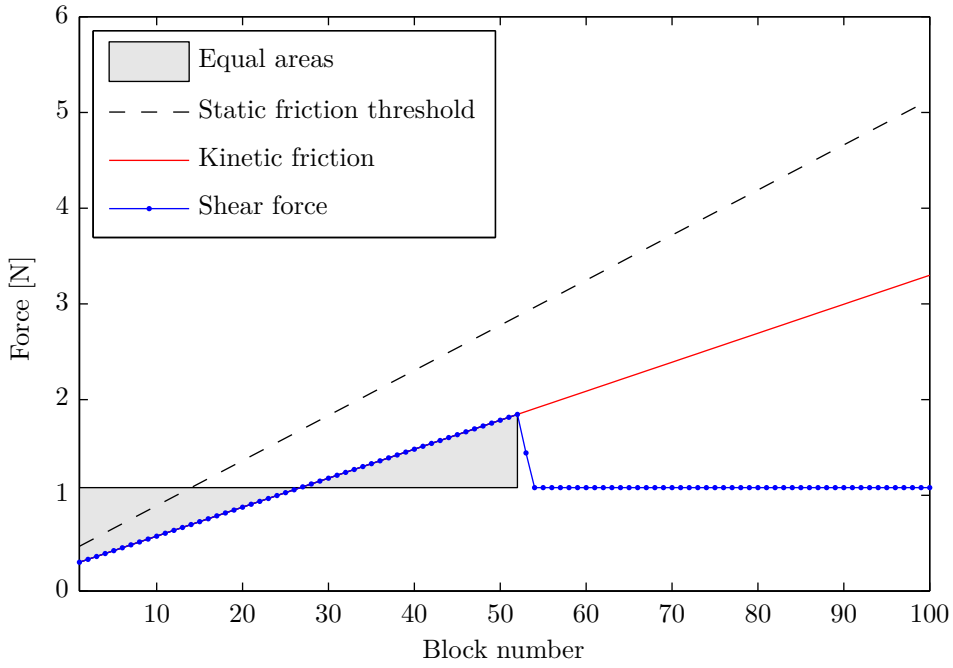

Figure 4.21: Suggested scheme for predicting L_p as a function of F_X in the top driven 1D model, see the text for details. Arbitrary parameters. The figure has been made as an illustration, it is not the result of a simulation. The scheme predicts L_p for any value of F_X in a two-step (imagined) process described in the text; in practice, events trigger as soon as the shear force reaches the static friction threshold.

4.11 Robustness of results

As the goal of the thesis is to reproduce spesific experimental results, I have not explored the parameter space of the 1D models thouroughly. I have, however, performed a few checks of the robustness of my results to changes in the friction law.

A straightforward modification of the model is to allow a small disorder in the friction coefficients, i.e. to draw μ_s and μ_k for each block randomly from a probability distribution. With uniform distributions of relative width on the order of a few percent, e.g. $\mu_s \in [0.69, 0.71]$, I find no appreciable changes in the results.

With an instantaneous change of a block's friction coefficient upon slip initiation, there is a discontinuity in the force on the block. This can be smoothened out by introducing a gradual transition from μ_s to μ_k, and in Chapter 6 I introduce a slip weakening friction law with a characteristic length ξ_μ. Whether this affects the results depends continuously on ξ_μ, which means that the Amontons–Coulomb laws, retrieved in the limit $\xi_\mu \to 0$, are not singular in the sense that my findings depend crucially on the discontinuity in the local friction force.

4.12 Summary

The 1D side driven model predicts a series of precursors nucleating at the trailing edge, in accordance with the experimental observation. The trend is an increase in the length L_p of precursors until the leading edge is reached and system-sized events occur. When changing from a uniform to a nonuniform normal load the model correctly reproduces the observation that at a given level of the shear force F_X, the precursors are longer (shorter) when the normal force at the trailing edge is lower (higher). However, the quantitative fit with experiments is poor, and the number of precursors scales with the system resolution N.

What will it take to improve the agreement with experiment? The experience with spring–block models that has been gained from the study of the 1D models helps answer this question. Whether a node sticks or slips is governed by the local shear and normal forces, and I expect that if the experimental force profiles are reproduced, other results will follow. For example, since the shear force profile only changes upon slip, the loading zone consists of the single leftmost node, while in experiments, changes in F_X affect a region near the trailing edge, because stress can be transferred through the bulk. The normal force in the model has to be imposed directly, and is chosen as a simple linear distribution for lack of knowing the real profile. In experiments, the normal force would change locally upon slip.

In Chapter 5 I will include the vertical dimension in the model. This improves the representation of the boundary conditions and the elastic interactions, and should lead to local forces in better agreement with experiment. In particular, stress transfer through the bulk becomes possible, and instead of imposing the normal force at the slider–track interface, it can be imposed on top of the slider, allowing the normal forces at the interface to evolve throughout the simulation.

Chapter 5

1+1D model

In Chapter 4 I studied the onset of dynamic friction in a 1D model. In the extraction of the numerical model from the full experimental setup, the elimination of the vertical dimension lacked a physical motivation; it was dropped for simplicity only. In the first section of this chapter I return the vertical dimension to the model system. I then describe the model in detail in Sections 5.2 and 5.3, while Section 5.4 presents some numerical technicalities. The parameters I use are given in Section 5.5. Sections 5.6 to 5.10 are concerned with results, except for Section 5.8, which presents a boundary condition that closely resembles the experiments I model. A summary of this chapter is deferred to Section 7.1.2.

5.1 Deduction of the model

In Section 4.1.1, the full experimental setup was reduced to a tractable model system bit by bit. Ignoring the frame keeping the slider and track in place and the transverse y-direction, in which there act no external forces, the model system is a 1+1D slider on a 1+1D track. The boundary between them is an ensemble of junctions, and both the slider and the track deform upon the application of external forces. I will treat the track as rigid, which is not unreasonable: the track is low and wide, while the slider is high and narrow. This approximation removes the track from the model system.

The model system, then, is an elastic 1+1D block with a frictional interface at its bottom. As in 1D, I model the frictional response as a locally applied Amontons–Coulomb law; this could easily be changed to another empirical law. As in 1D, the elasticity of the slider could be treated by FEM or similar approaches (see e.g. [6]), but I stick to a spring–block model. This minimises the differences between the 1D and 1+1D descriptions, which is very useful when the output from the two models is compared.

In Sections 5.2 and 5.3 I describe the model in detail. Parameters are given in Section 5.5. Section 5.8 introduces a refined representation of the experimental normal loading mechanism.

5.2 Internal interactions

Like the 1D model, the 1+1D model consists of blocks on a lattice and springs connecting them, see Figure 5.1. The horizontal and vertical springs have the same equilibrium lengths l and spring constants $k_1 = k$. The diagonal springs have equilibrium lengths

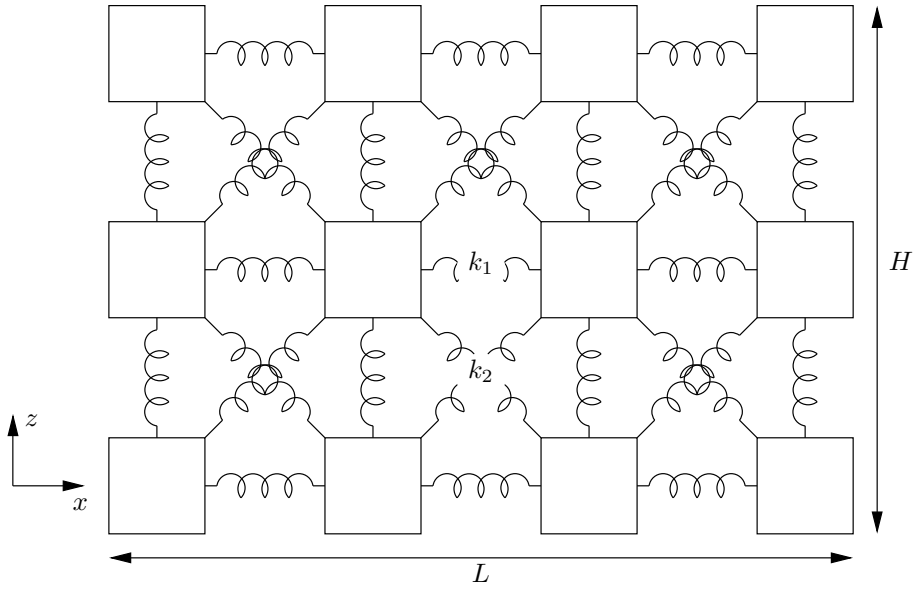

Figure 5.1: A spring-block model of an elastic continuum. The chosen numbers of blocks in each direction ($N_x = 4$ and $N_z = 3$) are a matter of the desired resolution as long as they respect the aspect ratio, i.e. the cells should be square.

$\sqrt{2}l$ and spring constants $k_2 = k/2$. Here, l is resolution dependent and given by $l = L/(N_x - 1) = H/(N_z - 1)$, N_x and N_z being the number of nodes in the x- and z-direction, respectively.

The force on block i from block j is

$$\mathbf{F}_{ij} = \begin{cases} k_{ij}\left(r_{ij} - l_{ij}\right)\left(\frac{\Delta x_{ij}}{r_{ij}}\hat{\mathbf{e}}_x + \frac{\Delta z_{ij}}{r_{ij}}\hat{\mathbf{e}}_z\right) & \text{when blocks are connected,} \\ 0 & \text{otherwise,} \end{cases} \tag{5.1}$$

where $\hat{\mathbf{e}}_x$ and $\hat{\mathbf{e}}_z$ are unit vectors along x and z, $\Delta x_{ij} = x_j - x_i$, $\Delta z_{ij} = z_j - z_i$, $r_{ij} = \sqrt{(\Delta x_{ij})^2 + (\Delta z_{ij})^2}$ and k_{ij} and l_{ij} are the stiffness and equilibrium length of the spring connecting the blocks.

5.2.1 Choice of lattice, relationship between k, E and ν

Whereas in 1D the uniformly spaced lattice is the obvious choice, there are multiple options to consider in 1+1D. These include triangular and square lattices with or without bond bending forces and with or without next nearest neighbour interactions. A good candidate should mimic the behaviour of a linear isotropic elastic continuum while not being too computationally expensive.

The naive configuration of a square lattice is one with central nearest neighbour interactions only. To see that this fails to reproduce linear elasticity, consider deforming the square cells to parallelograms without changing the distance between connected sites. This implies no restoring forces, and the whole lattice can be collapsed to a line. Replacing some of the springs by leaf springs whose end points are fixed to lattice sites remedies this, but this system has no Poisson expansion.

It is well known from modelling of condensed matter that the triangular lattice and the square lattice with nearest and next nearest neighbour interactions are more suitable candidates, the square lattice being preferred by some, e.g. Monette and Anderson [38],

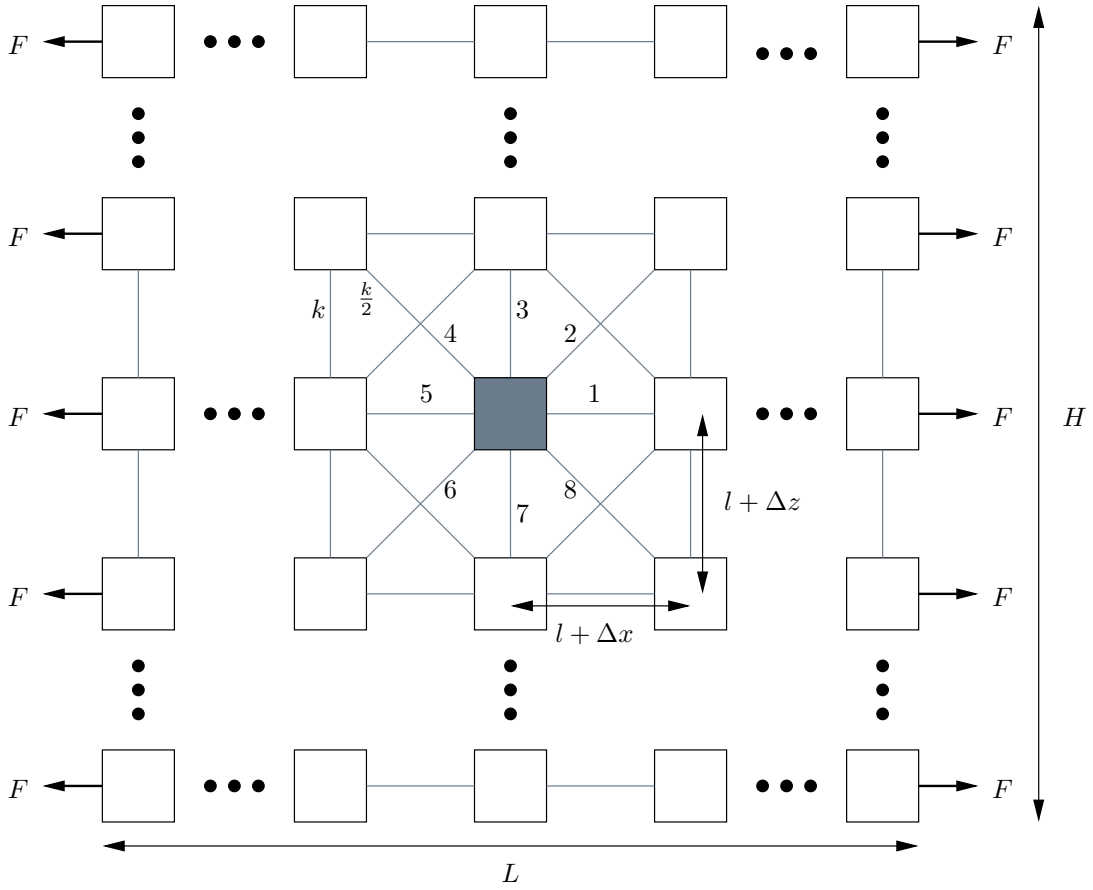

Figure 5.2: By calculating the forces on the shaded block one can find the relationships between the spring constant k and Young's modulus E and Poisson's ratio ν. Springs are shown as grey lines.

because it has a tensile failure surface, with which I will not be concerned, that is more isotropic. Since I will not include bond bending forces selecting one over the other is, to my knowledge, a matter of taste. I have chosen the square lattice. Setting the bond bending constant $c = 0$ and adjusting for the fact that I have defined $k = k_1$ while Monette and Anderson define $k = k_2$ their equation (3.12) becomes

$$E = \frac{4}{3}k, \tag{5.2a}$$

$$\nu = \frac{1}{3}. \tag{5.2b}$$

The first of these suppresses some factor of dimension length, as $[E] =$ Pa while $[k] =$ N/m. To find this factor, and to investigate the importance of boundary effects, I will now derive these relationships.

Figure 5.2 shows the system in equilibrium under uniform tension in the x-direction. This configuration is suitable for determining $E(k)$ and $\nu(k)$. The number of blocks N_x and N_z in the x- and z-directions, respectively, is large so that boundary effects can be neglected. The third dimension of the system (not shown) is B, the area on which the

total force $\tilde{F} = \sum F = N_z F$ acts is $A = BH$. By definition of the elastic constants,

$$E = \frac{\tilde{F}/A}{\Delta\tilde{x}/L} = \frac{\tilde{F}L}{\Delta\tilde{x}A}, \tag{5.3a}$$

$$\nu = -\frac{\Delta\tilde{z}/H}{\Delta\tilde{x}/L} = -\frac{\Delta\tilde{z}}{\Delta\tilde{x}}\frac{L}{H}, \tag{5.3b}$$

where

$$\Delta\tilde{x} = N_x \Delta x, \tag{5.4a}$$

$$\Delta\tilde{z} = N_z \Delta z, \tag{5.4b}$$

$$\frac{N_x}{N_z} = \frac{L}{H}. \tag{5.4c}$$

This can be rewritten as

$$E = \frac{F}{\Delta x B}, \tag{5.5a}$$

$$\nu = -\frac{\Delta z}{\Delta x}. \tag{5.5b}$$

The tension across any vertical cross-section is the same and equal to $\tilde{F}$. When boundary effects can be neglected this means that the sum of the x-components of the forces in springs 1, 2 and 8 in Figure 5.2 must equal F:

$$\begin{aligned} F &= F_{1,x} + F_{2,x} + F_{8,x} \\ &= k\Delta x + 2\frac{k}{2}\left(r - \sqrt{2}l\right)\frac{l + \Delta x}{r}, \qquad r = \sqrt{(l+\Delta x)^2 + (l+\Delta z)^2}. \end{aligned} \tag{5.6}$$

Similarly, the tension across any horizontal cross-section is zero, so that

$$\begin{aligned} 0 &= F_{2,z} + F_{3,z} + F_{4,z} \\ &= k\Delta z + 2\frac{k}{2}\left(r - \sqrt{2}l\right)\frac{l + \Delta z}{r}. \end{aligned} \tag{5.7}$$

In order to use equations (5.5) I need linearised expressions $F(\Delta x)$ and $\Delta z(\Delta x)$. To obtain these, expand r at $\Delta x = \Delta z = 0$:

$$r(\Delta x, \Delta z) = \sqrt{2}l + \frac{1}{\sqrt{2}}(\Delta x + \Delta z) + O(\Delta^2), \tag{5.8a}$$

$$\frac{1}{r} = \frac{1}{\sqrt{2}l} - \frac{1}{2\sqrt{2}l^2}(\Delta x + \Delta z) + O(\Delta^2). \tag{5.8b}$$

Inserting this in equation (5.7) and keeping terms to first order gives

$$\Delta z = -\frac{1}{3}\Delta x. \tag{5.9}$$

Using this and equations (5.8) in equation (5.6) and keeping terms to first order gives

$$F = \frac{4}{3}k\Delta x. \tag{5.10}$$

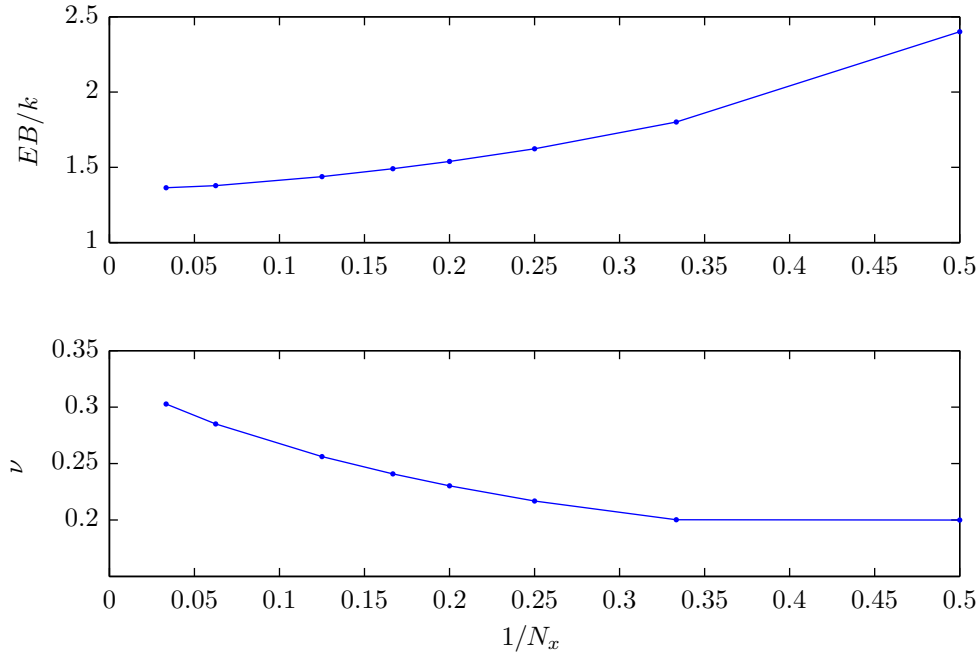

Figure 5.3: Young's modulus E and Poisson's ratio ν for a two-dimensional system. For a given value of k, E and ν depend on the relative importance of the bulk and the boundary, with the limiting cases given by equations (5.11) and (5.12). The data shown was found by implementing the experiment in Figure 5.2 and measuring the deformations after equilibration. $H = L$, which implies $N_x = N_z$. The perfect agreement with equation (5.12) provides a verification of the implementation.

With these results for $F(\Delta x)$ and $\Delta z(\Delta x)$ equations (5.5) become

$$\boxed{E = \frac{4}{3}\frac{k}{B},} \tag{5.11a}$$

$$\boxed{\nu = \frac{1}{3},} \tag{5.11b}$$

in agreement with the results of Monette and Anderson (equations (5.2)). Note that without bond bending forces ν is not adjustable; luckily, $\nu = 0.33$ is the value listed for PMMA in the supporting online material of [7], which I follow.

Carrying out a similar analysis for the case $N_x = N_z = 2$ maximises boundary effects. One obtains

$$E = \frac{12}{5}\frac{k}{B}, \tag{5.12a}$$

$$\nu = \frac{1}{5}, \tag{5.12b}$$

which shows that significant deviations from the $N_x, N_z \gg 1$ case are possible. Figure 5.3 shows E and ν for increasing N, determined by computer simulations.

5.2.2 Damping

Slip events at the interface or abrupt changes in loading conditions (e.g. at the start of simulations) will introduce oscillations in the system. If they are allowed to persist they

may eventually come to dominate the dynamics, which is undesirable. Friction occurs only at the interface and does not damp oscillations sufficiently on its own. In fact, while the interface is pinned there is no frictional damping at all. I have introduced what might be coined *solid viscosity*: a damping resisting relative motion of the nodes. Contrast this with absolute viscosity, which resists motion with respect to some external medium.

Solid viscosity in 1D was introduced in Section 4.1.2. Since the motion of the blocks is then always along the direction of the springs, I did not distinguish a change of spring length from a relative motion of the blocks; the two are one and the same. Not so in 1+1D.

If the damping is considered to be a property of the springs, a natural way to define the force on block i from neighbouring block j is

$$F_{ij} = \eta \frac{\mathrm{d}r_{ij}}{\mathrm{d}t}, \tag{5.13}$$

where F_{ij} is the magnitude of the force and r_{ij} is the length of the vector pointing from the position of i to the position of j. As can be shown by writing out the components,

$$\frac{\mathrm{d}r_{ij}}{\mathrm{d}t} = \mathbf{v}_{ij} \cdot \hat{\mathbf{r}}_{ij}. \tag{5.14}$$

The component along the x-direction would be

$$F_{ij,x} = F_{ij} \frac{\Delta x_{ij}}{r_{ij}}, \tag{5.15}$$

with a similar expression for the second dimension.

One may also consider the springs and the damping to be independent. I have taken such a view. The springs are a particular way of modelling linear elasticity, leaving the question of how to dampen oscillations open. Then, damping on the form

$$\boxed{\mathbf{F}_{ij} = \eta(\mathbf{v}_j - \mathbf{v}_i)} \tag{5.16}$$

becomes an obvious choice. I have preferred this form because it gives a more efficient damping: where equation (5.15) only acts on the motion of the blocks to and from each other, equation (5.16) dampens all relative motions.

While the damping coefficient η should be high enough to ensure that oscillations die out between successive events, ideally it should not affect the dynamics during the events, since it is not expected to imitate the physical damping process(es). In particular, overdamping of any mode is undesirable, as this can, for instance, prevent a sliding event from stopping as nodes approach their equilibrium positions without ever reaching them.

The damping regimes of the one-dimensional monatomic chain are calculated in Appendix B.3. I have not been able to perform a similar analysis for the 1+1D system. Instead, I have investigated the damping numerically. An obvious disadvantage of this is that whereas equation (B.31) gives the critical damping coefficient for any mode of oscillations, each numerical experiment only covers a specific excitation. To cope with this I have studied excitations that I believe are particularly relevant for the later work, viz. a single block at the slider–track interface sliding under dynamic friction while its neighbours are pinned.

An overdamped oscillation by definition does not overshoot the point of zero net force, it approaches this point as a decaying exponential function (or a sum thereof).

An underdamped motion will overshoot the dynamic friction level, and then the block will reach a point of zero velocity at which static friction will keep it pinned. It is tempting to consider the complete stopping of the motion to be the *signature* of underdamping; overdamped motion is then identified as motion that does not cease. In numerical studies, however, this is not a robust criterion, because unceasing motion requires negligible velocities to remain positive at all times. Round-off errors are always present, and testing that something arbitrarily small does not oscillate around zero is sensitive to these errors.

A point excitation in the 1D model can be solved analytically. An arbitrary node i is displaced to left so that the spring forces on it from the neighbours just exceed the static friction threshold. As long as the neighbours remain pinned, which they will unless additional excitations are introduced, this is the same as a single block attached by springs to two rigid walls. The two springs act in series and there is damping due to the relative motion with respect to both neighbours. Equation (B.18) applies if $\eta \to 2\eta$ and $k \to 2k$, so that critical damping occurs when $\eta = \sqrt{2km}$.

Having obtained the analytical result, I looked at barely underdamped and overdamped systems. For this configuration the naive test outlined above did work: from simulations I found that the displaced node stopped moving for $\eta = (\sqrt{2} - 0.01)\sqrt{km}$, while for $\eta = (\sqrt{2} + 0.01)\sqrt{km}$ it did not stop moving. Figure 5.4 shows the time evolution of the position, velocity and forces on the node in the latter case.

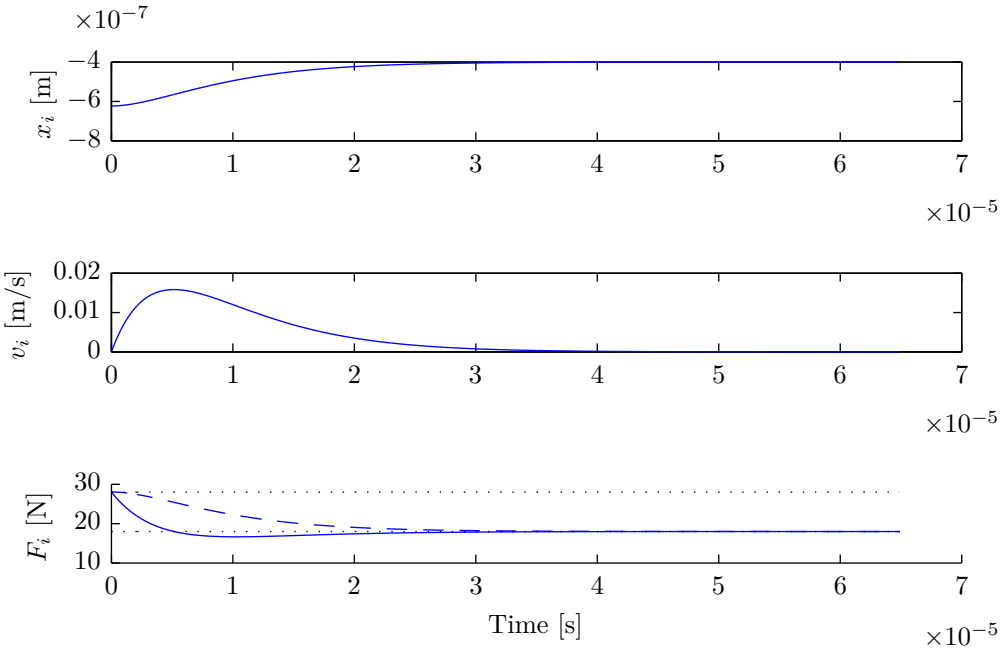

Figure 5.4: Overdamped motion in the 1D model. A single node i was displaced to left just enough to exceed the static friction level. In the bottom figure, the blue dashed line is the total elastic force, the blue drawn line is the elastic force plus the total damping force, and the black dotted lines are the static and dynamic friction levels. Note that close to the critical damping value, this kind of figure cannot be used to distinguish overdamping from underdamping. Rather, a boolean variable (not shown) with values sliding / not sliding was inspected to determine whether the block stopped moving or not. $N = 10$, $\eta = (\sqrt{2} + 0.01)\sqrt{km}$, remaining parameters as in Table 4.1.

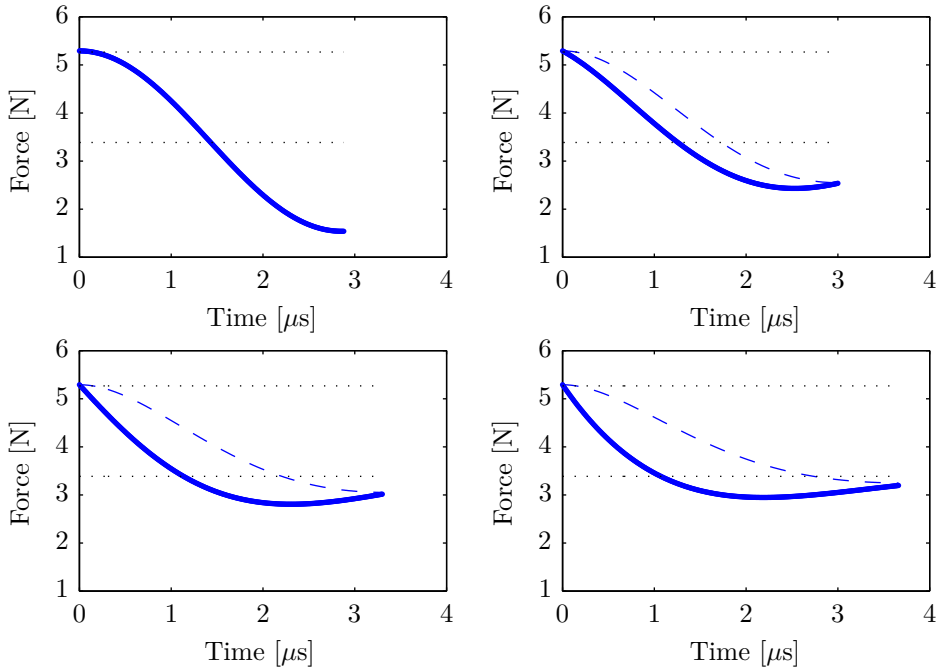

Figure 5.5: Underdamped motion in the 1+1D model. The blue dashed line is the net elastic force on the block in motion, the blue drawn line is the net force including damping forces, the black dotted lines are the static friction threshold and the dynamic friction level. The final point in time in each plot is the instant at which the block stopped. From top left and in reading order, $\eta/\sqrt{km}$ equals 0, 0.15, 0.3 and 0.4, respectively. $\theta = 0$, $N_z = 11$, $k_{\mathrm{ps}} = k$, $\Delta t = 10^{-8}$ s, remaining parameters as I in Table 5.1. Top loading: pressure. The parameters and loading conditions are described in Sections 5.3 and 5.5.

A more robust test that works well in the 1+1D model is to use directly the observation that in underdamped motion, the net force overshoots zero and reaches negative values, whereas in overdamped motion, this does not happen. The following scheme puts a lower bound on the critical damping coefficient. Initially, set $\eta = 0$ and observe that the overshooting is approximately symmetric: when the motion stops, the net force on the block has its initial magnitude, but the opposite sign. Increase η and repeat the experiment. If the system is underdamped, the final magnitude of the net force will be less, but the sign will still have changed. Repeat for increasing η. Once the final magnitude of the net force is reduced to one tenth, say, the system is close to critical damping. This precision is sufficient if the only objective of the analysis is to identify the maximum η that can be used while still ensuring underdamping.

Figure 5.5 illustrates my application of this test. As η is increased the overshooting of the dynamic friction level (at which the net force on the block is zero if dynamic friction is acting) is reduced. Also, the duration of the event, identified by the last data point in each panel, increases. The figure shows that $\eta/\sqrt{km} = \sqrt{0.1} \approx 0.32$ will give underdamping that is efficient without being too close to critical damping, and so I have used this value of η.

5.3 Simple boundary conditions

In 3D the slider has six boundaries. The one under study is the lower face, where the slider rests on the track. This is the frictional interface. However, as was seen in Chapter 4, all of the boundary conditions are important for the evolution of the system.

In addition to friction, there are normal forces acting on the lower face of the slider. If the system is side pushed, the driving force acts on the left face (trailing edge). Otherwise, this face is a free boundary. The external normal load is applied on the upper face. The right face (leading edge) is free, and so are the front and back faces, which are not included in the model.

In 1D the boundary conditions were simplified by the geometry of the model. The lower and upper faces are the same, and so the normal force distribution at the sliding interface was by necessity imposed directly. The left and right boundaries each consisted of a single node.

One of the strengths of the 1+1D model is the possibilities it gives to mimic the experimental boundary conditions; I return to this in Section 5.8. To get started, however, I implemented a set of simple boundary conditions.

5.3.1 The bottom surface

The normal force distribution at the bottom surface, crucial to the frictional response, is determined by the forces from above layers. In equilibrium, the total external normal force W on the bottom surface equals the external load F_Z on the top surface. Two simple ways of imposing a force response are a potential surface and an impregnable barrier.

An impregnable barrier explicitly prohibits the system from entering the lower half-plane. The external normal force on each bottom node is exactly equal and opposite to the sum of the internal vertical forces on the node, as long as these act downwards. To get a complete description, one must decide whether to prohibit lifting of the bottom nodes off the barrier: if the internal vertical forces on a node are positive, upwards movement may or may not be prevented by the barrier. If upwards movement is allowed, care must be taken to ensure that if the node comes back down, it does not penetrate the barrier because of algorithmic mistakes. Analytically, the impregnable barrier is the infinite stiffness limit of a potential barrier; numerically it should not be treated in this way because of finite precision arithmetic. A very high stiffness can lead to instability as round-off errors are amplified.

The force from a potential barrier can take any number of functional forms. I have chosen a linear potential of stiffness k_{ps}, giving an upwards force on bottom node i

$$w_i^{\mathrm{bottom}} = \begin{cases} -k_{\mathrm{ps}} z_i, & z_i < 0, \\ 0 & z_i \geq 0. \end{cases} \tag{5.17}$$

The stiffness k_{ps} of the barrier should be compared to the internal stiffness k of the spring-block system. If the barrier is very soft compared to the system, the force on each bottom node will be approximately the same. This is because the potential is linear, so that it takes twice the penetration to get twice the force. If this length, which also depends on the loading force, is on the order of the equilibrium length l of the springs, such deformation of the interface is unlikely. What will happen instead is that the whole system will move into the barrier more or less uniformly, giving the same normal force on all bottom nodes. Of course, with a soft barrier, the amount of penetration can be

higher than l, and you have to consider whether the boundary condition acts on all nodes or on the ones that are initially at the interface only.

For $k_{\mathrm{ps}} \gg k$, the potential barrier is nearly the same as a rigid support / impregnable barrier. In this range, the penetration into the barrier will be negligible, and all results should be independent of k_{ps}. I have used $k_{\mathrm{ps}} = k$ and $k_{\mathrm{ps}} = 10k$. They give the same results, which I interpret as k_{ps} independence.

The main advantage of using a potential force over a rigid support is ease of implementation. The force from the potential can simply be added to the net force on each bottom node, i.e. treated like any other force. A rigid support has to be implemented as a constraint on the available positions of the bottom nodes, and this requires additional `if`-tests.

The shear forces from the bottom surface are given by the chosen friction law. As in 1D I have used Amontons–Coulomb friction with a static coefficient μ_s and a dynamic coefficient μ_k. In Chapter 6 I test the robustness of my results by using a slip weakening friction law.

5.3.2 The top surface

The normal force at the bottom surface balances the other vertical forces acting on the system, which in the friction experiments I try to model is simply an imposed normal force at the slider's top surface. Gravitational pull is neglected.

The simplest way to impose the normal force on top is node-wise, i.e. as a vertical force acting on each top block. This condition allows the top surface to deform, and it does not resist a tilting of the system. It is similar to an external pressure in that deformation of the surface does not lead to a change in force distribution, which is what one would typically expect if the top surface was attached to a solid object. I have therefore referred to a vertical force acting on each top block as a pressure condition. The pressure does not have to be the same at all points along the top surface, but can e.g. be given by an expression similar to equation (4.8), which is what I use when θ is given in the list of parameters.

A change in force distribution with deformation of the surface, which will occur at the corners of the system, can e.g. be achieved by letting the topmost blocks interact with a potential surface. The system deforms most easily near the corners, and therefore the blocks near corners will not penetrate the potential surface as deeply as blocks closer to the middle, thus taking up a smaller amount of the imposed normal force. The potential surface may or may not be allowed to translate and rotate. If movement of the surface is allowed, it can be assigned a mass and/or a moment of inertia and treated as a system of its own under the influence of some external force(s) and the reaction forces from the blocks. If the potential surface is not allowed to move, the normal force will depend on the distance between the top and bottom boundaries, and it can be harder to control the magnitude of the imposed force. Whether or not the potential surface moves, this boundary condition imposes no restrictions on the horizontal movement of the top nodes.

If the slider is glued to some much stiffer medium, it may be more appropriate to restrict the horizontal movement. This can for instance be achieved by keeping the positions of the blocks relative to some rigid rod fixed, or by attaching them to the rod through springs. In Section 5.8 I present the details of a boundary condition like this, which is the most similar to the experiments by the group of Jay Fineberg.

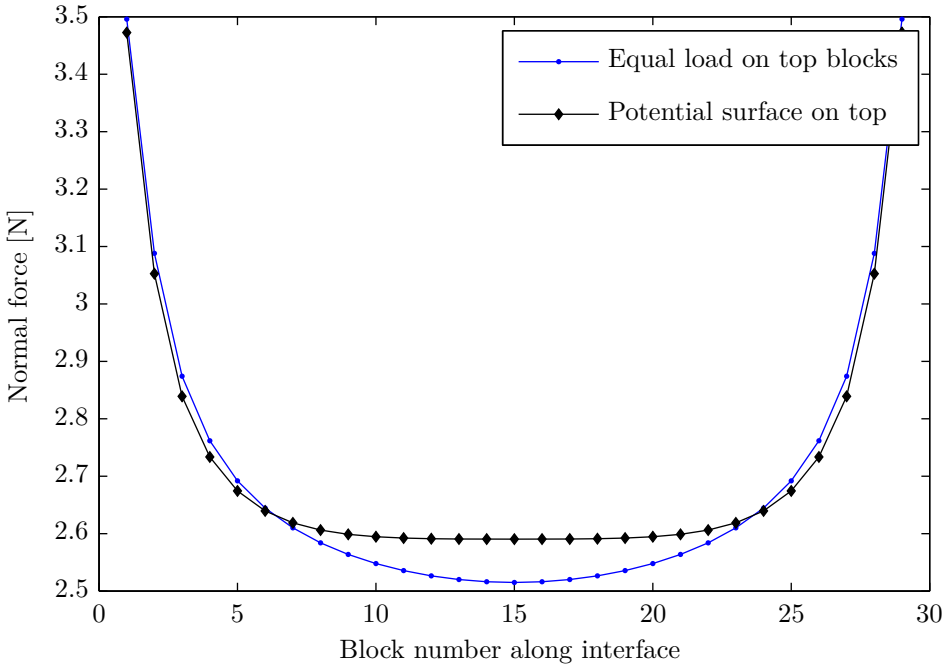

Figure 5.6: Equilibrium of normal force distribution at slider–track interface, where the slider rests on a potential surface. Two different loading conditions on the top of the slider are shown: equal load on all top blocks (pressure) and a potential surface on top. The total normal force is $F_Z = 80$ N. There is no driving. The potential surfaces have the stiffness $k_{\mathrm{ps}} = k$.

Figure 5.6 shows the normal force distribution at the bottom surface for the node-wise and potential surface conditions on the top.

5.3.3 The trailing and leading edges

Driving the system from the side can be done in one point, at all points, or anything in between. To allow the system to compress under the influence of the normal forces at the top and bottom, no vertical forces or constraints have been imposed at the trailing edge.

I have applied driving at a single node, of the same form as in the 1D model. A spring of stiffness K is coupled to the node at height h and to a point moving with a constant speed V to the right. The driving force is similar to equation (4.4),

$$F_X = K\left(Vt - x_h\right), \tag{5.18}$$

x_h being the horizontal position of the node at height h. The force is strictly horizontal. I have typically used a vertical resolution of ~ 30 nodes; if a much higher resolution is used, F_X should be applied over a region of physical extent rather than at a single node.

The leading edge has been treated as free, i.e. no external forces have been imposed.

5.4 Numerical preparations

5.4.1 Code structure

A flexible way to represent the grid of blocks and interconnecting springs in the computer is to create a one-dimensional array of block objects. Each block object stores certain internal properties like its position, velocity and mass, some of which may be equal for some or all blocks. Additionally, each block object has a list of the blocks it is connected to, and the properties of the springs that make up these connections. Since each connection involves a pair of blocks and should not be counted twice, the blocks need only store the connections to blocks of higher index in the block array. This also makes for efficient force calculations. Finally, the blocks store information of their location in the global system. This is important since the external forces like friction and applied normal and shear forces do not necessarily act on all blocks.

5.4.2 Time step length

As in 1D the equations of motion will be solved by a fourth order Runge Kutta method on a uniform temporal grid. Like in 1D I hold that the time step length Δt should be small enough that the motion of each block is well resolved, but does not have to be much smaller than this. Again, a relevant time scale is $T = 2\pi\sqrt{\frac{m}{k}}$. The effective stiffness of the springs connected to each block is of course different from k, but only by a numerical factor of order 1. I have typically used $\Delta t \leq T/50$. Retrospective inspection of block's movements shows that this is sufficient to resolve each motion into many steps in time.

5.4.3 Initialisation

As in the 1D models, the initial conditions must be given in order to have a complete description of the system. Because of the nonlinear nature of friction, the initial conditions in the experiments depend on how the slider was mounted. An obvious example is that for $F_Z > 0$, $F_X = 0$, it matters whether F_X has not yet been applied or the slider has been sliding and F_X was then reduced to zero. I will stick to the former case. The slider is put down with no forces acting on it, and then F_Z is applied.

When setting up the computational lattice, it is convenient to use a uniform grid with no deformations, corresponding to no external forces. When $F_Z > 0$ is applied, the slider will be compressed in the normal loading direction, and, as discussed in Section 2.2, expand laterally. In my simulations, I have let the system relax to the equilibrium configuration for the desired value of F_Z before F_X was applied. A straightforward way to implement this relaxation is to use the same forward in time integration as I use to study the behaviour under shear loading. However, as long as no slip occurs at the interface, the initial relaxation is an equilibrium problem that can be solved much more efficiently.

To verify that no slip occurs at the interface during the initial relaxation, while still making use of the efficiency of equilibrium solution, I have used a *successive relaxation* scheme. Equilibrium is reached by taking steps that resemble the physical path that the system would follow if time integration was applied. The speedup is obtained because inertia is ignored, preventing overshooting and long-lived oscillations, and by taking larger steps than time integration allows. I will here briefly outline the relaxation scheme.

By definition, in equilibrium the net force on each node is zero. In each relaxation step the system moves towards this state. Each node is moved according to the net force on it: if the net force is small, the movement is small; if the force is bigger, the movement is bigger. To quantify, consider a single block in 1D attached to a spring of stiffness K. If the net force is F, equilibrium is reached by taking a single relaxation step of length $\Delta x = F/K$. If there are more blocks, an effective stiffness K_{eff} can be found for the springs acting on each one. Global equilibrium is not reached in a single step, however, because the movement of each block affects the net force on its neighbours after the step.

Typically, a relaxation parameter ω_{rel} is introduced, and $\Delta x_i = \omega_{\text{rel}} F_i / K_{\text{eff},i}$ for each node i. Convergence requires $\omega_{\text{rel}} \in (0, 2)$. Using $\omega_{\text{rel}} > 1$ is often efficient, and the scheme is then called successive over-relaxation (SOR).

In 1+1D, successive relaxation can be applied in the x and z-directions independently. The effective stiffness in each direction can be found by linearised analytical calculations. Forces that do not arise from springs, like the normal loading forces on the top boundary, can also be treated properly, but I have chosen a simplified implementation by treating these forces in the same way as the spring forces, putting their K equal to zero. This gives K_{eff} that are too small, and the maximum ω_{rel} that gives convergence is reduced. By trial and error I've found that $\omega_{\text{rel}} = 0.1$ works well. A more thorough analysis would no doubt give a better value for ω_{rel} and faster initialisation; however, the initialisation time is short compared to the total simulation time and so there is little to gain from such analysis.

5.4.4 Verification

Verification of the RK4 implementation, the damping and the time step length is provided by the $N_x = N_z = 2$ results of Figure 5.3, in which the experiment of Figure 5.2 was implemented as a fully time dynamic relaxation.

5.5 Parameters

To obtain good agreement with experimental results, the parameters in the model are based on their experimental counterparts. Parameters corresponding to the experiment of Maegawa et al. [36] are given as I in Table 5.1. Note that I have changed the value of V from 0.1 mm/s, this is explained in Section 5.5.2. The extent of the pushing apparatus on the trailing edge is not clear from [36], and although it appears from their quite detailed figure to have a size comparable to H, I have applied F_X at a single point at the height $h/H = 1/10$ for convenience, as this is similar to the other set of experiments that I model.

Most of my work with the 1+1D model has been aimed at the experiments conducted by the group of Jay Fineberg at the Hebrew University of Jerusalem. The details of the experiments are found in [45] and [46].

The dimensions of the slider and track are $140(200) \times 6 \times 75$ mm and $300 \times 30 \times 27$ mm in the (x, y, z) directions of external shear, sample thickness and normal loading. Two sliders of different length was used, hence the 140(200) notation. The normal loading on top was applied to the slider via an array of 40 springs of total stiffness $4 \cdot 10^5$ N/m sandwiched between two rigid plates. In Section 5.8 I explain how I model this loading condition. Total normal force was varied between experiments, and was on the order of

			I	II	III	
Macroscopic	Slider	L	100	140	200	mm
		H	20	75	75	mm
		B	5	6	6	mm
		E	2.5	3	3	GPa
		ν	1/3	1/3	1/3	
		M	0.012	0.076	0.108	kg
	Loading	F_Z	0.40	3.5	2.7	kN
		K	0.8	4	4	MN/m
		V	$\frac{2\mu_k F_Z}{K \times 1\ \mathrm{s}}$	”	”	
		K_{mat}	n/a	0.4	0.4	MN/m
		M_{mat}	n/a	M	M	
		h	$H/10$	$H/15$	$H/15$	
		θ		n/a	n/a	
Microscopic		μ_s	0.7	0.7	0.7	
		μ_k	0.45	0.45	0.45	
Numerical		N_x		$L(N_z-1)/H+1$		
		N_z				
		m		$M/(N_x N_z)$		
		k		$3EB/4$		
		k_{ps}		$10k$		
		Δt				
		η		$\sqrt{0.1}\sqrt{km}$		

Table 5.1: Typical parameters used in the 1+1D model. An empty field means that the variable in question does not have a single, most common value. An ending quotation mark (”) means that the value equals the previous column, while n/a means *not applicable*. The microscopic and numerical parameters are shared between all parameter sets. I corresponds to the experiment of Maegawa et al. [36] while II and III correspond to the experiments by the group of Jay Fineberg.

kilonewtons. The shear force was applied by coupling to a stepping motor via a load cell of stiffness $4 \cdot 10^6$ N/m. The motor moved in discrete steps of 0.04 μm with loading rates ranging from 1 μm/s to 10 mm/s. The load cell coupled to a rod of diameter 12 mm and was applied at 6 mm above the interface except when varied to study effects of the loading height explicitly. In the supporting online material of [7], Young's modulus and Poisson's ratio for PMMA are given as $\nu = 0.33$, $E \approx 3$ GPa. My most common parameters are II and III in Table 5.1.

5.5.1 Determining μ_s and μ_k from experimental data

Macroscopic experimental parameters like the mass, geometric shape, elastic moduli and the magnitude of the external forces are straightforward to select: they are chosen equal to their experimental values. To some extent the friction coefficients also have experimental counterparts. Although the simple Amontons–Coulomb laws are far from a complete description of the response at the sliding interface, globally one commonly predicts a global static friction threshold, and in steady sliding a dynamic friction level. I've found that in order to reproduce the static friction threshold found in an experiment, the static friction in the model should be assigned a different value than the experimental one. I will use the term *local* static friction to refer to μ_s, the static friction coefficient

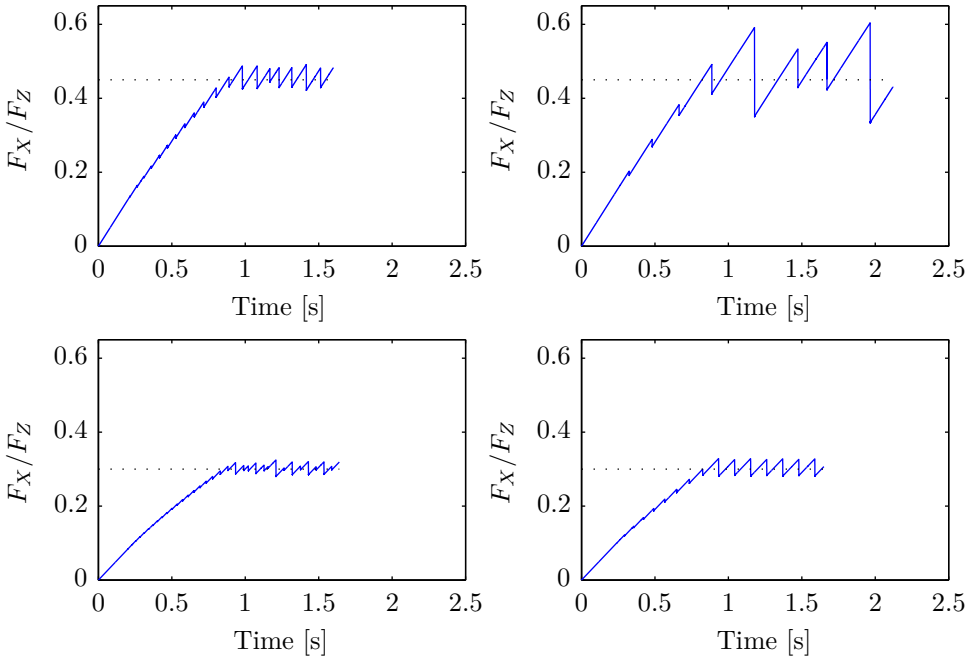

Figure 5.7: Influence of the local friction coefficients. The blue drawn line is $F_X(t)$, the horizontal black dotted line is μ_k. Top left: $\mu_k = 0.45$, $\mu_s = 0.7$; top right: $\mu_k = 0.45$, $\mu_s = 1.2$; bottom left: $\mu_k = 0.3$, $\mu_s = 0.4$; bottom right: $\mu_k = 0.3$, $\mu_s = 0.5$. Observe that the global dynamic friction level is close to μ_k, while the global static friction level is much less than μ_s (not shown). $h = 5$ mm, $N_z = 31$, $k_{\text{ps}} = k$, $\Delta t = 2 \cdot 10^{-7}$ s, remaining parameters as II in Table 5.1. Top loading: pressure.

of a single block in the model. *Global*, or macroscopic, static friction is the resulting system property that can be compared with experiments. In this terminology, the above can be rephrased as $\mu_s^{\text{global}} < \mu_s$. For the dynamic friction coefficients the differences are smaller, i.e. the global dynamic friction is close to the local dynamic friction. In this section I will discuss how the local quantities μ_s and μ_k can be determined from the global quantities.

Figure 5.7 shows the typical time evolution of the force $F_X(t)$ from the driving stage. One way of determining μ_k and μ_s is to make figures like this with different values of the friction coefficients and compare them to experimental results. In doing so, some understanding of how the figure changes with the friction coefficients is needed. An important observation is that during the stick–slip phase, the time average of F_X/F_Z is close to μ_k, while the maximum value taken is less than μ_s, which is easily shown. Considering the forces immediately before an event and neglecting the vibrations of the bulk material,

$$F_X = \sum_i f_i \leq \sum_i \mu_s w_i = \mu_s F_Z, \tag{5.19}$$

where the sum is over all blocks at the slider–track interface. The highest value taken by F_X/F_Z, i.e. the global static friction coefficient μ_s^{global}, increases with μ_s. It also increases with h/H, which becomes clearer in Section 5.7.

An analytical solution of the motion of a single block is useful in explaining why the local maxima and minima in the stick–slip phase are (nearly) symmetric around μ_k.

Consider the system in Figure 2.2 and assume that V is small so that during an event, the change in the position X of the driving point can be neglected. If x_0 is the position of the block at sliding initiation and Δx is the total slip during the following event, the elastic energy in the spring is

$$E_0 = \frac{1}{2}K(X - x_0)^2 \tag{5.20}$$

before the event and

$$E_1 = \frac{1}{2}K((X - x_0) - \Delta x)^2 \tag{5.21}$$

after the event. The change in stored elastic energy is

$$\begin{aligned} \Delta E &= E_1 - E_0 && (5.22)\\ &= \frac{1}{2}K(-2(X - x_0)\Delta x + \Delta x^2) && (5.23)\\ &= \Delta x\left(-K(X - x_0) + K\frac{\Delta x}{2}\right). && (5.24) \end{aligned}$$

This is balanced by the work done by friction, which is $-\mu_k w \Delta x$. Using $K(X - x_0) = F_{\text{trigger}}$ and equating the work and the change in potential energy,

$$\Delta x = \begin{cases} 0 \\ 2\frac{F_{\text{trigger}} - \mu_k w}{K}, \end{cases} \tag{5.25}$$

where the solution $\Delta x = 0$ is unphysical. The force from the driving stage at sliding arrest is

$$\begin{aligned} F_{\text{stop}} &= K((X - x_0) - \Delta x) && (5.26)\\ &= F_{\text{trigger}} - 2(F_{\text{trigger}} - \mu_k w) && (5.27)\\ &= \mu_k w - (F_{\text{trigger}} - \mu_k w), && (5.28) \end{aligned}$$

which shows that in this simple case, the overshoot exactly balances the difference between the triggering force and the dynamic friction level.

For the 1D and 1+1D models, the calculation is changed in the following ways: there is additional work done by the internal damping forces, and there is internal elastic energy. The former makes the overshoot smaller, while the latter can go both ways, depending on the relative internal energy of the initial and final configurations. On average, the overshoot will be less, and so the average of F_X/F_Z will be greater than μ_k. The greater the difference $\mu_s - \mu_k$ becomes, the more important internal damping will be, and the difference between the average of F_X/F_Z and μ_k will increase, as Figure 5.7 indeed shows.

Another indicator of the values of μ_k and μ_s that fit a given experiment is the number of precursor events. This will be discussed in Section 5.7. Initially I kept $\mu_k = 0.45$, $\mu_s = 0.7$ as in the 1D model. From the above considerations and the results to come, I hold that these are reasonable values for the experiments I model.

5.5.2 The driving speed

The driving speed V and the stiffness K of the driving stage determine the rate KV of increase of the driving force between events. Because of separation of time scales in

the slow driving limit, the computation time is inversely proportional to this rate: most of the time is spent between events, and the lower the value KV, the longer the time between events. Unlike in the 1D model this time cannot be easily skipped, because there are waves propagating and dying out in the bulk long after the sliding at the interface arrests, and because the bulk deforms in a non-trivial manner during the increase in F_X.

I have used a higher value of KV than what was used in the experiments, to reduce the simulation time. Changing K would change the ratio of the external and internal stiffness, which I do not want, and so I have increased V instead. One should ensure that there is still a separation of time scales, and that sufficient time elapses between events that the induced oscillations die out. Of these, the latter turns out to be the stricter requirement. I discuss it in Section 5.9.1. The driving speed I use is

$$V = \frac{2\mu_k F_Z}{K \times 1\ \mathrm{s}}. \tag{5.29}$$

This way I know that the first global sliding event occurs at $t \approx 1$ s, which is very useful when setting the total time to simulate in each run, even if the approximation is rather poor.

5.6 Loading curve and number of sliding blocks

Figure 5.8 shows the loading curve and the number of sliding blocks at the slider–track interface. It should be compared to Figures 3.3b and 4.14b, its experimental and 1D counterparts. As in the experiment, the global trend is a quasi-linear increase up to a stick–slip regime. Preceding the global sliding events is a series of precursors of increasing length, each associated with a drop in F_X. The agreement with experiment is not perfect, however. The simulation shows chaotic stick–slip of magnitude $F_Z/10$, and while this magnitude is the same in the experiment, the stick–slip pattern in Figure 3.3b is regular. The driving velocity was $V = 0.45$ mm/s compared to $V = 0.1$ mm/s in experiments and 1D, which explains perfectly the differences in the values of t at which global sliding occurs. In fact, the whole time axis is rescaled by the change in V, or more precisely the change in KV, the rate of increase of the driving force.

One of the shortcomings of the side driven 1D model was that the loading curve and the number of events depended linearly on the resolution N. The resolution dependence of the 1D model stemmed from the $1/N$ scaling of the force increase $\Delta F_X^{\text{next event}}$ required to trigger successive events. The loading zone was the leftmost node only. In the 1+1D model the extent of the loading zone has a *physical length scale*: it is on the order h or $2h$, illustrated in Figure 5.9. For this reason, the force increase required to trigger successive events is resolution independent. This removes the strong resolution dependence, as Figure 5.10 confirms. Complete resolution independence is not obtained, but this is not to be expected at these low resolutions: for $N_z = 16$, the driven node at $h/H = 1/15$ is only one layer above the interface, and the coarseness of the grid is likely to be important.

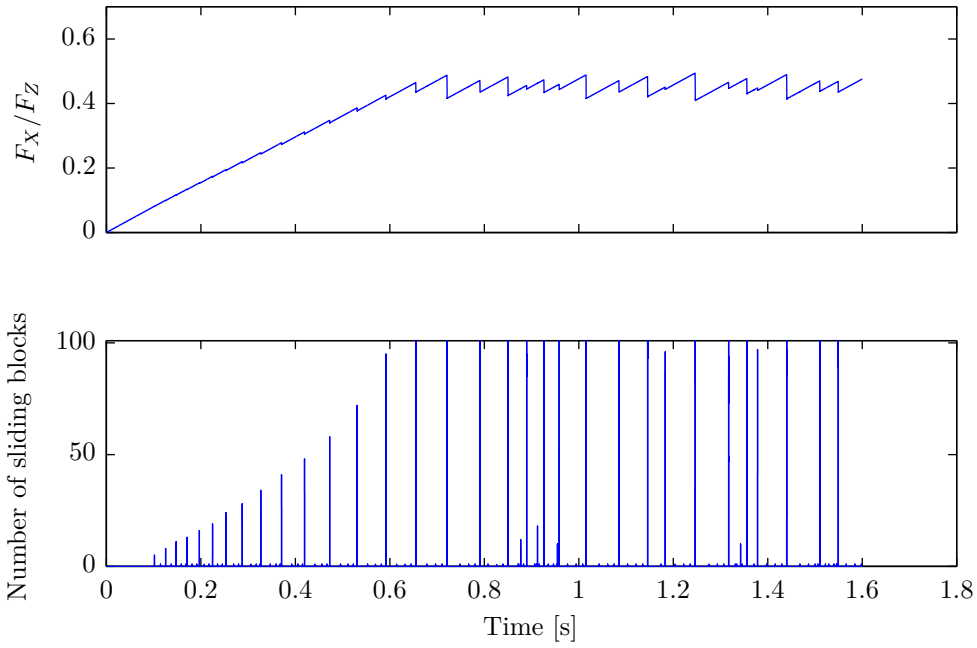

Figure 5.8: The loading curve and the number of sliding blocks in the 1+1D model. $N_x = 101$, $N_z = 21$, $\theta = 0$, $\Delta t = 9 \cdot 10^{-8}$ s, $k_{\text{ps}} = k$, remaining parameters as I in Table 5.1. Top loading: pressure.

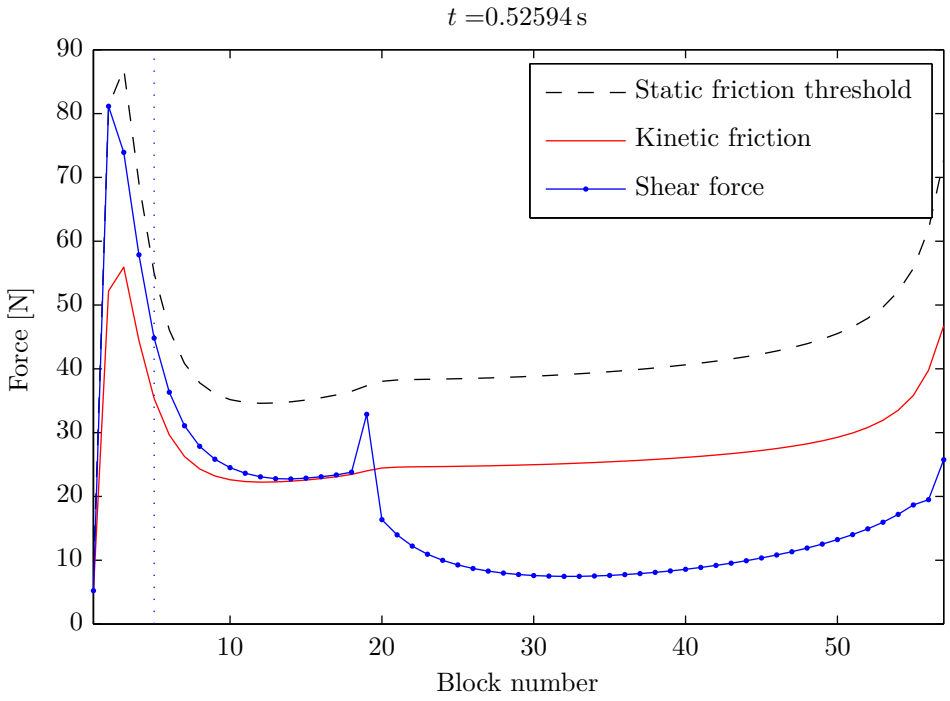

Figure 5.9: I define the *loading zone* as the region in which the shear and normal forces are significantly altered during the loading between events, i.e. the region to the left of the dashed line, which is located at $2h$. The edge of the loading zone is not uniquely defined, and the numerical factor in front of h is somewhat arbitrary. $N_x = 57$, $N_z = 31$, $\Delta \text{t} = 2 \cdot 10^{-7}$ s, $k_{\text{ps}} = k$, $h = 5$ mm, remaining parameters as II in Table 5.1. Top loading: pressure.

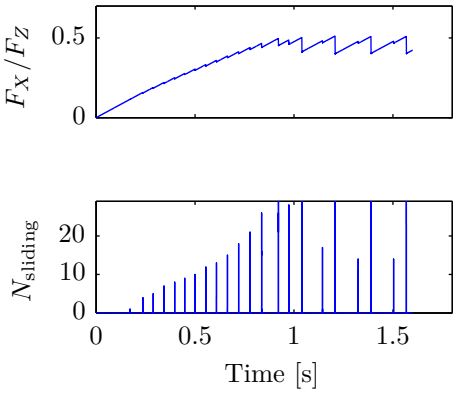

(a) $N_x = 29$, $N_z = 16$.

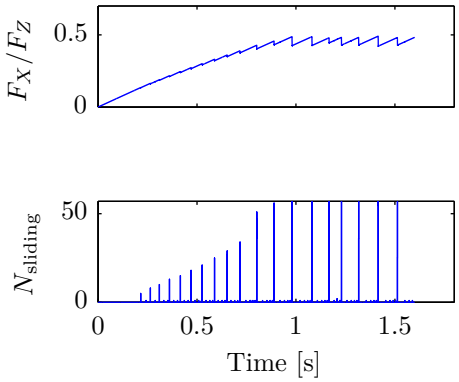

(b) $N_x = 57$, $N_z = 31$.

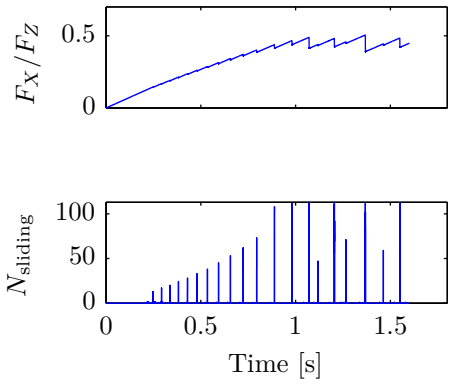

(c) $N_x = 113$, $N_z = 61$.

Figure 5.10: In the 1+1D model, the number of events is resolution independent because a pushing height $h > 0$ gives a loading zone of nonzero extension (shown in Figure 5.9). $h = 5$ mm, $k_{\text{ps}} = k$, $\Delta t = 0.4$, 0.2, 0.1 µs, remaining parameters as II in Table 5.1.

5.7 Length and number of precursors

Figure 5.12 shows the length of precursors in the 1+1D model, for parameters like those in [36]. It should be compared to Figure 5.11, which shows its experimental and 1D counterparts.

The shape of the curves agrees much better with experiment for the 1+1D than the 1D model, both qualitatively and quantitatively. The curve for $\theta = 0.833$ is rather straight, while the curves for $\theta = 0$ and $\theta = -0.833$ have increasing curvature. The very sharp increase in L_p between $F_X/F_Z = 0.4$ and 0.5 is still not observed, except for $\theta = -0.833$. The curves do not start at the origin, but at increasing F_X/F_Z values, a feature the 1D model failed to reproduce.

As well as the shape of the curves, the number of precursor events agrees well with experiment for the 1+1D model. In the experimental results the number of precursors longer than the ones preceding them is 27, 19 and 11 for $\theta = 0.833$, 0 and -0.833, respectively. In Figure 5.12 the numbers are 33, 15 and 12. Clearly, the non-uniform loading affects the number of precursors, and the 1+1D model can be used to understand this.

In the model, the number of precursors is controlled by the pushing height h, the sample length L, the load asymmetry θ and the friction coefficients μ_k and μ_s. To understand the influence of each, consider the force at the global static friction threshold, $\mu_s^{\text{global}} F_Z$, the force increment between events, $\Delta F_X^{\text{next event}}$, and the force reduction during each event, ΔF_X^{slip}. The number of precursors is

$$N_p = \frac{\mu_s^{\text{global}} F_Z}{\Delta F_X^{\text{next event}} - \Delta F_X^{\text{slip}}}. \tag{5.30}$$

Note that since $\Delta F_X^{\text{next event}}$ and ΔF_X^{slip} are not strictly equal between events, an exact calculation of N_p using this formula is not possible.

Figure 5.8 gives insight on equation (5.30). Observe that $\mu_s^{\text{global}} \gtrapprox \mu_k = 0.45$, which was discussed in Section 5.5.1. Also clear from the figure is that, for the current parameters, $\Delta F_X^{\text{next event}} \gg \Delta F_X^{\text{slip}}$, so that the latter can be ignored (this is not true for the global events, only for the precursors).

$\Delta F_X^{\text{next event}}$ is closely tied to the loading zone; the following order of magnitude calculation makes this plain. As a first approximation, assume that the force build-up is equal for all nodes within the loading zone, which has extent $2h$. After an event, the shear force lies on the dynamic friction level; the next event occurs when any node reaches the static friction level. For uniform normal load the total normal force on the nodes within the loading zone is roughly $F_Z \times 2h/L$. So, $\Delta F_X^{\text{next event}} \sim (\mu_s - \mu_k) F_Z 2h/L$. Combining these assumptions gives

$$N_p \sim \frac{\mu_k}{\mu_s - \mu_k} \frac{L}{2h} = \frac{1}{\frac{\mu_s}{\mu_k} - 1} \frac{L}{2h}. \tag{5.31}$$

For $\theta > 0$ the normal force within the loading zone is reduced, giving a larger number of events. This is reversed for $\theta < 0$.

It should be emphasized that equation (5.31) is not an exact result: with the parameters used in Figure 5.12, the equation predicts $N_p = 45$ for $\theta = 0$, while the simulation found $N_p = 15$ (although smaller than in the loading zone, there is an increase in the shear forces along the whole interface; this contribution to $\Delta F_X^{\text{next event}}$ has been

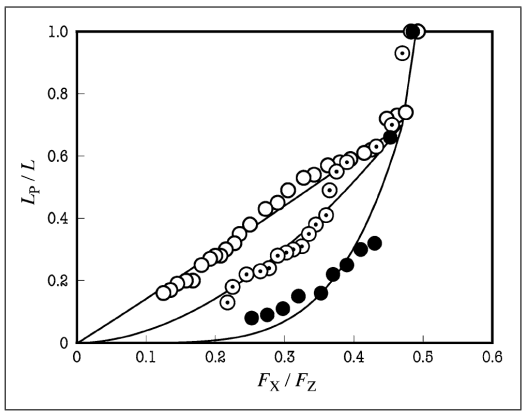

(a) Experimental results.

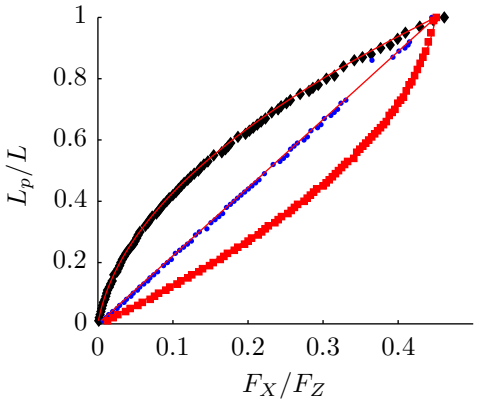

(b) 1D simulation results.

Figure 5.11: L_p–F_X from experiment and the 1D side driven model, repeated for ease of comparison with Figure 5.12. (a) is the same as Figure 3.7, (b) is the same as Figure 4.9.

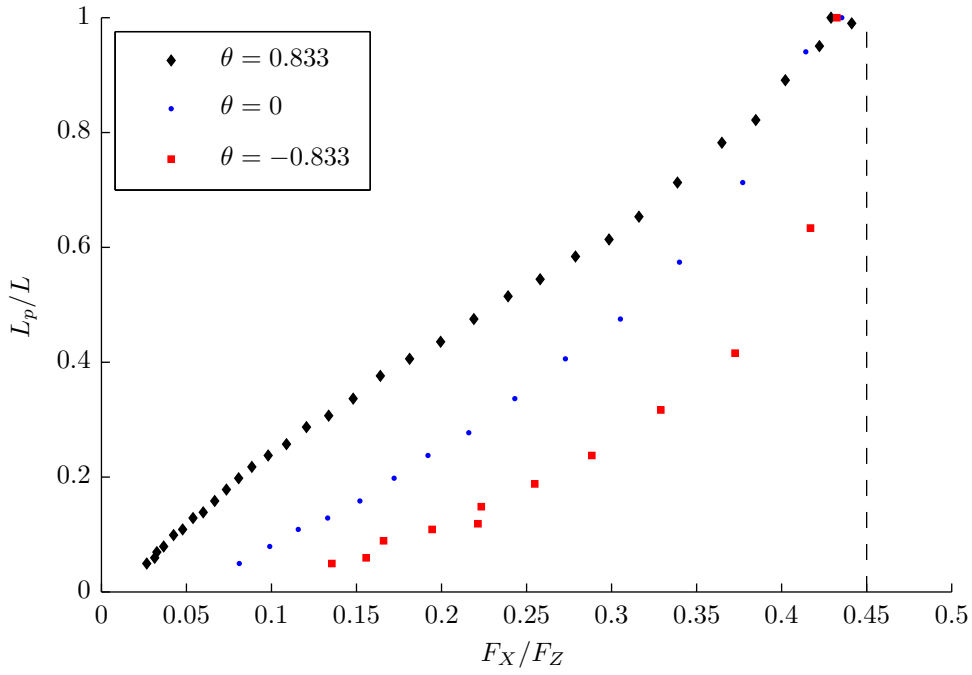

Figure 5.12: The effect of non-uniform static loading on the length of precursors in the 1+1D model. The dashed vertical line has the value of the local dynamic friction coefficient μ_k. $N_z = 21$, $\Delta t = 9 \cdot 10^{-8}$ s, $k_{\text{ps}} = k$, remaining parameters as I in Table 5.1. Top loading: pressure. F_X was measured at the arrest time of the events.

ignored). Nor is equation (5.31) a true scaling relation, i.e. doubling L does not necessarily double N_p. Rather, the equation makes plain the influence of each parameter: increasing h or μ_s/μ_k reduces N_p, increasing L increases N_p. It also shows that changing F_Z does not change N_p.

5.7.1 Importance of boundary conditions

Figure 5.12 demonstrates that a change in the boundary conditions (load distribution on top surface) significantly alters the shape of the L_p–F_X curve. In this section I demonstrate that subtler changes in the boundary conditions also have significant influence, and that by choosing boundary conditions similar to those in the experiments, a very good agreement with experimental results can be obtained.

An experimental L_p–F_X curve from Rubinstein et al. [48] was shown in Figure 3.6b. A more complete picture is given in Figure 5.13. The overall picture in (b) and (c) is a quasi-linear increase of low slope that starts away from the origin, and transitions to a higher slope near $L_p = L/2$. The number of events in (c) is 16 and 17 for $L = 0.2$ m and 13 for $L = 0.14$ m, in reasonable agreement with the scaling in equation (5.31) (compare $0.2/0.14 = 1.4$ to $16.5/13 = 1.3$). (d) shows collapse onto a master curve upon rescaling, note that I use a different scaling with L_p/L and F_X/F_Z, which rescales horizontally as well. (e) shows that by increasing h the number of events is increased while the shape of the curve stays the same.

Simulation results for $L = 140$ mm and parameters taken from the experiment are shown in Figure 5.14. The primary discrepancies from (c) and (e) are that the linear part is more curved in the simulations, and that transition to a higher slope is much more gradual. The way increasing h affects the number of events and the position of the leftmost point on each curve is in good agreement with experiment.

In Section 5.8 I introduce a top loading condition that is closer to the experimental condition by modelling the loading apparatus in more detail. Figure 5.15 shows that this improves the agreement with the experimental results: the linear part becomes longer and the transition becomes somewhat sharper. Because bringing the boundary conditions closer to the experimental ones brought the results closer to the experimental data, I will stick to this boundary condition from now on when studying the results of Rubinstein et al..

5.7.2 Numerical prediction of L_p–F_X

Within the 1D model I was able to find analytical expressions for L_p–F_X. I have not been able to do the same for the 1+1D model. In this section I explain the difference between the models that makes the analytical prediction scheme fail. I then present a next best solution, a prediction scheme that enables quasi-static calculation of L_p–F_X in the 1+1D model.

The analytical prediction in the 1D model depends on knowing the shear force distribution. Along the precursors, it was assumed to equal the dynamic friction level, and this assumption is still valid in the 1+1D model. To the right of the precursors the shear force was unchanged: unchanged with respect to the initial field if the slider is side driven, and unchanged with respect to the field just before the event if the slider it top driven. This is no longer the case in the 1+1D model. A local slip at the interface influences the shear force everywhere by force transfer through the deformation of the bulk.

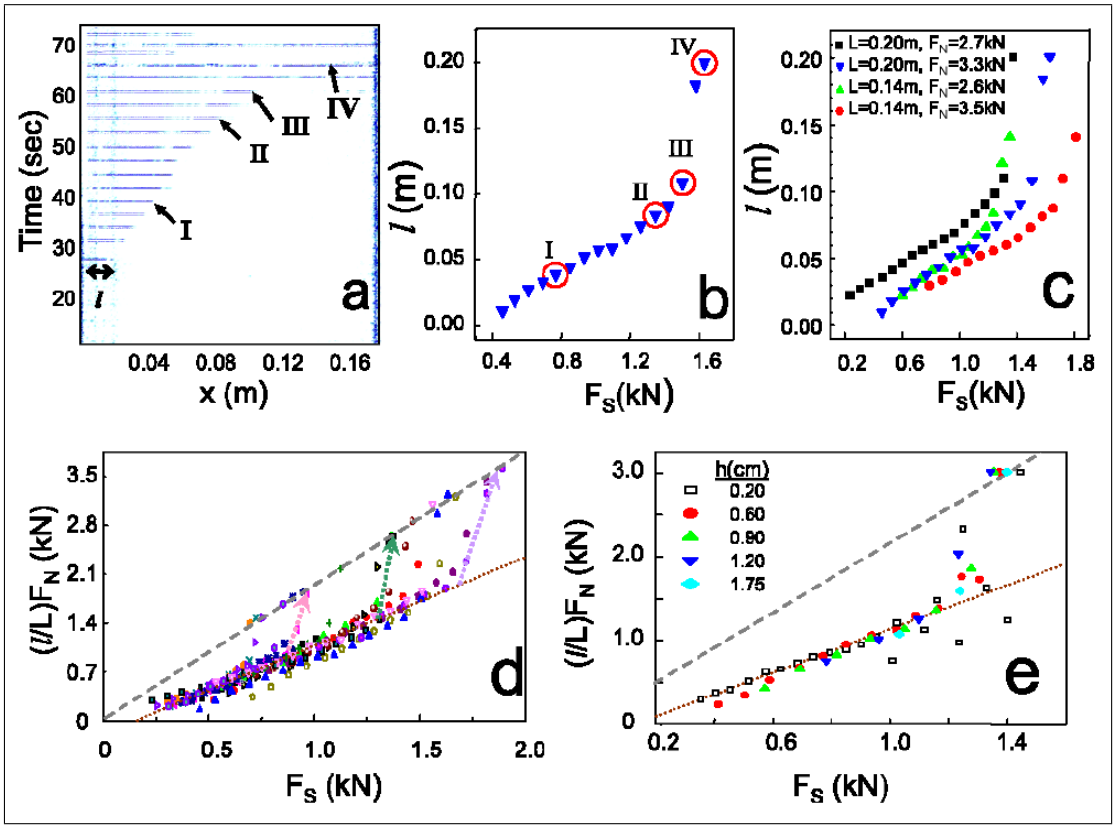

Figure 5.13: Experimental results for L_p–F_X taken from Rubinstein et al. [47]. Their l is my L_p, F_S is F_X, F_N is F_Z. (a) is included for completeness only and shows the temporal derivative $|\mathrm{d}A_{\mathrm{real}}(x,t)/\mathrm{d}t|$, for which I have no numerical counterpart. (b) shows L_p–F_X for the data in (a), without any rescaling by L and F_Z. (c) shows the data in (b) together with similar results for another sample length and other normal loads. (d) shows the data collapse of twenty-three experiments with $1.2 < F_Z < 4.0$ kN and $L = 140$, 200 mm. Note that they rescale by F_Z/L on the ordinate axis with no rescaling of the abscissa. In (b), (c) and (d) $h = 6$ mm. (e) includes different pushing heights h for an experiment with $L = 140$ mm. In (d) and (e) the grey dashed line is the Amontons–Coulomb law, i.e. it is drawn as a straight line from the origin through the point at which $L_p = L$. There is no legend or explanation of the brown dotted line.

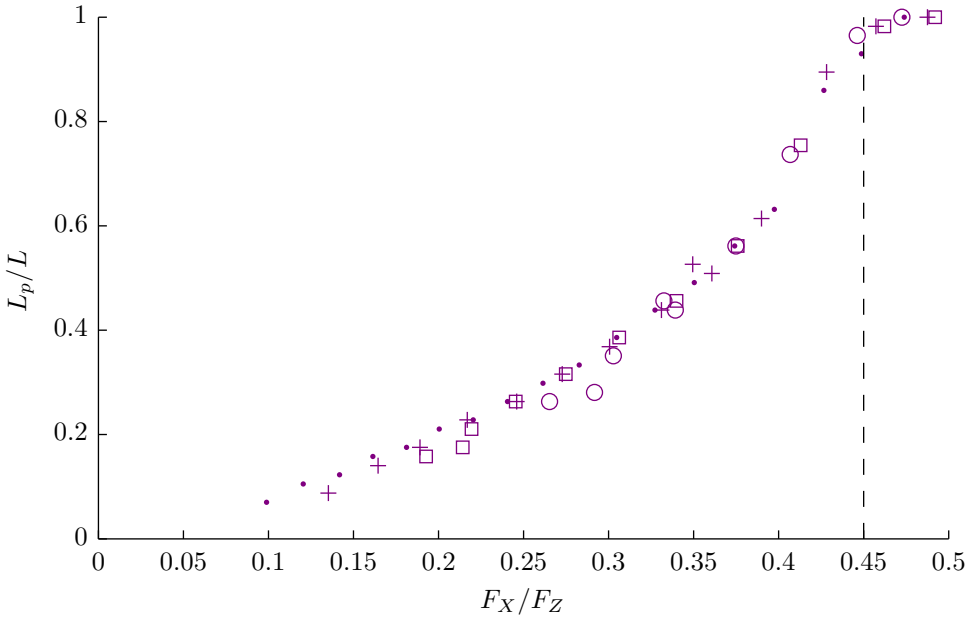

Figure 5.14: The length of precursors for parameters corresponding to [47]. Pushing heights $h = 2.5(\bullet)$, $5(+)$, $7.5(\square)$ and $12.5(\circ)$ mm. The dashed vertical line has the value μ_k. $N_z = 31$, $\Delta t = 2 \cdot 10^{-7}$ s, $k_{\text{ps}} = k$, remaining parameters as II in Table 5.1. Top loading: pressure. F_X was measured at the triggering time of the events. Precursors due to lifting of the leftmost node, relevant for $h > 7.5$ mm, have not been included.

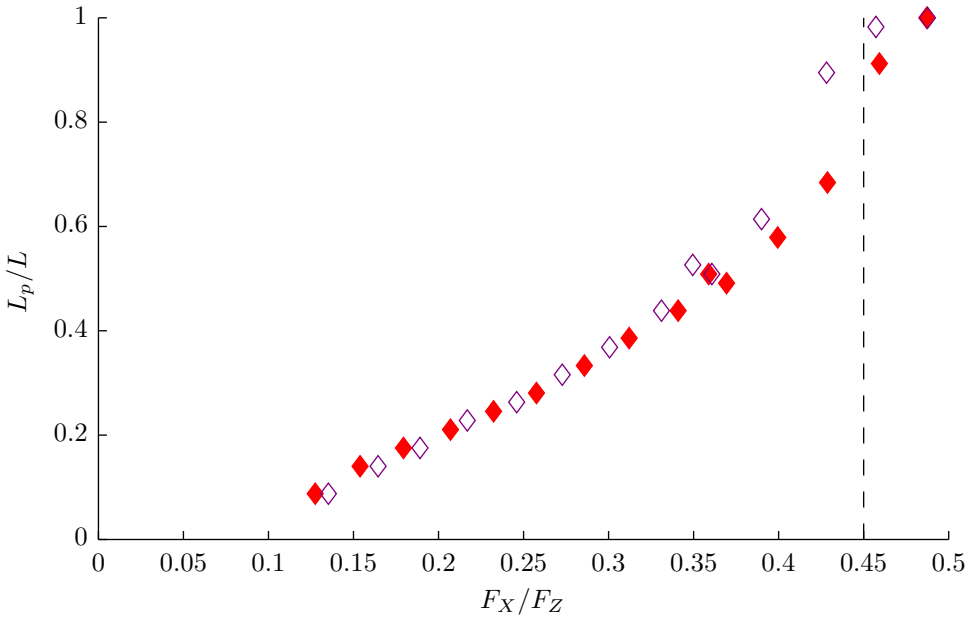

Figure 5.15: Changing the top boundary condition affects the L_p–F_X curve. Shown are open symbols for pressure condition (equal and constant vertical force on each top node, same data as $(+)$ markers in Figure 5.14) and filled symbols for the spring mattress condition of Section 5.8. The dashed vertical line has the value μ_k. $h = 5$ mm, $N_z = 31$, $\Delta t = 2 \cdot 10^{-7}$ s, $k_{\text{ps}} = k$, remaining parameters as II in Table 5.1. F_X was measured at the triggering time of the events.

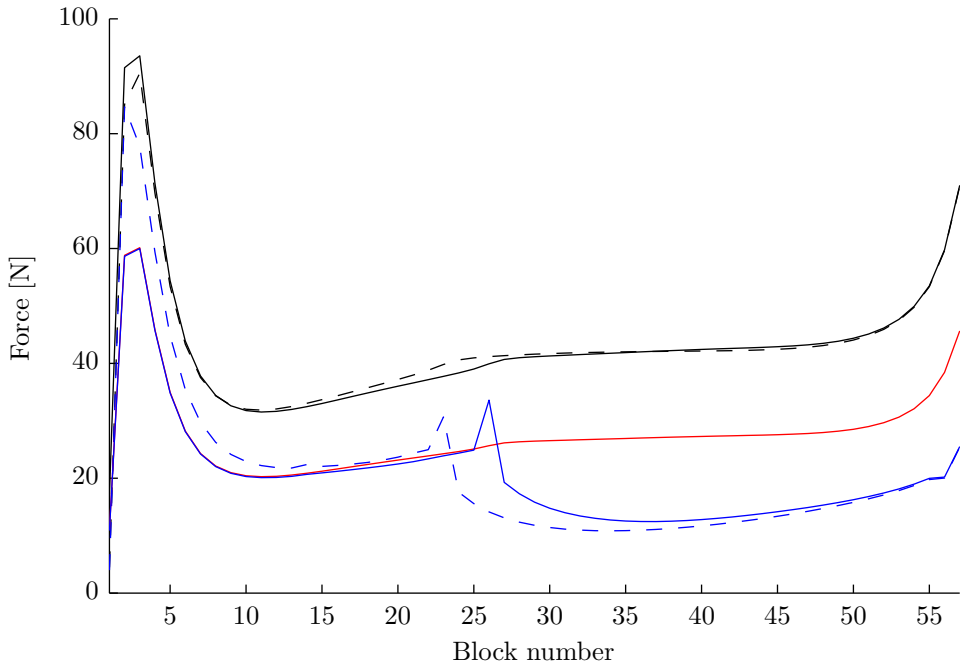

Figure 5.16: The force distributions before (dashed) and after (drawn) an event. Shown are the static friction threshold (black), dynamic friction level (red) and shear force (blue) profiles. $h = 5\,\mathrm{mm}$, $N_z = 31$, $\Delta t = 2 \cdot 10^{-7}$ s, $k_{\mathrm{ps}} = k$, remaining parameters as II in Table 5.1. Top loading: spring mattress.

Figure 5.16 shows the force profiles before and after an event. The normal force remains close to its value before the event as seen in the static friction threshold, but the shear force profile changes significantly both along the precursor and to its right. The spikes at 23 and 26 signify the stopping points of the previous and the present precursors. After the event, the shear force along the precursor is very close to the dynamic friction level.

A prediction of L_p–F_X is obtained by setting $\mu_s = \mu_k$ and re-running the simulation. This gives the right shear force profile: along the precursors, the shear force obtains the dynamic friction level as it should. To the right of the precursors, the shear force is determined by the bulk deformations, which are in turn determined by the pushing force F_X and the slipped distance along the precursor. Given L_p, F_X and the shear forces along the precursor for a given parameter set, the slipped distance at each point along the precursor is uniquely determined.

Setting $\mu_s = \mu_k$ allows a quasi-static calculation. The effect of inertia is essentially that a moving block's linear momentum makes it overshoot the point where the net force on it becomes zero. For $\mu_s = \mu_k$ the acceleration of a block is always small and so very little linear momentum is gained. This eliminates the overshooting, and inertia can be neglected.

When $\mu_s = \mu_k$ the discrete precursor events are replaced by a gradual lengthening of the slipping zone, as shown in Figure 5.17. I define the force corresponding to a given length $L_p = jL/N$ as the value of F_X when node $j+1$ starts sliding. When the slipping zone reaches the leading edge the system enters a stick–slip regime. Because each stick and slip period is very brief when $\mu_s = \mu_k$, the line width of the plot is wider than the

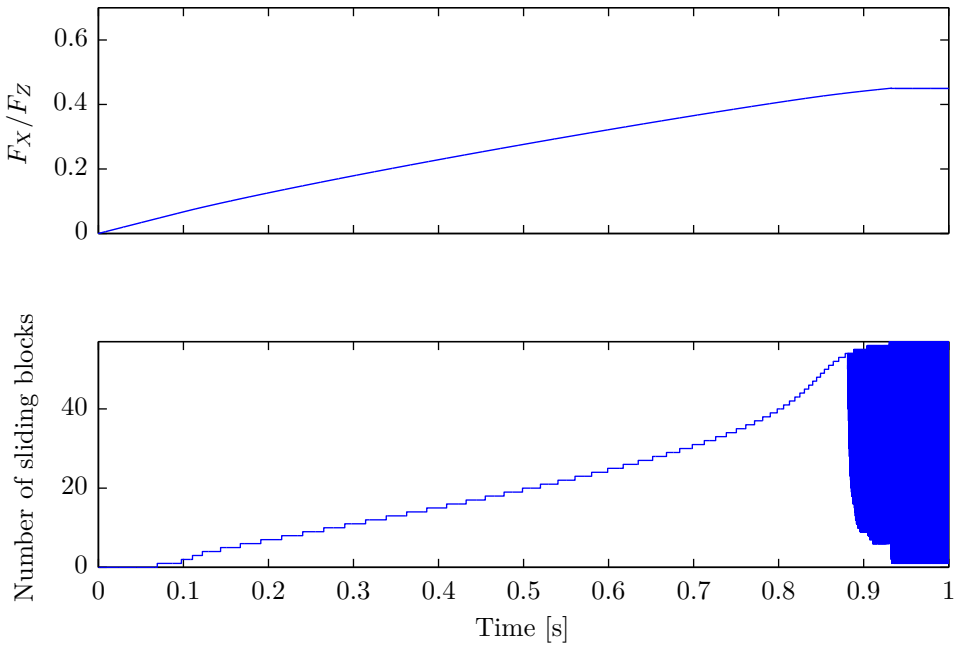

Figure 5.17: Setting $\mu_s = \mu_k$ changes the discrete slip events into a gradual lengthening of the slipping zone. $h = 2.5$ mm, $N_z = 31$, $\Delta t = 2 \cdot 10^{-7}$ s, $k_{\text{ps}} = k$, remaining parameters as II in Table 5.1. Top loading: spring mattress.

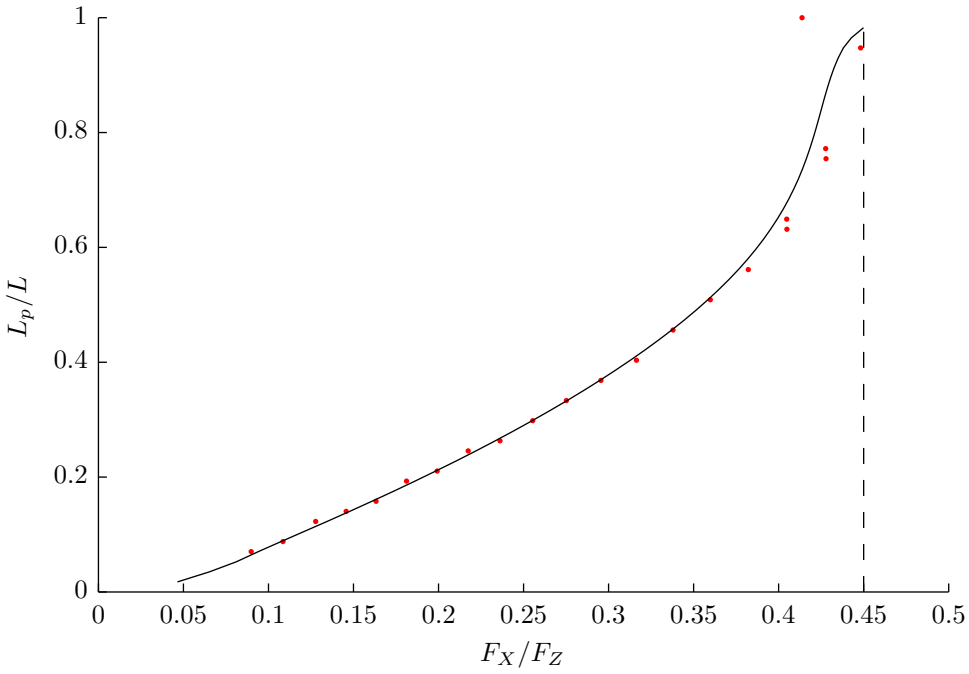

Figure 5.18: Setting $\mu_s = \mu_k$ gives a prediction of the length of precursors, shown as a drawn line. The discrete points correspond to $\mu_s = 0.7$, $\mu_k = 0.45$. $h = 2.5$ mm, $N_z = 31$, $\Delta t = 2 \cdot 10^{-7}$ s, $k_{\text{ps}} = k$, remaining parameters as II in Table 5.1. Top loading: spring mattress. F_X was measured at the arrest time of the events.

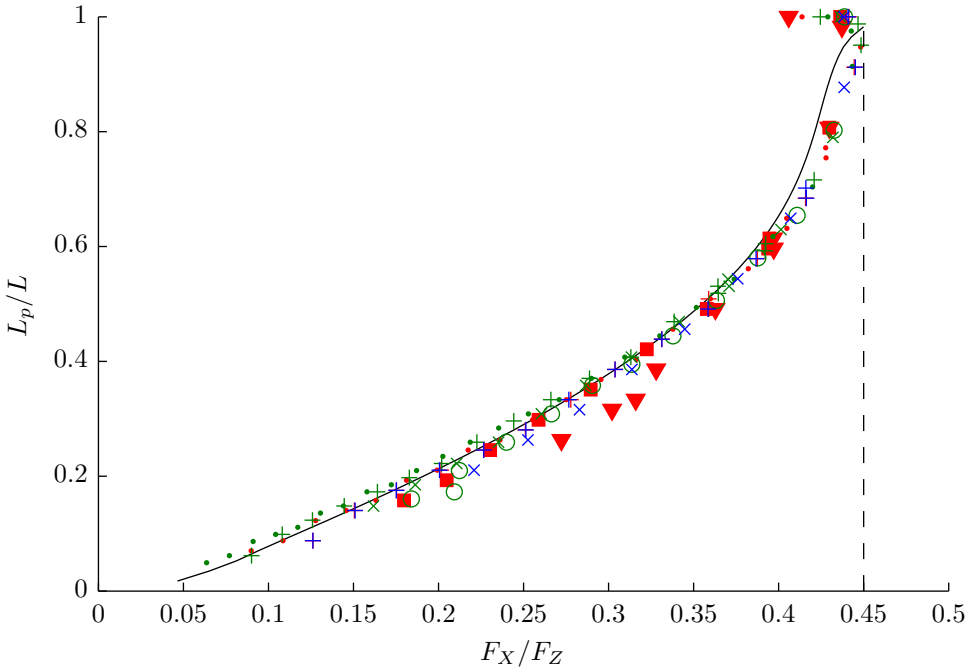

Figure 5.19: The length of precursors as a function of the driving force follows a master curve when different simulations are rescaled by their L and F_Z. Markers denote pushing heights $h = 2.5(\bullet)$, $5(+)$, $7.5(\square)$, $10(\times)$, $12.5(\circ)$ and $15(\triangledown)$ mm. Colours are: red: $L = 140$ mm, $F_Z = 3.5$ kN; blue: $L = 140$ mm, $F_Z = 1.75$ kN; dark green: $L = 200$ mm, $F_Z = 2.7$ kN. The drawn line is a prediction with $\mu_s = \mu_k = 0.45$ and $h = 2.5$ mm. The dashed vertical line has the value of the local dynamic friction coefficient μ_k. $N_z = 31$, $k_{\text{ps}} = k$, $\Delta t = 2 \cdot 10^{-7}$ s. Remaining parameters as II and III in Table 5.1. Top loading: spring mattress. F_X was measured at the arrest time of the events.

time intervals and the graph appears solid.

In the experiments the force F_X is measured *before* the events. However, the assumption that the shear force lies on the dynamic friction level along the precursor is only valid after events, as Figure 5.16 shows. To investigate the accuracy of the prediction scheme with $\mu_s = \mu_k$, therefore, F_X should be measured *after* each event in the full simulations with $\mu_s > \mu_k$. Figure 5.18 shows that the prediction scheme agrees very well with the full simulation. The discrete point at $L_p = L$ has a smaller F_X than previous points because of the large relaxation of the driving force associated with a global sliding event.

Figure 5.19 shows that scaling L_p–F_X by L and F_Z does indeed collapse different simulations on the same master curve. In Appendix C.3 I discuss a subtle point related to the collapse of curves for different values of h.

5.8 Modelling an experimental normal loading condition: the spring mattress

In the experiments of Rubinstein et al. [48], normal force was imposed on the slider via a soft spring array, as shown in Figure 5.20. In modelling this, I have tried to capture the dynamics of the spring mattress without having to implement the inner details of

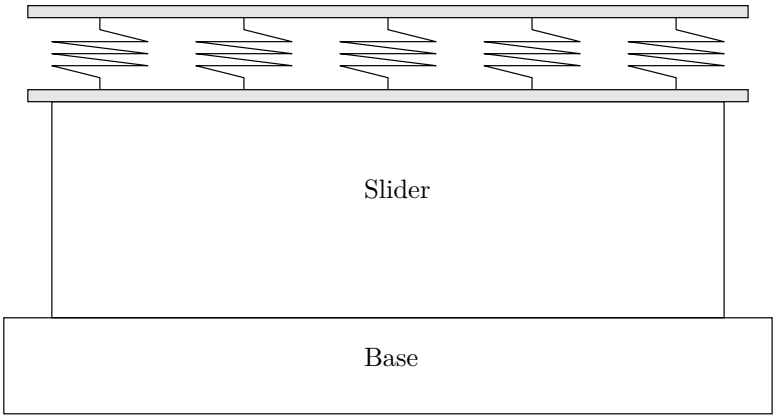

Figure 5.20: Normal force is imposed on the slider via an array of soft springs sandwiched between two rigid plates.

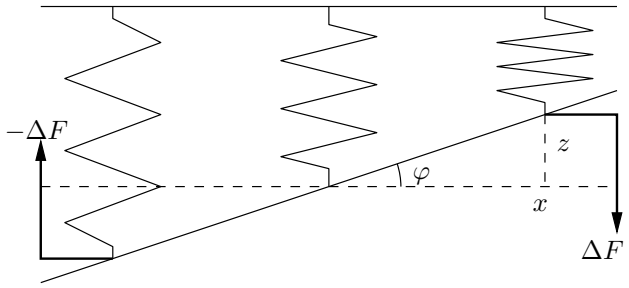

Figure 5.21: The restoring force at x depends on the angle φ.

the mattress. This relies on the following understanding of how the mattress behaves.

The lower plate is *rigid* and glued (stuck) to the slider. In the model this means that the uppermost layer of nodes is not allowed to deform. The top plate is also rigid, and undergoes pure translations, but no rotations. Although not explicitly stated in the experimental papers, the term *translational stage* suggests this restriction. Furthermore, the external normal force on the top plate is assumed to be a constant, independent of vertical displacement. This force is transmitted to the lower plate via springs distributed along the length of the plates. There are no external horizontal forces on the top plate.

If the lower plate rotates, the springs set up a restoring torque that I will calculate shortly. The net effect of the spring mattress on the slider is thus threefold: a normal force that is approximately constant, since the spring mattress is soft; the constraint that the upper layer of nodes cannot deform; and a restoring torque upon rotation of the upper layer. Neglecting inertial effects of the top plate, the spring mattress can be modelled as a rigid rod upon which act a constant normal force in the centre of mass, a torque that depends on the angle of rotation, and the forces acting on the top blocks from the rest of the slider.

In the continuum approximation to a large number of linear springs connected in parallel along a length L and having a total stiffness K_{mat}, the stiffness within an interval Δx is $\Delta K_{\mathrm{mat}} = K_{\mathrm{mat}} \frac{\Delta x}{L}$. For small angles φ the length change $z(x)$ of the spring equivalent at x is $z(x) \approx x \tan(\varphi) \approx x\varphi$, as is shown in Figure 5.21. The length x is measured from the centre of mass at $L/2$. The force on a small line element is

$\Delta F(x) = K_{\mathrm{mat}} x\varphi \frac{\Delta x}{L}$. The torque is

$$\Delta\tau = x\Delta F = -K_{\mathrm{mat}} x^2 \varphi \frac{\Delta x}{L}. \tag{5.32}$$

In the limit of small Δx, the total torque from the spring mattress is

$$\tau = \int_{-L/2}^{L/2} \Delta\tau \tag{5.33}$$

$$= \frac{K_{\mathrm{mat}}\varphi}{L} \int_{-L/2}^{L/2} x^2 \mathrm{d}x \tag{5.34}$$

$$= \frac{K_{\mathrm{mat}} L^2}{12}\varphi, \tag{5.35}$$

with the positive direction into the plane of the model.

The torque on the rigid rod from each force acting on the top nodes is

$$\tau_i = \mathbf{r}_i \times \mathbf{F}_i \tag{5.36}$$

$$= -x_i F_{z,i} + z_i F_{x,i}, \tag{5.37}$$

still with the positive direction into the plane of the model. Here, (x_i, z_i) is the position of top node i relative to the centre of mass of the rigid rod. A sum over the top nodes gives the total contribution to the torque.

Imposing the no deformation constraint is straightforward. Initially, each top node has a position along the rigid rod, which it should maintain. Instead of moving the top nodes independently, the rigid rod is treated as an inertial object having a mass M_{mat}, a centre of mass position and an angle of rotation. In each step of the integration algorithm, the rod moves under the influence of the net force and torque from external forces and the forces on the top nodes. Then, the positions and velocities of the top nodes, which serve as the attachment points to the rest of the slider, are given by the blocks' positions on the rod. As M_{mat} is not given in the experimental papers, I have used $M_{\mathrm{mat}} = M$ throughout.

5.9 Force profiles

The local frictional response is determined by the shear and normal force profiles: slip starts when the external shear force overcomes the local shear strength, which is proportional to the normal force. It makes sense, therefore, to measure these profiles, and to compare to them to experiments.

Initially the normal force profile is weakly non-uniform. At the left and right edges of the slider–track interface are the corners of the slider, and from continuum mechanics one expects large edge effects when the corners become infinitely sharp. In the model these end effects are smoothed by the coarseness of the grid and the potential surface that represents the track, but they are still present, as can be seen in Figure 5.22. The figure should be compared to the dashed lines in Figure 3.9, its experimental counterpart. (The drawn lines of this figure correspond to *uniform shear loading* similar to the 1D top driven model, and should not be compared to my 1+1D simulation results.) The experimental figure shows uniform normal force distribution away from the edges; at the very edges there are no measurement points. As far as can be told, the initial normal force profile agrees with experiment.

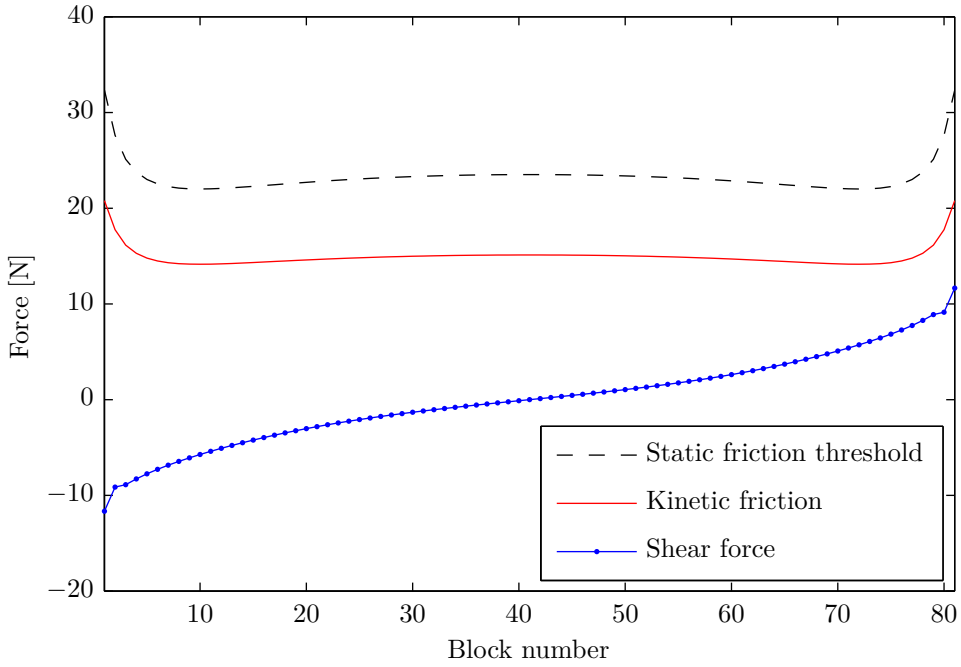

Figure 5.22: The initial force profiles in the 1+1D model. The effect of the slider corners are clearly seen as increases in the normal force at the left and right edge. $N_x = 81$, $N_z = 31$, $k_{\mathrm{ps}} = k$, remaining parameters as III in Table 5.1.

The initial shear force profile is anti-symmetric and agrees well with experiment. The experimentalists explain the effect by differential Poisson expansion frustrated at the interface, which I discussed in Section 4.4.3. In the 1+1D model there is no Poisson expansion of the potential surface that represents the track, and so the differential expansion is maximised.

The normal force profile changes throughout the precursor sequence; the change occurs both during the loading between events and as a result of the partial slips. The real area of contact A_{real} is essentially proportional to the local normal force, and so the two can be compared. Figure 5.23 shows $w_i(t)$ normalised by the value at $t = 0$ for every second precursor in a particular simulation. The figure is in excellent agreement with Figure 5.24, which shows the evolution of A_{real}. The normal force develops a peak near the trailing edge followed by a deepening valley and a tail that is essentially unchanged after the short precursors. As the precursors become longer, a peak develops at the leading edge as well. Also, in the inset of global events, the profile remains unchanged between events, just as it does in the experiments. Exact quantitative comparison is not possible, because the normal force profile has a constant sum/integral $\sum_i w_i = W = F_Z$, while the experimentally reported A_{real} does not: it is reduced upon sliding. And even if quantitative comparison was possible, I would expect discrepancies in the edge effects. In the experiments, the PMMA slider rests on a PMMA track, whereas in the simulations the track is an elastic potential that does not deform at all. I have considered modelling the PMMA track in a similar way as the slider to see if this gave even better agreement, but concluded that the constant sum/integral of the normal force would still preclude quantitative comparison.

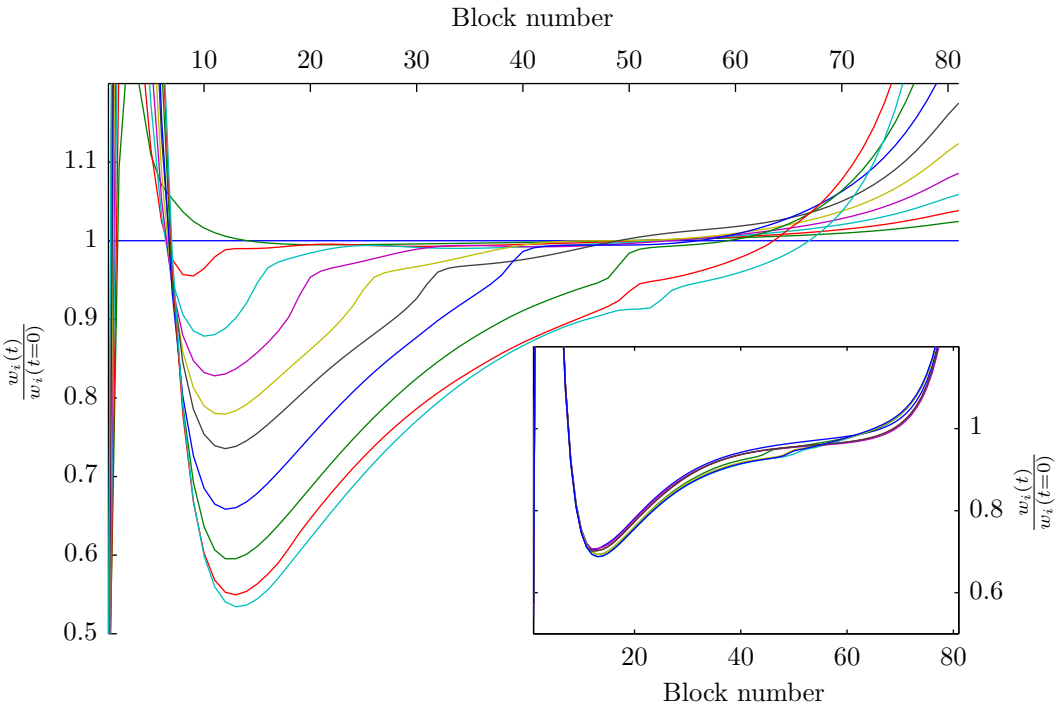

Figure 5.23: The normal force profile evolves with F_X and L_p. Shown are profiles taken at the point of arrest of the last slipping node for every second precursor (main) and the global events (inset). $h = 5$ mm, $N_x = 81$, $N_z = 31$, $k_{\text{ps}} = k$, $\Delta t = 2 \cdot 10^{-7}$ s, remaining parameters as III in Table 5.1.

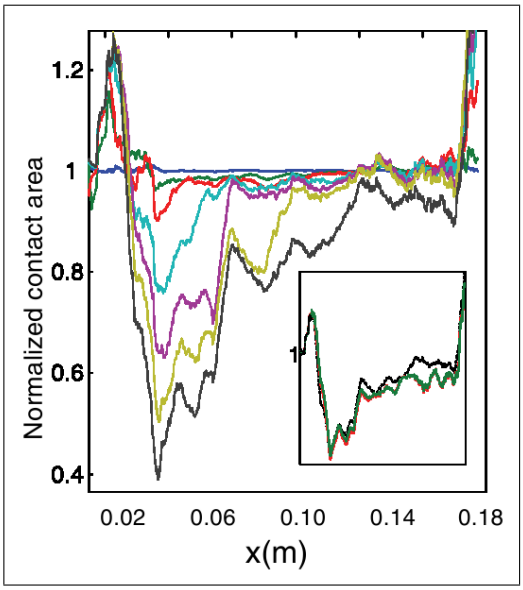

Figure 5.24: Evolution of the real area of contact. Each graph is $A_{\text{real}}(x, t = \text{constant})/A_{\text{real}}(x, 0)$ with t measured from the start of the experiment. The profiles were taken subsequent to every third precursor. The inset shows three profiles; one taken immediately prior to global sliding and two taken immediately following consecutive sliding events. Taken from Rubinstein et al. [47].

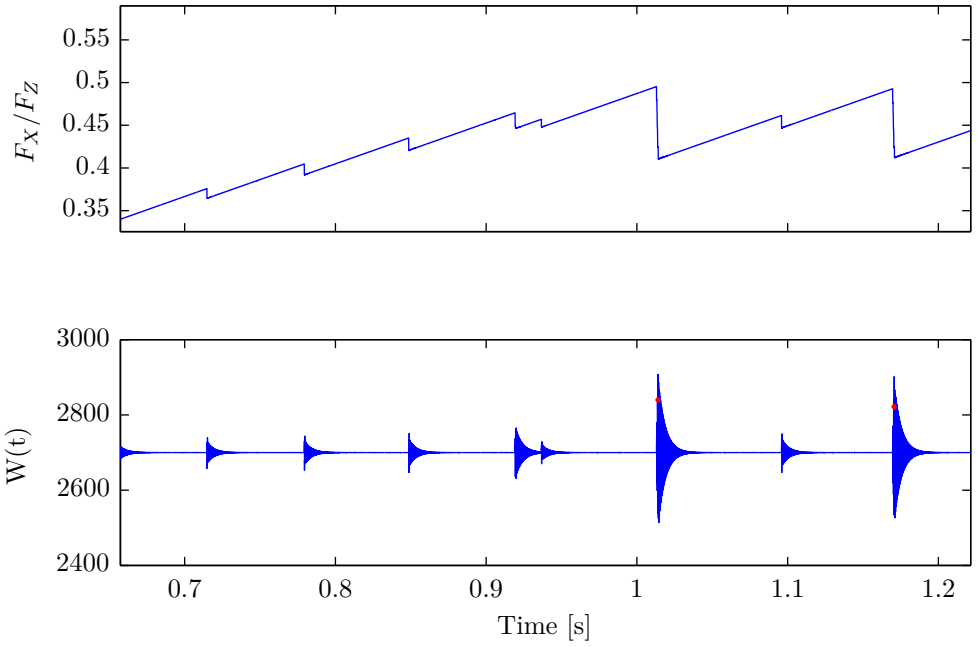

Figure 5.25: The normal force from the track, $W(t)$, indicates the duration of the oscillations associated with each event. The red dots show the point of arrest for the two global events; notice how much longer the oscillations persist. The same simulation as Figure 5.23, i.e. $h = 5$ mm, $N_x = 81$, $N_z = 31$, $k_{\text{ps}} = k$, $\Delta t = 2 \cdot 10^{-7}$ s, remaining parameters as III in Table 5.1.

5.9.1 Oscillations in the normal force W

To measure the normal force profile immediately after precursors you need a criterion defining when a precursor, or any event, ended. I have used the *point of arrest* of the last slipping node, i.e. the instant in time when all the blocks at the slider–track interface have come to rest. In 1D there is no reason to question this choice: all the blocks are at the slider–track interface, so when the last of them comes to rest, nothing at all happens except for the driving force increasing, eventually triggering the next event. In 1+1D, however, there are waves in the bulk that do not die out immediately upon the cessation of slip, and a disadvantage of using the point of arrest to determine the end of an event is that the shear and normal force profiles are not constant in time when they are measured.

An alternative definition of the end of an event is to require the oscillations associated with the event to have died out. However, this requires the time between events to be much longer than the time it takes for oscillations to disappear. Figure 5.25 shows that for the present parameters, oscillations persist for approximately one third of the time between events. By the time the oscillations have died out, therefore, the change in the loading force has been significant. Trivially, lowering V increases the time between events and enables the alternative definition to be applied, but since this also increases the time it takes to run a simulation, I have chosen to measure force profiles at the point of arrest, despite the disadvantages.

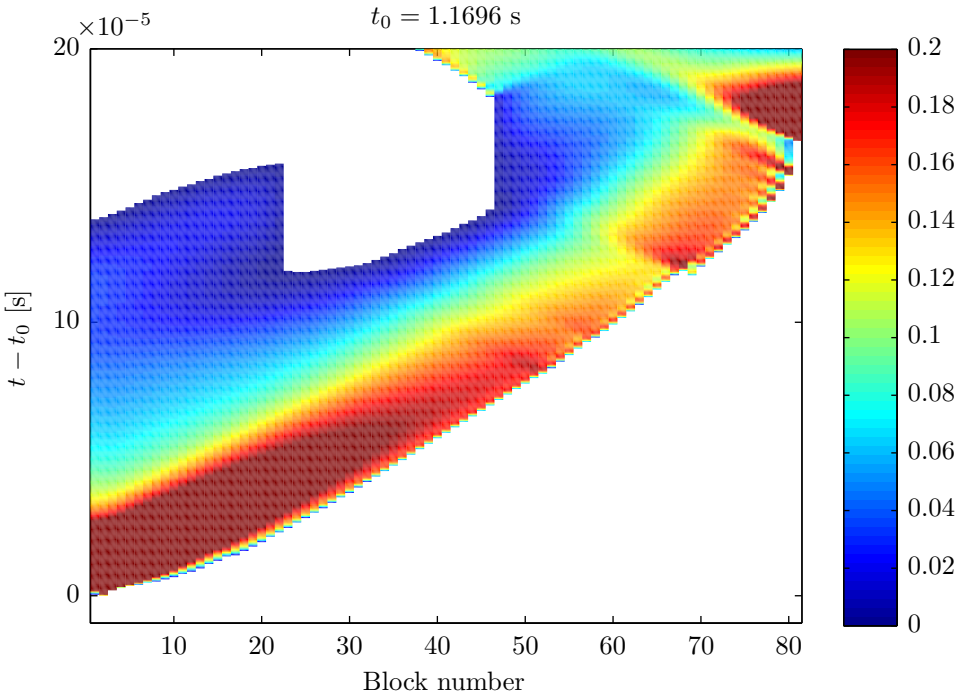

Figure 5.26: Time evolution of the local block velocity during a global event. Only the x-components are shown. The numbers on the colourbar are velocities in units of metre per second (values higher than the maximum on the colourbar exist). The end of the event is not shown. $h/H = 1/15$, $N_x = 81$, $N_z = 31$, $k_{\text{ps}} = k$, $\Delta t = 2 \cdot 10^{-7}$ s, remaining parameters as III in Table 5.1. Top loading: spring mattress.

5.10 Crack front velocities

Each precursor and global event starts with a crack-like rupture travelling outwards from a nucleation point. Motion at the interface initiates where the static friction threshold is first exceeded, then spreads in a wave-like manner as successive neighbours are brought above their friction thresholds. A space-time plot of the local slipping velocity illustrates this, see Figure 5.26.

The speed of the crack front, v_{crack}, is the inverse of the slope between the slipping and pinned regions in Figure 5.26. In principle it can be measured in every point along the interface as

$$v_{\text{crack},i} = \frac{l}{\Delta t_i^{\text{trigger}}}, \tag{5.38}$$

where l is the distance between nodes and $\Delta t_i^{\text{trigger}} = t_{i\pm1}^{\text{trigger}} - t_i^{\text{trigger}}$ is the time from node i started to move to node $(i \pm 1)$ started to move. The plus would be a front travelling to the right, and the minus would be a front travelling to the left. I have only considered fronts travelling towards the right, as most events nucleate near the trailing (left) edge.

However, with $v_{\text{crack},i} \approx 10^3$ m/s and $l = 2.5$ mm with $N_z = 31$, which I typically use, $\Delta t_i^{\text{trigger}} \approx 2 \cdot 10^{-6}$ s $= 10\Delta t$. This is highly unsatisfactory, as the resolution in possible values of v_{crack} will be very poor. Moreover, for speeds of $v_{\text{crack}} = l/(8.5\Delta t)$, say, there will be a sawtooth pattern when v_{crack} is plotted as a function of position,

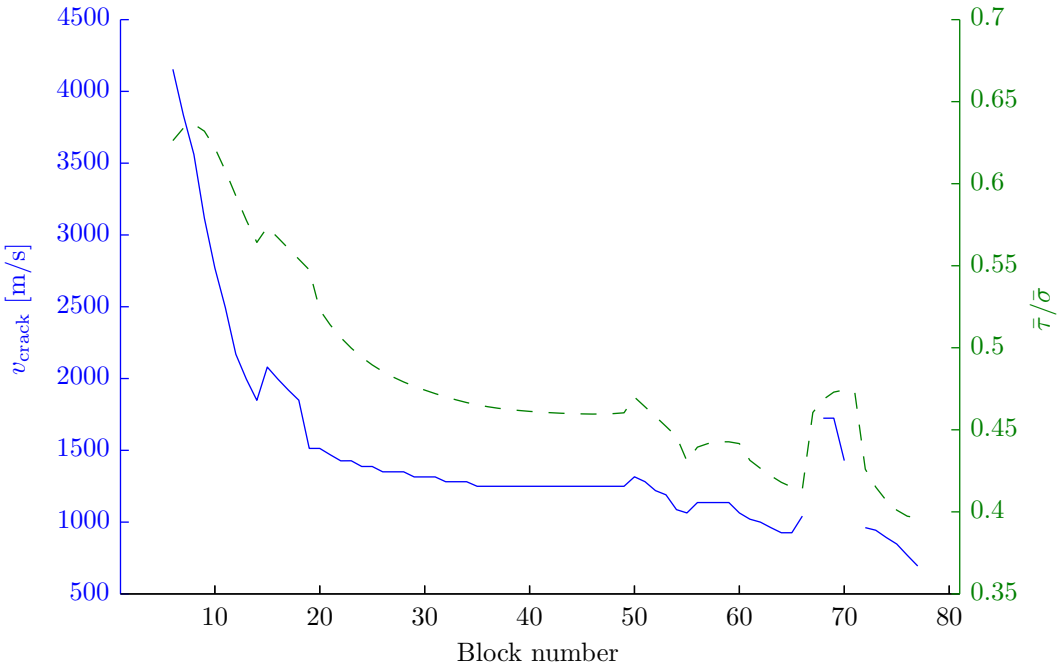

Figure 5.27: The crack front velocity and the stress ratio at the beginning of the event shown in Figure 5.26. Note the high degree of correlation between them.

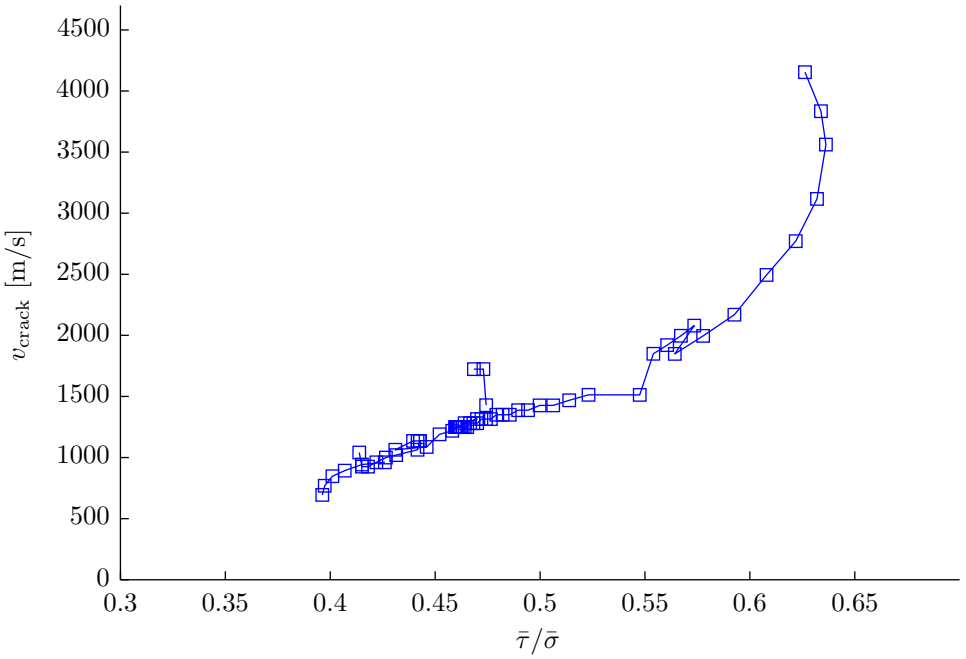

Figure 5.28: The crack front velocity as a function of the stress ratio for the data in Figure 5.27.

as alternating $\Delta t^{\text{trigger}}$ become 8 and $9\Delta t$. My chosen solution is to use a wider spatial region to define v_{crack}, similar to using a moving average. I define

$$v_{\text{crack},i} = \frac{x_{i+i_w} - x_{i-i_w}}{\Delta t_i^{\text{trigger}}}, \tag{5.39a}$$

$$\Delta t_i^{\text{trigger}} = t_{i+i_w}^{\text{trigger}} - t_{i-i_w}^{\text{trigger}}, \tag{5.39b}$$

where i_w is the width of the region over which I average. I have used $i_w = 2$. Compressions are small, so $x_{i+i_w} - x_{i-i_w} \approx 2i_w l = 4l$.

In Figure 5.26 one observes the anomalous behaviour that node $i = 69$ started moving before nodes $i = 67$ and 68. Inspection of the associated stress fields before the event reveals a spike at $i = 69$. Because such spikes are discreteness effects closely tied to the lattice spacing I have excluded v_{crack} measurements where $t_{i+1}^{\text{trigger}} < t_i^{\text{trigger}}$ enters; here, I exclude $v_{\text{crack},67}$ and $v_{\text{crack},71}$, since $i_w = 2$.

Ben-David et al. [7] plot v_{crack} as a function of the local shear to normal force/stress ratio τ/σ. I will do the same, using average values

$$\bar{\sigma}_i = \frac{1}{2i_w + 1} \sum_{j=i-i_w}^{i+i_w} \sigma_j = \frac{\sigma_{i-2} + \sigma_{i-1} + \sigma_i + \sigma_{i+1} + \sigma_{i+2}}{5}, \tag{5.40}$$

the same for τ. Note that τ and σ are measured *at the time of event initiation*. Figure 5.27 shows the close correspondence between $v_{\text{crack},i}$ and $\bar{\tau}_i/\bar{\sigma}_i$. Figure 5.28 shows the velocity as a function of the stress ratio.

If v_{crack} is plotted versus $\bar{\tau}/\bar{\sigma}$ for all events in a simulation, the lines collapse on a master curve. This is shown in Figure 5.29, which includes the data in Figure 5.28. The four events exhibiting an unexpected increase in v_{crack} for small and decreasing $\bar{\tau}/\bar{\sigma}$ were all triggered a small distance away from the trailing edge. Then, in addition to the crack front propagating to the right, a leftwards travelling front was generated. This was reflected at the trailing edge, and the reflected wave travelled in the bulk, faster than the surface crack wave still moving to the right. The increase in v_{crack} coincides with the crack front being overtaken by the reflected wave. Figure 5.30 shows the nucleation point, the left- and rightwards travelling waves, and the reflected wave overtaking the crack front. That the reflected wave travelled in the bulk can not be seen from the figure, which only shows the local velocities at the slider–track interface.

Changing L and F_Z does not affect the master curve, as will be seen by the collapse of the third and fourth data sets in Figure 5.31a.

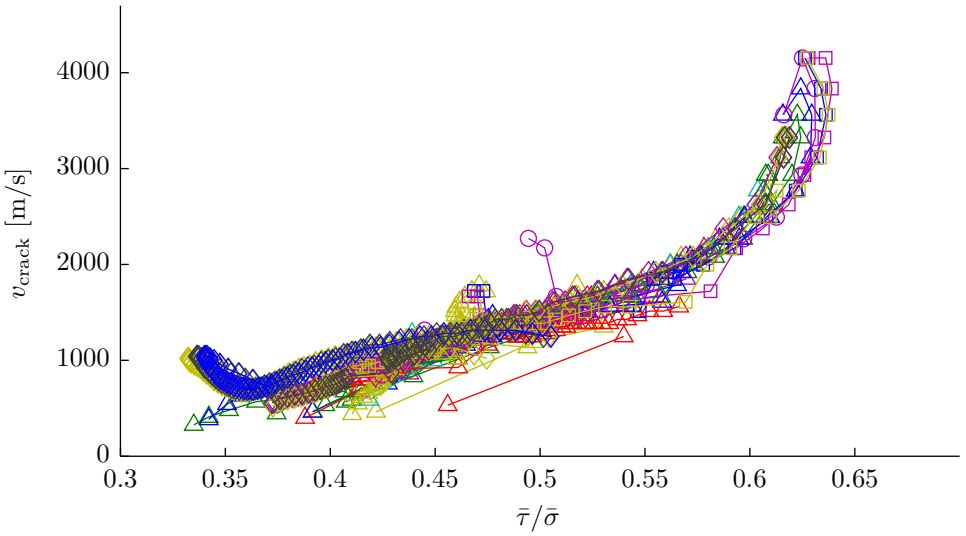

Figure 5.29: Crack front velocities for all multi-node events in a simulation. There is a rough data collapse and a common trend: lower $\bar{\tau}/\bar{\sigma}$ correspond to lower velocities. Event triggering occurs at high values of $\bar{\tau}/\bar{\sigma}$. Data points belonging to the same event all have the same colour, but different events may share a colour. The markers are: triangles for the precursors, circles for the first event to reach the leading edge, squares for later events in which all blocks moved simultaneously, diamonds for other events following the first global one. $h/H = 1/15$, $N_z = 31$, $k_{\mathrm{ps}} = k$, $\Delta t = 2 \cdot 10^{-7}$ s, remaining parameters as III in Table 5.1. Top loading: spring mattress.

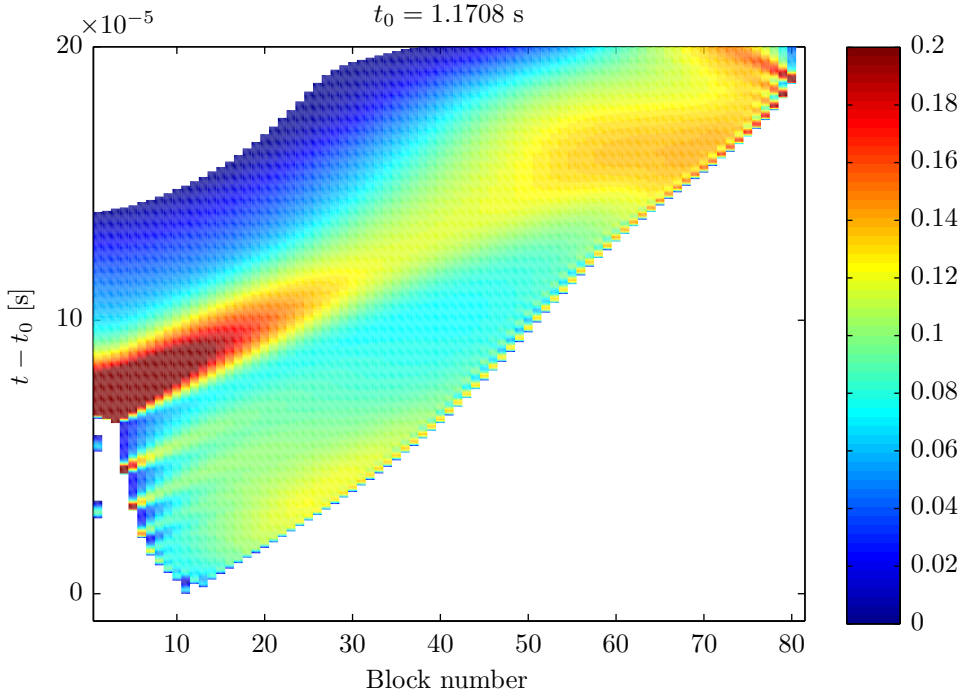

Figure 5.30: Time evolution of the local block velocity during one of the events in Figure 5.29 that triggered a small distance away from the trailing edge. Only the x-components are shown. The numbers on the colourbar are velocities in units of metre per second (values higher than the maximum on the colourbar exist). Note the pulse of higher velocities that is reflected from the trailing edge and overtakes the crack front near the leading edge. This pulse explains the anomalous increase in velocities evident in the lower left part of Figure 5.29.

5.10.1 Data collapse for different μ_k, μ_s

The ratio τ/σ does not by itself determine the propagation of the crack front: the friction coefficients enter in the picture as well. For instance, with a carefully prepared interface with every node at the static friction threshold, $\tau = \mu_s\sigma$ in continuum notation, the crack propagates infinitely fast: each block has to move but a negligible distance and its neighbour starts moving as well. In the 1D model, Amundsen [1] and Muratov [39] found that data collapse is obtained if the parameter

$$\boxed{\tilde{\tau} = \frac{\tau/\sigma - \mu_k}{\mu_s - \mu_k}} \tag{5.41}$$

is used. This relates the shear to normal stress before the event (τ/σ) to the static and kinetic interface strength (μ_s and μ_k).

Figure 5.31a shows that a change in μ_k, μ_s or both shifts the master curve of Figure 5.29. In Figure 5.31b, using $\tilde{\tau}$ on the abscissa produces data collapse, indicating that $\tilde{\tau}$ is the deciding parameter in 1+1D as well. For the sake of completeness I have included in Appendix C.4 a figure with more deviations from the master curve; I interpret them as transient parts of anomalously triggered events.

5.10.2 Deviations from experiment

Comparing Figure 5.29 to the experimental results in Figure 5.32 reveals major discrepancies. Perhaps most striking is the difference in the range of τ/σ values that occur. For the current friction coefficients, adjusted in Section 5.5.1 to give the best agreement with the experimental loading curve, and that also fit well with the number of precursors, τ/σ takes values in $[0.3, 0.7]$, the absolute upper limit being the value of μ_s. In the experiment, on the other hand, $\tau/\sigma \in [0.3, 2.5]$, with about half the measurements exceeding 0.8. The experimental results for the loading curve and the precursors were taken from a different article than the velocities, and perhaps the friction coefficients that best fit the samples used to produce Figure 5.32 are different? Figure 5.31a shows that changing the friction coefficients in the model changes the range of τ/σ; however, increasing μ_s to 2.5 would destroy the good agreement seen in earlier sections, and it is unlikely that the samples used in the different experiments are *that* dissimilar.

Allowing the blocks to have different friction coefficients, on the other hand, is an interesting extension of the model that could possibly reproduce the large range of stress ratios. In fact, the experiments indicate that local variations in the frictional strength *are* important: the three measurement points with the highest stress ratios were all taken in the same location, which is most easily explained by inhomogeneity of the frictional strength.

The other striking difference between my results and experiments is in the values of v_{crack}. In the experiments there is a large number of points with $v_{\text{crack}} < 200$ m/s, the slow fronts. I have not observed the slow fronts in my simulations. I believe that the slow fronts are due to some physical process(es) that has(have) not been included in the model, i.e. the contact law would have to be changed or extended (in a more fundamental manner than just including a disorder in the friction coefficients) in order to produce them.

That I observe $v_{\text{crack}} > 3000$ m/s is easily explained. The loading zone has a physical extension, and within this zone, nodes are typically close to their static friction threshold when events nucleate, giving quick triggering. Indeed, the highest velocities

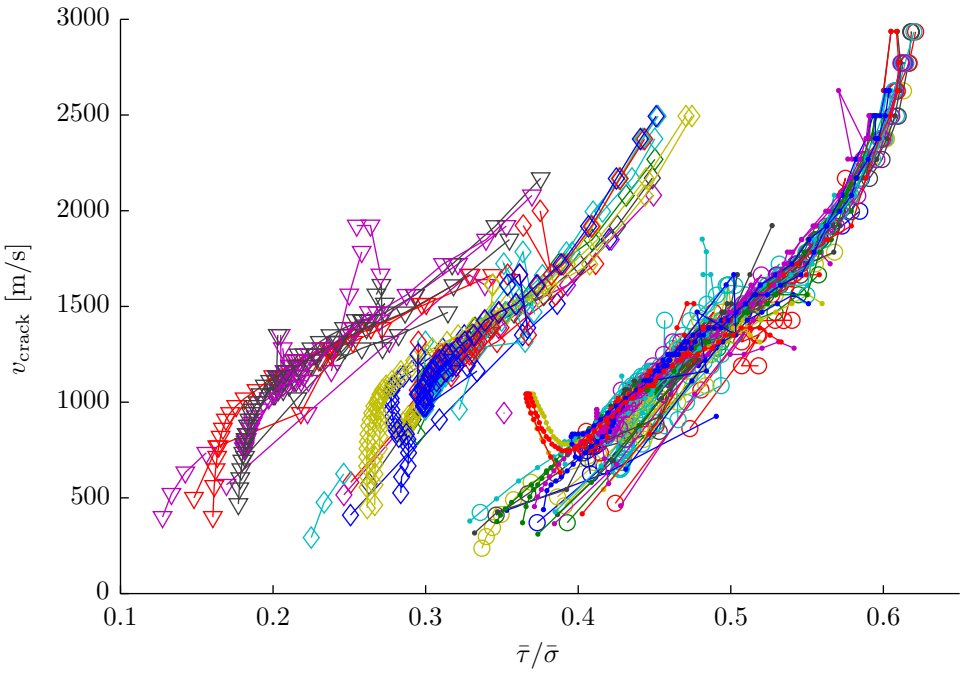

(a) Rupture front velocity as a function of shear to normal stress ratio.

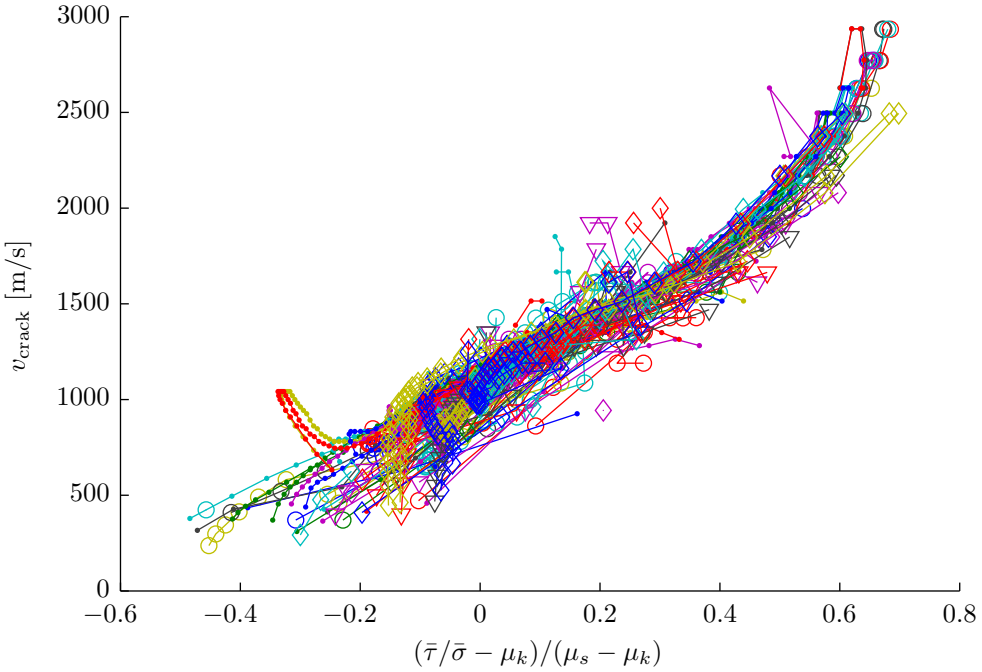

(b) Using $\tilde{\tau}$ on the abscicca collapses the data in (a).

Figure 5.31: The non-trivial parameter $\tilde{\tau}$ produces data collapse of simulations with different μ_k, μ_s. Shown are $L = 140$ mm, $F_Z = 3.5$ kN: i) $h = 5$ mm, $\mu_k = 0.20$, $\mu_s = 0.50$ ($\triangledown$); ii) $h = 5$ mm, $\mu_k = 0.30$, $\mu_s = 0.55$ ($\Diamond$); iii) $h = 7.5$ mm, $\mu_k = 0.45$, $\mu_s = 0.7$ ($\circ$); and iv) $L = 200$ mm, $F_Z = 2.7$ kN, $h = 10$ mm, $\mu_k = 0.45$, $\mu_s = 0.7$ ($\cdot$). All have $N_z = 31$, $k_{\text{ps}} = k$ and $\Delta t = 2 \cdot 10^{-7}$ s. Remaining parameters can be found in Table 5.1.

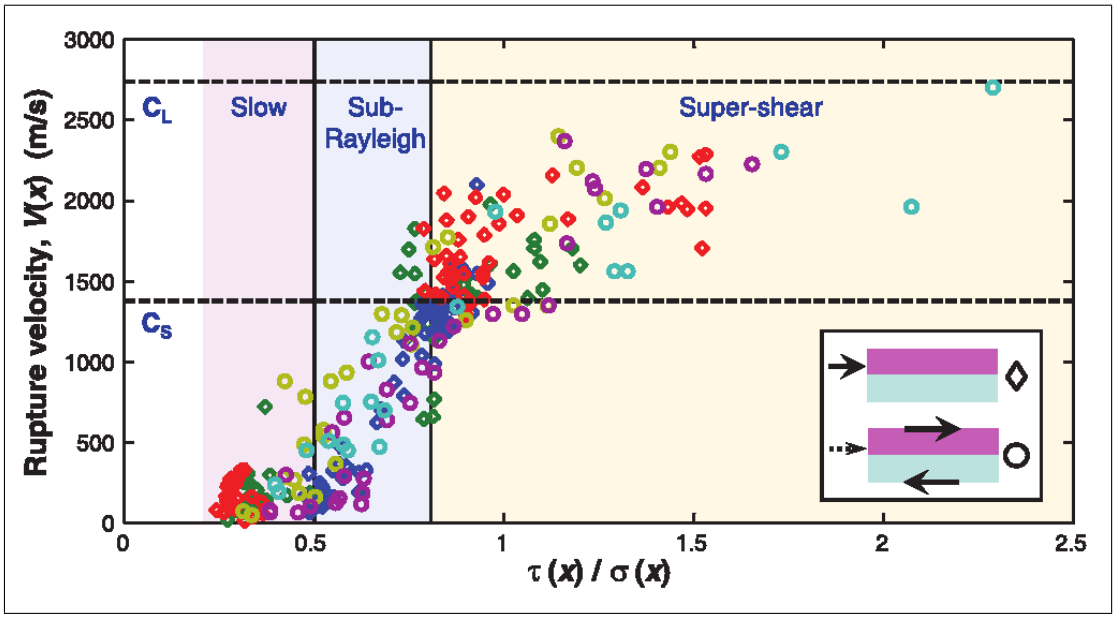

Figure 5.32: The same as Figure 3.10. $V(x)$ is my $v_{\text{crack}}(x)$, the crack front velocity, here presented for 287 different system-sized slip fronts. Shear was applied at the edge (diamonds) or predominantly uniformly (circles). Measurements were performed at strain gauge rosettes located away from the edges of the $L = 200$ mm sample. Dashed lines indicate longitudinal (C_L) and shear (C_S) wave speeds. Taken from Ben-David et al. [7].

in Figure 5.29 occur at the start of the events, i.e. in the vicinity of the nucleation point, which is most often the trailing edge. In the experiments, however, all the readings were taken away from the edges, to avoid the effects of large stress gradients ([7]).

Chapter 6

Results for slip weakening friction

The Amontons–Coulomb friction laws introduced in Section 2.1.1 predict a discontinuity in the friction force at the onset of sliding: upon reaching the static friction threshold, friction immediately drops to its dynamic value. Obviously, this approximation is not valid at all time and length scales. In the asperity picture, an infinitesimal movement cannot give a large change in the friction force. Perhaps the simplest refinement is to keep the static and dynamic friction description, but to smoothen out the transition between the coefficients by introducing a characteristic *length*, *velocity* or *time*. The two former are widely used in the literature, see e.g. [20, 28].

6.1 Slip weakening friction laws

A friction law that involves a characteristic length ξ_μ can for instance take the form

$$\mu = \mu_k + (\mu_s - \mu_k)e^{-|x-x_0|/\xi_\mu}, \tag{6.1}$$

x_0 being the position of the block at the onset of sliding. (While the block is at rest, $x = x_0$ and $\mu = \mu_s$.) A linear decrease

$$\mu = \begin{cases} \mu_s - (\mu_s - \mu_k)\frac{|x-x_0|}{\xi_\mu}, & |x - x_0| \leq \xi_\mu \\ \mu_k, & |x - x_0| > \xi_\mu \end{cases} \tag{6.2}$$

is equally justified. Figure 6.1 show these two laws graphically.

Both are based on the idea that microscopically, the population of junctions is the same at the onset of friction as immediately before, but is then renewed gradually as old junctions are ruptured and new ones are formed. The decrease in frictional resistance as this happens can be explained by ageing: the new junctions are younger and therefore weaker than the ones existing before the onset of sliding. However, the microscopic picture is not my point of interest, and the friction law including a transition between the friction coefficients can also be seen simply as a mathematical means of checking the robustness of my results when moving away from the singularity at $\xi_\mu = 0$.

6.2 Stick–slip and steady sliding under slip weakening friction

In Appendix B.1 I show that for a single block being pushed through coupling to a spring, Amontons–Coulomb friction gives stick–slip motion for all parameter values.

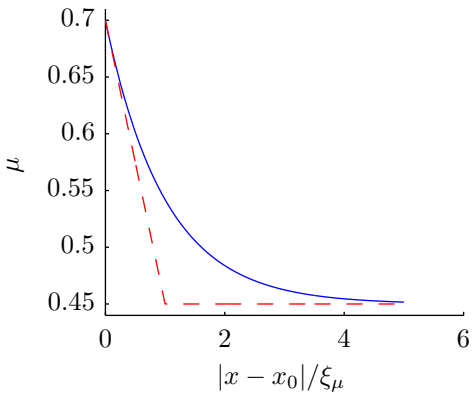

Figure 6.1: Slip weakening friction laws. The blue drawn line is equation (6.1), the red dashed line is (6.2). $\mu_s = 0.7$, $\mu_k = 0.45$.

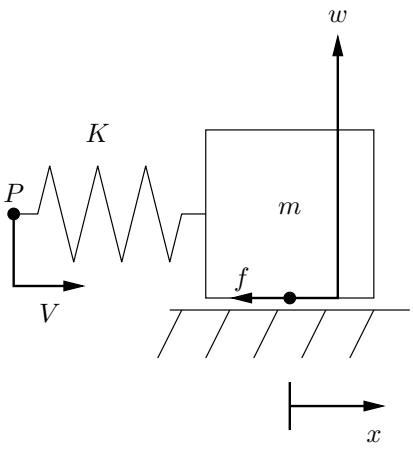

Figure 6.2: A sliding system consisting of a single block and a driving spring.

Here I will show that for the slip weakening friction introduced in Section 6.1, both stick–slip and steady sliding are possible depending on the steepness of the transition in the friction force and on K. For multi-block systems like the 1D and 1+1D models, there is a transitional regime where stick–slip vanishes in the initial loading phase. The argument is adapted from Scholz [52], pages 81–82.

The single block system is shown in Figure 6.2. For the purpose of stability analysis the movement of the point P during a small slip of the block, $\Delta x = |x - x_0|$, can be neglected. The change in the driving force is $\Delta F_X = -K\Delta x$, with slope $-K$. If the reduction of friction because of this small slip is greater than the reduction in the driving force, motion is unstable: a small positive slip takes the system to a point with positive acceleration. This produces stick–slip. If, on the other hand, the driving force changes faster than the friction, motion is stable: a small positive slip takes the system to a point of negative acceleration. Figure 6.3 shows the former case.

The friction force is $f = \mu w$. With μ given by equation (6.1) or (6.2),

$$\left.\frac{\mathrm{d}f}{\mathrm{d}x}\right|_{x_0} = -\frac{w(\mu_s - \mu_k)}{\xi_\mu} \tag{6.3}$$

and the condition for stick–slip becomes

$$\xi_\mu < \frac{w(\mu_s - \mu_k)}{K}. \tag{6.4}$$

Extending the analysis to the side driven 1D model is straightforward. Neglecting the motion of the neighbouring blocks the only difference in the argument is that K is

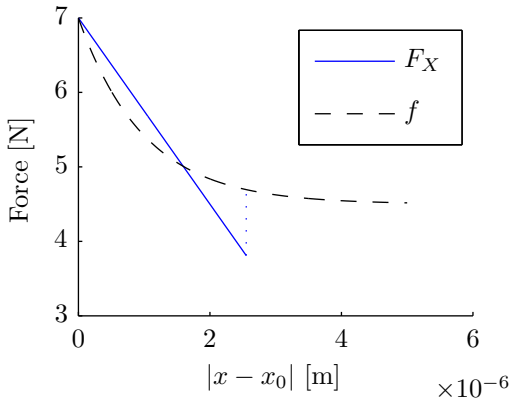

Figure 6.3: If the friction force falls off faster than the driving force, motion will be unstable. $\mu_s = 0.7$, $\mu_k = 0.45$, $w = 10$ N, $\xi_\mu = 1$ µm, $K = 1.25 \cdot 10^6$ N/m. The blue dotted line indicates the point where the integrals under the two curves (from the origin) become equal; neglecting V, this is the point where sliding stops.

replaced by

$$k_{\text{effective},i} = \begin{cases} k + K, & i = 1 \\ 2k, & i = 2, \ldots N - 1 \\ k, & i = N. \end{cases} \tag{6.5}$$

For $K < k$, the critical ξ_μ that makes stick–slip vanish will be determined by the leftmost block. Because $k \propto N$ and $w \propto 1/N$, $\xi_{\mu,\text{critical}}$ will be strongly resolution dependent, as verified by Table 6.1. I believe that the discrepancies between the theoretical predictions and the simulation results are due to multi-block instabilities. Even if the leftmost block is stable when considered on its own, once the next block starts moving the motion may become unstable, and indeed, Table 6.1 indicates that $\xi_{\mu,\text{critical}}$ is somewhat larger than the predicted values.

Determining $\xi_{\mu,\text{critical}}$ in the 1+1D model is harder, because multi-block instabilities seem to become more important. If the single block analysis *did* apply, $\xi_{\mu,\text{critical}}$ would be inversely proportional to the system resolution; doubling the number of nodes in each direction would halve the value of $\xi_{\mu,\text{critical}}$. This follows from equation (6.4) and the fact that in the 1+1D model, k is independent of resolution while on average, $w = F_Z/N_x$. However, Table 6.1 shows that the resolution dependence is much weaker than this.

The loading zone is the region at the trailing edge in which the shear force changes significantly during the loading between events, shown in Figure 6.4. As a first attempt to include multi-block instabilities in the analysis, I have considered the loading zone as a whole to be a single block. Since k is resolution independent, one can imagine coarsening the grid by grouping neighbouring blocks together. The normal load on the loading zone is, to first approximation, $w_{\text{lz}} = \frac{2h}{L} F_Z$, where I have assumed the extent of the loading zone to be twice the pushing height and neglected boundary effects in the normal force. The effective spring constant in the coarsened grid is $\frac{5}{4}k$, see Appendix B.4. With these assumptions,

$$\xi_{\mu,\text{critical}} = \frac{\frac{2hF_Z}{L}(\mu_s - \mu_k)}{\left(K + \frac{5}{4}k\right)}, \tag{6.6}$$

which has the right order of magnitude. More importantly, this predicts resolution independence. Table 6.1 shows resolution dependence, but one should remember that the systems I have been able to simulate are rather small. With $N_z = 16$, $h = \frac{1}{15}H$ means that the pushing point is only one node above the interface. It is not unreasonable

	$N = 50$	$N = 100$
Theory	1.6	0.4
Simulation	1.8–2	0.45–0.5

(a) 1D, $\xi_{\mu,\text{critical}}$ in units of 10^{-8} m. $\Delta t = 10^{-7}$ s, remaining parameters as in Table 4.1.

h/H	Theory	$N_z = 16$	$N_z = 31$	$N_z = 61$
0	1.4 , 0.7 , 0.4	1.2–1.4	0.8–1	
1/15	3	3–4	3–4	
2/15	6	5.5–6	4.5–5	3.5–4

(b) 1+1D, $\xi_{\mu,\text{critical}}$ in units of 10^{-6} m. The three values for $h = 0$ are the theoretical predictions for the different N_z, which are different because the loading zone collapses to a single block for this pushing height. The theoretical values for $h/H > 0$ depend on the width defined for the loading zone, and could easily have been a factor of two higher/lower. $k_{\text{ps}} = k$, $\Delta t = 0.4$, 0.2 and 0.1 µs for $N_z = 16$, 31 and 61, respectively. Remaining parameters as II in Table 5.1. Top loading: spring mattress.

$F_Z = 1.75$ kN	2–2.5
$\mu_s = 0.9$	7.2–9
$L = 200$ mm	2.8–3.5

(c) 1+1D, $\xi_{\mu,\text{critical}}$ in units of 10^{-6} m. Results after changes in a single parameter at a time with respect to (b). $N_z = 31$, $h/H = 2/15$. For $L = 200$ mm, M follows III in Table 5.1, but $F_Z = 3.5$ kN as in II used in (b) was kept.

Table 6.1: $\xi_{\mu,\text{critical}}$ as determined by simulations (Figure 6.5) and theory. The measured values in (b) and (c) are in good agreement with equation 6.6.

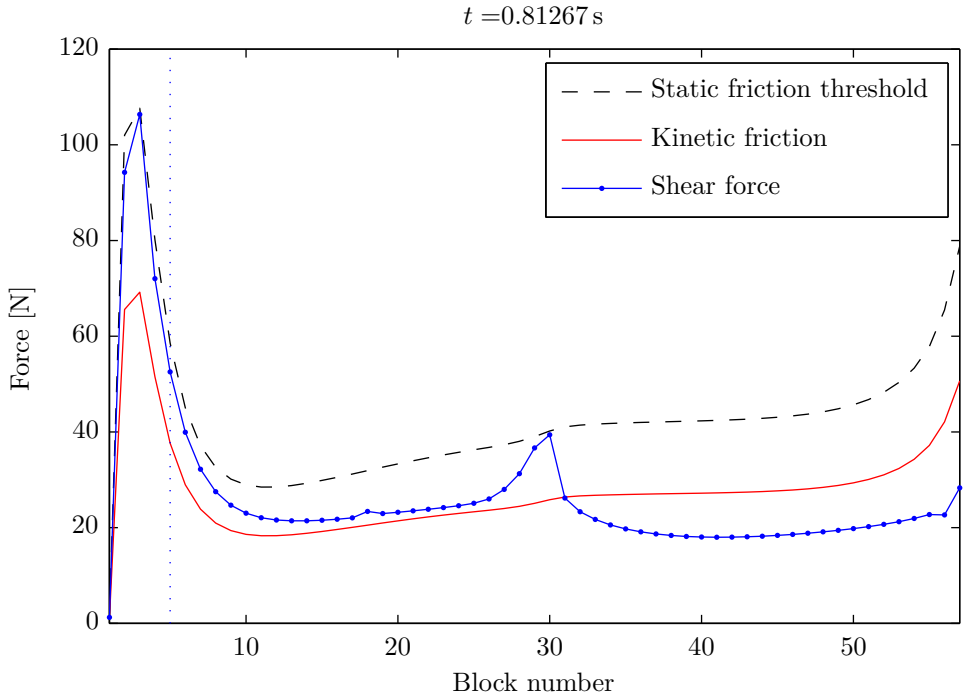

Figure 6.4: As in Figure 5.9, the loading zone is the region in which the shear and normal forces are significantly altered during the loading between events, i.e. the region to the left of the dashed line, which is located at $2h$. The edge of the loading zone is not uniquely defined, and the numerical factor in front of h is somewhat arbitrary. $N_x = 57$, $N_z = 31$, $\Delta\text{t} = 2 \cdot 10^{-7}$ s, $k_{\text{ps}} = k$, $\xi_\mu = 3 \cdot 10^{-6}$ m, $h = 5$ mm, remaining parameters as II in Table 5.1. Top loading: spring mattress.

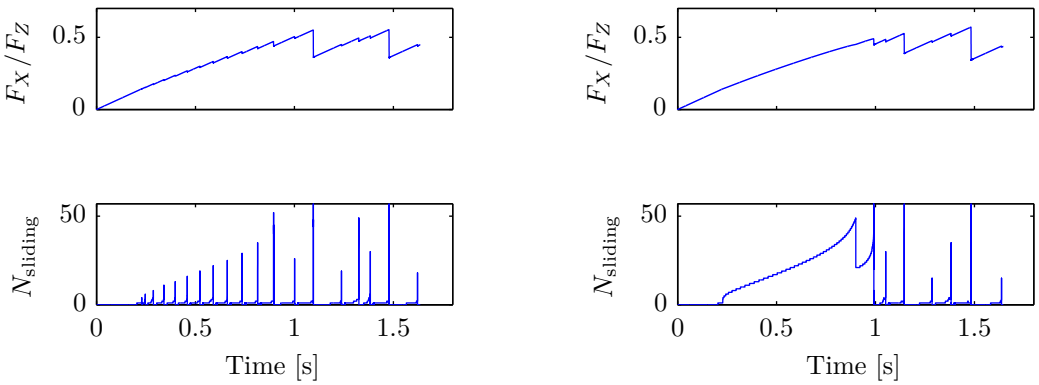

(a) $\xi_\mu = 3$ µm. **(b)** $\xi_\mu = 4$ µm.

Figure 6.5: The critical value of ξ_μ that makes stick–slip vanish can, for given parameters, be determined by simulations. In (a), multi-block instabilities are evident. At the start of each event, a few blocks start sliding one at a time. Then the point of instability is reached and the precursor obtains its final length in a small fraction of the event duration time. In (b), steady sliding occurs during the initial loading cycle. Instability can be observed after the first global event, but for studying the precursors, $\xi_\mu = 4$ µm is too high. Together, (a) and (b) show that $\xi_{\mu,\text{critical}}$ lies somewhere in the range 3–4 µm; this becomes the entry in Table 6.1. $N_z = 31$, $k_{\text{ps}} = k$, $\Delta t = 2 \cdot 10^{-7}$ s, remaining parameters as II in Table 5.1. Top loading: spring mattress.

to expect that for larger resolutions, $\xi_{\mu,\text{critical}}$ converges to a nonzero value. A qualitative argument in favour of this view follows.

The slip distribution at the onset of sliding at the leading edge should be resolution independent (Figure 6.6). For Amontons–Coulomb friction, the number of precursor events is resolution independent as long as $h > 0$ (Figure 5.10). Therefore, the local slip during each event must be resolution independent, at least as long as $\xi_\mu = 0$, and therefore so should $\xi_{\mu,\text{critical}}$ be.

6.3 Summary of findings

I find that replacing Amontons–Coulomb friction with a slip weakening friction law essentially leaves my results unchanged as long as $\xi_\mu < \xi_{\mu,\text{critical}}$. Although to be expected, this is not a trivial statement, because a discontinuous change from μ_s to μ_k gives a discontinuity in the force on a node at slip onset. Showing that my results are valid for more than the simplest friction law is important, because neither Amontons–Coulomb friction nor slip weakening friction are expected to reproduce the actual frictional response in the experiments.

Because a slip weakening law results in sliding events that begin by long-lasting sliding of a few nodes, see Figure 6.5a, my algorithm for reducing the amount of simulation data written to file must be refined in order to investingate v_{crack} under slip weakening friction. However, I expect that this, too, is essentially unchanged.

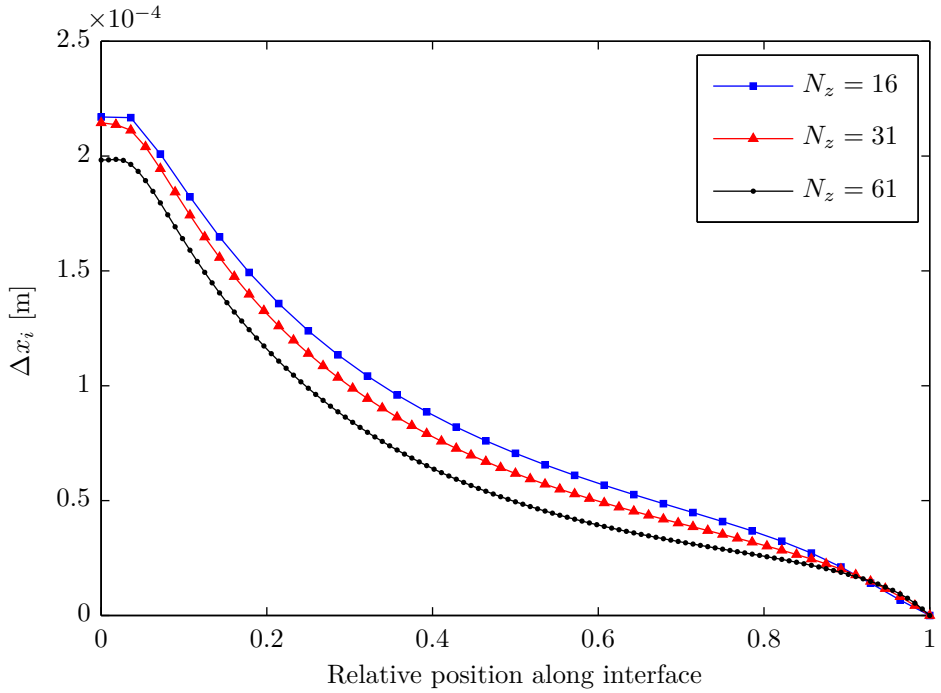

Figure 6.6: The slip $\Delta x_i = x_i(t) - x_i(0)$ along the interface at the instant at which the rightmost block starts moving, i.e. when the precursors reach the leading edge. The slip distribution depends only weakly on the system resolution. $k_{\mathrm{ps}} = k$, $\Delta t = 0.4$, 0.2 and 0.1 µs for $N_z = 16$, 31 and 61, respectively. Remaining parameters as II in Table 5.1. Top loading: spring mattress.

Part III

SUMMARY AND CONCLUSIONS

Chapter 7

Summary and conclusions

In Chapter 3 I presented recent experimental work that resolved the onset of sliding in space and time. The experiments were performed using two blocks of poly(methyl methacrylate) (PMMA), one acting as a base and the other as a slider. By measuring the details of the stepwise growth of the slipped region, the experiments went beyond the classical friction laws that consider a single degree of freedom, the velocity of the centre of mass. Existing theoretical/numerical works on multi degree of freedom models of friction either did not consider the onset of sliding, or else were unable to reproduce the experimental results satisfactorily. The goal of this thesis has been to study the onset of sliding in models of the minimum complexity required to significantly improve the agreement with experiments. This goal has been reached through the combined study of a 1D and a 1+1D spring–block system with complete time dynamics and local Amontons–Coulomb friction.

In this chapter I summarise my findings and the conclusions drawn from them.

7.1 Summary of findings

7.1.1 1D model

The 1D model was found to correctly predict a stepwise increase in the length of the slipped region, i.e. a series of precursors. As the external tangential load, applied at the trailing edge, was increased, local slip occurred while the leading edge remained pinned. This behaviour was inherent in the construction of the load transfer mechanism. The length L_p of successive precursors as a function of the driving force F_X was studied. For a given precursor length, the shear force profile was found to have the following characteristics: to the left of the precursor arrest point, the shear force equalled the dynamic friction level, while to the right of this point the local shear forces retained their values at the start of the experiment. These two observations enabled an analytical prediction of L_p–F_X that was found in excellent agreement with the numerical results.

The experimentally observed changes in the shape of L_p–F_X with changes in the normal load, that precursors are longer (shorter) for a given F_X when the normal load at the trailing edge is lower (higher), was reproduced qualitatively. The quantitative agreement with experiments, on the other hand, was poor. Including an initial shear force profile similar to the one in the experiments improved the agreement somewhat. The biggest discrepancy was the number of events, which scaled linearly with the system resolution N. This was explained by the fact that the loading zone in the 1D side driven

model consists of a single node.

In the top driven model a friction induced torque was modelled as an F_X dependent asymmetry in the normal force profile. This was seen to make the trailing edge the precursor nucleation point even with uniform shear loading. Comparison with the theoretical model of Scheibert and Dysthe revealed major deviations from their assumptions that can probably be attributed to the differences in the loading conditions: the relaxation of the driving force upon sliding was much less in my model, and local peaks in the shear force profile were shown to dominate the triggering of successive events.

The study of the 1D models gave experience with spring–block systems that helped identify interesting lines of investigation. The major shortcomings of the side driven 1D model, the resolution dependence of the loading zone and the need to impose the normal force profile directly, were overcome by introducing the 1+1D model.

7.1.2 1+1D model

The 1+1D model extended the 1D model by introducing the dimension out of the sliding plane. This had the important consequences that stress could be transferred through the bulk, and that boundary conditions could be made much more realistic. The normal force profile was no longer imposed directly, but resulted from global force balance between the external force pushing down and the track pushing up on the slider. Consequently, it could evolve dynamically, redistributing the local force/stress as slip events deformed the slider. The evolution of the normal force profile was found in accordance with experiment.

With the vertical dimension included in the model, the application height h of the external driving force could be varied systematically. A nonzero height was found to give the loading zone a physical extension of the order h, which made it resolution independent. In itself, this was a major improvement over the 1D model, because it made the number and amplitude of events robust to changes in resolution.

The L_p–F_X curves in the 1+1D model agreed very well with experiments, both in shape and in number of precursors. The change in the number of precursors with h and with changes in the friction coefficients was explained to first order by an estimate of the force change required to trigger each new precursor. Data collapse by rescaling with L and F_Z was demonstrated. Force transfer through the bulk invalidated the 1D result that the shear force remained unchanged to the right of the precursor arrest point. This made the analytical prediction scheme fail, but was one of the reasons for the improved agreement with experiment. The analytical prediction was replaced by a scheme with $\mu_s = \mu_k$ that I expect to work well in quasi-static calculations.

The rupture front velocities v_{crack} were studied and related to the local shear to normal stress ratio τ/σ at event initiation. Because numerical simulations provide complete access to all variables, I was able to study the evolution of each front as a function of τ/σ; in the experiments, the resolution in τ was too low to allow this. I found that for the present loading conditions, all events followed a similar curve in τ/σ–v_{crack} space. The shape of the curve was preserved upon changes in L and F_Z. A non-trivial variable that combined τ/σ, μ_s and μ_k was shown to provide data collapse for experiments with different friction coefficients. However, this master curve did not agree with the experimental master curve. The most striking discrepancies were a much too narrow interval of sampled τ/σ values, and the lack of slow fronts.

7.1.3 Results for slip weakening friction

The Amontons–Coulomb friction laws predict a discontinuity in the friction force at the onset of sliding. To check that my results are not artefacts of this discontinuity, I implemented a slip weakening friction law that smoothened the transition between the friction coefficients out over a characteristic length ξ_μ. As long as ξ_μ was less than a critical length $\xi_{\mu,\text{critical}}$, the measures I study were essentially unchanged. The value of $\xi_{\mu,\text{critical}}$ was found to depend on the normal load, the stiffness of the slider and driving stage, and the friction coefficients. In 1D $\xi_{\mu,\text{critical}}$ was strongly resolution dependent, while in 1+1D it was found to be weakly resolution dependent. An argument concluding that in 1+1D it should have a nonzero value regardless of resolution was presented.

7.2 Outstanding questions in the 1+1D model

In addition to the uses I have made of the 1+1D model, I believe that the following subjects would be valuable to pursue further.

a) *The importance of inertia.* Taking my parameters from specific experiments, I have not explored the parameter space of the model thoroughly. The effects of inertia and damping are coupled: no inertia means that blocks move to where they experience zero net force, which also happens for overcritical damping. On the other hand, overcritical damping means that movement takes a long time, which is more similar to high inertia. In addition to addressing the fundamental interest in knowing the importance of inertia in the model, exploring the effect of changes in damping and inertia magnitudes would likely reveal any unintentional effects of the artificial damping that has been introduced.

b) *Slip arrest.* The stress profiles at the start of each event are determined by the stopping of the previous event. A better understanding of how slip stops might help understand more quantitatively where and when slip will start.

c) *Sound velocities in 2D.* Experimentally, the rupture front velocities are compared to the transverse and longitudinal material sound speeds, see e.g. [7]. It is not obvious whether the rupture velocities in the model should be compared to the experimental sound speeds, to indicate the quantitative agreement, or to sound speeds in the model, to indicate a relative agreement. In order to use model sound speeds and understand how these relate to experimental sound speeds, you should consider the relation between the adiabatic elastic constants and the isothermal elastic constants of PMMA.

d) *Elasticity of the track.* The track was removed from the model system and replaced by a rigid potential for ease of implementation. In light of the importance of the boundary conditions on L_p–F_X it would be interesting to see if including the elasticity of the track improves the agreement further. However, apart from small quantitative changes to the results, I do not believe a priori that new insights will be gained by modelling the track.

e) *Uniform shear load.* So far, only side driving in a point has been studied in the 1+1D model. Investigating the behaviour under uniform shear load would help span the limits of what can be observed in this model.

f) *Slow fronts.* I have not observed the slow fronts, and from the range of sampled τ/σ alone it is clear that in order to reproduce the complete dynamics of the experiments, the local friction law must be modified. How this should be done remains an open question, but my results indicate that variations in the friction law have to be combined with models including the vertical dimension if real quantitative agreement is desired.

7.3 Relation to other modelling approaches

I have studied spring–block models in 1D and 1+1D. The springs and blocks are essentially a finite difference approximation to the elastic continuum. As discussed in Section 3.3, spring–block models of frictional systems have a long history in the earthquake community. The main difference from existing work is that I choose parameters similar to laboratory friction experiments, study the onset of sliding, and that I include the dimension out of the sliding plane.

I have been asked why I did not use the finite element method (FEM). The answer is twofold. Firstly, I wanted to begin by catching up with the research frontier, and the models of Braun et al. and Maegawa et al., the most recent I know that study sliding onset, are spring–block models. Secondly, development of FEM code usually takes more time than writing finite difference code. In order to have complete freedom and control over the assumptions in the model I wanted to write the programs myself instead of applying commercial or open-source packages. It was clear that I would be able to explore more model permutations with a spring–block approach. A FEM modelling approach should be considered in future work. Solving the equations of elasticity with FEM software is a mature field, and it is to be expected that the representation of the stress fields would improve. The importance of these fields has been demonstrated in the present work.

The present models only have two scales: the size of a single block, and the size of the whole slider. The smallest, the size of single block, has implicitly been assumed mesoscopic: a phenomenological friction law cannot be applied unless each block covers a statistical ensemble of asperities. In 1+1D I have used an internode spacing of $l \sim 1$ mm; in [45], the distance between contact points was estimated to be 10 µm. Clearly, if the resolution is much increased, a model that incorporates the response of single asperities should be considered. This would have profound interest, because it could yield a bottom-up estimate of the global frictional properties. The response of single asperities could come from molecular dynamics simulations, where the building blocks are individual molecules. With molecular dimensions generically of order nanometres, it should be possible to build asperities on the order of micrometres.

7.4 Conclusions

The shear and normal force profiles and the L_p–F_X curves are part of what I have called the statics of the onset of sliding. The statics are tied to the "frozen" states of the sliding system: the configurations it comes to rest in. The rupture front velocities exemplify what I have called the dynamics of the onset of sliding; the velocities depend on the detailed time evolution. A priori, I expected that the statics and the dynamics were tightly coupled: that either one could not be studied without the other. My results indicate that this is not the case. The statics were reproduced remarkably well,

considering the simplicity of the applied friction law, while the dynamics still lacked important features of the experimental results. Apparently, the statics can be studied without a complete understanding of the dynamics. The converse is not true: the strong dependence of v_{crack} on τ/σ shows that without a proper representation of the statics, it is unlikely that the experimental dynamics can be reproduced.

Some of the questions listed in Section 3.4 have been answered. To predict the shape of L_p–F_X and the number of precursors in an experiment, the vertical dimension must be included in your model, and you should try to mimic the external loading conditions. You do not, seemingly, need an accurate friction law or a correct representation of the dynamics.

The local speed of a rupture front is determined by the prestress τ and the frictional strength before and after passage of the front. In the Amontons–Coulomb formulation, the crucial parameter is $\tilde{\tau} = \frac{\tau/\sigma - \mu_k}{\mu_s - \mu_k}$, where σ is the normal stress. Thus, a front slows down when it reaches a region of low prestress, and speeds up when it reaches a region of higher prestress. However, this is not the complete picture, as I have been unable to reproduce the slow fronts seen in the experiments.

The limiting value of the local shear to normal stress ratio τ/σ is the local static friction threshold, which, unsurprisingly, is lower than the global static friction threshold. I have used a single static friction coefficient μ_s, but it would be interesting to see if introducing disorder in the local frictional strength could produce high τ/σ values without dramatically changing the static results.

The questions of how to use the event history of the interface to predict and control the magnitude of the next event remains open.

Although all the experiments to which I have compared my results were carried out with PMMA on PMMA, I believe that the main insights, that the vertical dimension cannot be ignored if quantitative agreement is desired, and that the statics can be reproduced independently of the dynamics, have a more general validity: save for the values of the mass density and the elastic constants, the models describe a generic elastic material.

7.5 Outlook

Of the questions in Section 2.4, the one of most interest outside the community of tribologists and other scientists studying friction is very likely how friction can be controlled in practice. However, finding profound answers to this question is probably tied to answering the more academic questions.

Reaching a level of sophistication where the parameters in the phenomenological relationships can be predicted from first principles or molecular dynamics would be a great stride in the understanding of friction. It would mean that new surface textures and coatings, and new lubricants, could be investigated in computer simulations, where analysis can benefit from complete access to all variables. Novel microstructuring or lubricant compositions could more easily be explored.

Meanwhile, the miniaturisation of computer hardware, medical equipment and other machines brings us ever closer to the atomic level, where surface interactions take on new descriptions and importance as the contacts become too few for statistical averaging and the volume to area ratio shrinks. It can be hoped that a better understanding of the microscopic origins of friction can lead to improvements on the macroscale too.

Part IV

APPENDICES

Appendix A

Numerical solution of the equations of motion

Numerical techniques for solving differential equations is a vast subject and a research field in its own right. Consequently, choosing an appropriate solution method for the problem at hand from the plethora of available methods can seem like a daunting task. An exhaustive treatment is probably beyond the scope of any work; it is certainly beyond the scope of this thesis. Luckily, once the type of equations and boundary conditions have been identified, one is down to a manageable number of applicable schemes.

In this appendix I will first cover some of the general ideas that are common to most applications. I will then focus on the method that I have employed in my work: the fourth order Runge–Kutta (RK4) integration on a uniform temporal grid. Good references are Langtangen [35] and Press et al. [44].

A.1 Classification of problems involving differential equations

Classification of problems involving differential equations is important because it helps determine the applicable numerical solution techniques in each case. To classify a given problem, one must consider both the form of the equation and the boundary conditions.

An equation that contains functions of only one independent variable and derivatives with respect to that variable is called an ordinary differential equation (ODE). The equation of a single point undergoing simple harmonic motion,

$$m\frac{\mathrm{d}^2u(t)}{\mathrm{d}t^2} + ku(t) = 0 \tag{A.1}$$

with m and k as constants, is an ODE: it has one independent variable t and one dependent variable $u(t)$.

An equation involving functions of more than one independent variable and partial derivatives with respect to these variables is called a partial differential equation (PDE). The wave equation

$$\frac{\partial^2u(x,t)}{\partial t^2} = \gamma^2\frac{\partial^2u(x,t)}{\partial x^2} \tag{A.2}$$

with γ as a constant is a PDE. If x is position in space and t is time then $u(x,t)$ can e.g. be the shape of a string. In this example x and t are independent variables and $u(x,t)$ is the dependent variable.

The solution of a differential equation is not determined by the equation alone: boundary conditions are needed. Nevertheless, in analytical calculations the solution method is often independent of the boundary conditions, which are treated at the end by determination of unknown constants that appear in the solutions. In numerical work, however, classifying the boundary conditions is an important part of determining which method to use.

Boundary conditions are conditions on the values of the unknown functions prescribed at the boundary of the region of interest (e.g. some interval). They can be simple requirements on the value of certain variables at given discrete points, or more complicated relations between the variables. Boundary conditions divide into two broad categories.

- In *initial value problems* all the boundary conditions are given at the same point, which becomes the starting point of the solution scheme. This is often the case when the equations describe some time evolution. The task is to track the time evolution with some desired accuracy.

- In *boundary value problems*, boundary conditions are specified at more than one point. There is no obvious point to "start" and the task becomes the usually more complicated one of finding solutions that satisfy all the boundary conditions.

The problems I study in this thesis are initial value problems of (coupled) ordinary differential equations. I will now introduce the Runge-Kutta method for solving such problems.

A.2 Runge–Kutta integration

The fundamental idea behind Runge–Kutta integration and similar methods is to obtain the full solution by tracking the evolution of the unknown functions as the independent variable changes from some starting point where the unknowns are given by the boundary conditions. This is achieved by introducing discrete steps in the independent variable. The simplest example is solving the first-order equation

$$\frac{\mathrm{d}x(t)}{\mathrm{d}t} = f(t, x(t)) \tag{A.3}$$

by Euler's method. Formally, the derivative is replaced by the definition

$$\frac{\mathrm{d}x(t)}{\mathrm{d}t} = \frac{x(t+\Delta t) - x(t)}{\Delta t}, \tag{A.4}$$

but instead of taking the limit $\Delta t \to 0$, this step size is assigned a non-zero value. As $x(t)$ is known for some value $x(t_0)$ from the boundary conditions, one can then take steps forward in time to find

$$x(t_1) = x(t_0 + \Delta t) = x(t_0) + \Delta t f(t_0, x(t_0)), \tag{A.5}$$

from which $x(t_2) = x(t_1 + \Delta t)$ can be found, and so on.

One of the problems with Euler's method is that the error in equation A.5 is of order $(\Delta t)^2$ (usually written as $O(\Delta t^2)$), as can be seen from a Taylor series expansion. To increase the accuracy of the solution one can decrease the step size Δt. A better idea

in terms of computational efficiency is to use a slightly more elaborate method in which the error is of higher order.

The standard way of deriving the fourth-order Runge–Kutta method is to introduce intermediate steps to the midpoint of the integration interval, i.e. to use $\Delta t/2$. By combining Euler-like steps with different coefficients in front of the higher order error terms in clever ways, one can make the error terms cancel. To achieve $O(\Delta t^5)$ requires three intermediate steps and four evaluations of the right hand side $f(t, x(t))$: two steps to the midpoint and one step to the endpoint, and an evaluation of the right hand side at this trial endpoint. Introducing the notation $x(t_i) = x_i$ and writing each Euler step as $x_{i+1} = x_i + \Delta t f(t_i, x_i)$, the algorithm for the fourth-order Runge–Kutta method is

$$\boxed{\begin{aligned} k_1 &= \Delta t f\left(t_i, x_i\right) \\ k_2 &= \Delta t f\left(t_{i+1/2}, x_i + k_1/2\right) \\ k_3 &= \Delta t f\left(t_{i+1/2}, x_i + k_2/2\right) \\ k_4 &= \Delta t f\left(t_{i+1}, x_i + k_3\right) \\ x_{i+1} &= x_i + \frac{1}{6}\left(k_1 + 2k_2 + 2k_3 + k_4\right) + O(\Delta t^5). \end{aligned}} \tag{A.6}$$

Compared to Euler's method and other lower order methods, each step in the RK4 method is computationally more expensive, because of the additional right hand side evaluations. In common applications, this is offset by giving the same overall accuracy with a larger step size Δt, so that the total number of $f(t, x)$ evaluations becomes smaller.

A.3 Coupled differential equations

Coupled first-order differential equations for the functions $x_i(t)$, $i = 0, 1, \ldots, N-1$ take the general form

$$\frac{\mathrm{d}x_i(t)}{\mathrm{d}t} = f_i(t, x_0, \ldots, x_{N-1}), \qquad i = 0, \ldots, N-1. \tag{A.7}$$

The subscript i denotes different functions, and should not be confused with the shorthand notation $x_i = x(t_i)$ for the value of the single unknown function x at the time step $t_i = t_0 + i\Delta t$ of the previous paragraphs. Extending the integration scheme to coupled equations is trivial: for each step in time, including trial time steps, apply the scheme to each equation separately. The right-hand sides will take care of the coupling.

Another powerful result is that problems involving ODEs can always be reduced to the study of coupled first-order equations. As an example, the second-order equation

$$\frac{\mathrm{d}^2x}{\mathrm{d}t^2} = \frac{1}{m}F\left(t, x, \frac{\mathrm{d}x}{\mathrm{d}t}\right), \tag{A.8}$$

where m typically denotes a particle mass and F is the sum of forces on this particle, can be reduced to two coupled equations by introducing the velocity $v = \mathrm{d}x/\mathrm{d}t$, giving

$$\frac{\mathrm{d}v}{\mathrm{d}t} = \frac{1}{m}F\left(t, x, v\right) \tag{A.9}$$

$$\frac{\mathrm{d}x}{\mathrm{d}t} = v. \tag{A.10}$$

Newton's second law for N interacting particles thus typically results in $2N$ coupled first-order equations. As mentioned above, Runge–Kutta integration of each equation solves them all simultaneously.

Appendix B

Supporting analytical solutions

B.1 Periodic stick–slip of a single block under Amontons–Coulomb friction

Figure B.1 depicts a sliding system consisting of a single block of mass m under normal load w driven by coupling to a moving point P through a spring of stiffness K. When performing experiments on such sliding systems one can distinguish the three kinds of sliding dynamics shown in Figure 2.3: steady sliding, periodic stick–slip motion and chaotic motion. Stick–slip occurs for low values of K and V only (Persson [43]).

Surprisingly, Hooke's law for the spring and the Amontons–Coulomb laws for friction are unable to predict a steady sliding regime for this system when the transition from static to dynamic friction is assumed to be instantaneous, as is typically the case in physics textbooks.

At time $t = 0$ the block is at rest and the spring is in its equilibrium configuration. As the point P moves to the right, the increasing force from the spring on the block is cancelled exactly by static friction. This holds until the force from the spring reaches the static friction threshold at

$$t_0 = \frac{\mu_s w}{KV}. \tag{B.1}$$

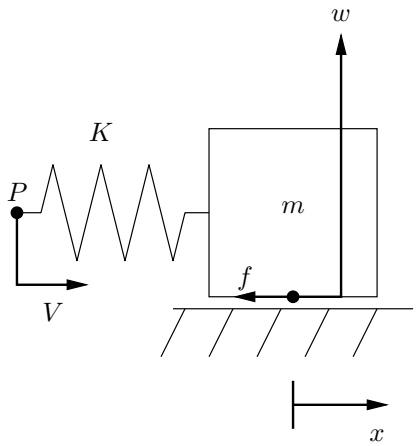

Figure B.1: A sliding system consisting of a single block and a driving spring.

At this point in time the block starts sliding, and the equation of motion becomes

$$m\ddot{x} = K(Vt - x) - \mu_k w \tag{B.2}$$
$$\tag{B.3}$$

until the block stops moving. Introducing $\omega = \sqrt{K/m}$ this can be rewritten as

$$\ddot{x} + \omega^2 x = \omega^2 V t - \frac{\mu_k w}{m}. \tag{B.4}$$

The general solution of the homogeneous left-hand side is $x_{\text{hom}}(t) = C\sin(\omega t + \phi)$, where the constants C and ϕ can be determined by the initial conditions $x(t_0) = 0$, $\dot{x}(t_0) = 0$. A particular solution of the inhomogeneous equation is $x_{\text{part}}(t) = Vt - \mu_k w/(m\omega^2)$. The general solution is

$$x(t) = x_{\text{hom}}(t) + x_{\text{part}}(t) \tag{B.5}$$
$$= C\sin(\omega t + \phi) + Vt - \frac{\mu_k w}{m\omega^2}. \tag{B.6}$$

The initial conditions become

$$0 = x(t_0) = C\sin(\omega t_0 + \phi) + \frac{w}{K}(\mu_s - \mu_k) \tag{B.7}$$
$$0 = \dot{x}(t_0) = \omega C\cos(\omega t_0 + \phi) + V. \tag{B.8}$$

Solving for C and ϕ is not necessary except to note that neither depends on t.

A necessary condition for steady sliding is that $\dot{x}(t)$ remains positive for all $t > t_0$. As soon as the block stops sliding it is back to static friction and the motion will repeat itself (chaotic motion in this single block model would require modelling of surface inhomogeneities, e.g. by making μ_s and μ_k x dependent). Since C and ϕ are determined such that (B.8) is fulfilled,

$$\dot{x}(t) = \omega C\cos(\omega t + \phi) + V \tag{B.9}$$
$$= 0 \tag{B.10}$$

at $t = (t_0 + 2\pi/\omega)$ at the latest, which shows that no values of K and V will give steady sliding in this model.

B.2 The harmonic oscillator

To introduce the concept of damping regimes it is convenient to start out with a single block only.

Consider a block of mass m connected to an ideal spring of stiffness k that is attached to a rigid wall. Assume for now that the block slides without friction. If the position of the block is taken to be $x = 0$ at the point where the spring has its equilibrium length, the equation of motion for the block is

$$m\ddot{x} + kx = 0, \tag{B.11}$$

which has the solutions

$$x(t) = A_{\pm} e^{\pm i\omega_0 t}, \tag{B.12}$$

where $\omega_0 = \sqrt{k/m}$ and it is understood that only the real part of the solutions have physical significance. This is called simple harmonic motion.

Damped harmonic motion occurs if there is an additional force resisting the motion of the block, e.g. viscous damping of the form $F_\eta = -\eta\dot{x}$. With this term the equation of motion becomes

$$\begin{aligned} 0 &= m\ddot{x} + \eta\dot{x} + kx \\ &= \ddot{x} + \frac{\eta}{m}\dot{x} + \omega_0 x. \end{aligned} \tag{B.13}$$

This linear ordinary differential equation can be solved by using the characteristic polynomial, or one can simply make the ansatz

$$x(t) = e^{-\alpha t} e^{i\omega t} = e^{(-\alpha + i\omega)t}. \tag{B.14}$$

There is of course a solution with $-i\omega t$ as well, and the general solution will be a superposition of the two. Inserting (B.14) in (B.13) one finds that

$$\alpha = \frac{\eta}{2m}, \tag{B.15}$$

$$\omega^2 = \frac{k}{m} - \frac{\eta^2}{4m^2}. \tag{B.16}$$

As long as ω is real the system oscillates; it is underdamped. For $\eta = 0$ the undamped solution is recovered and $\omega = \omega_0$. The period increases with η until critical damping occurs at

$$\eta = 2\sqrt{km}, \tag{B.17}$$

$$\omega = 0. \tag{B.18}$$

With this value of the damping coefficient, the system does not oscillate, but returns exponentially to its equilibrium configuration of $x = 0$. For larger values of η the system is overcritically damped and the decay is slower.

B.3 The one-dimensional monatomic chain

Extending the treatment of the previous section to a one-dimensional chain of blocks and springs is a standard way of introducing vibrations of crystals, see e.g. [26] by Elliott. Without the damping term one finds the dispersion relation

$$\omega_\kappa = 2\sqrt{\frac{k}{m}}\left|\sin\left(\frac{\kappa a}{2}\right)\right|, \tag{B.19}$$

where a is the lattice spacing and κ is the wave vector or mode. The angular frequency takes its maximum value $2\sqrt{k/m}$, called the cut-off frequency, at $\kappa = \pi/a$, which corresponds to the shortest possible wavelength on the grid, $\lambda = 2a$. In this mode, alternating blocks oscillate in opposite directions. As it turns out, the friction models I will study tend to excite high-frequency modes. This is unfortunate, as it implies a strong dependence on the grid resolution of physical quantities like the stress field.

Different ways of damping these oscillations can be envisaged, sliding friction itself being among them. Following Knopoff and Ni [33] I have included in my 1D model a viscous damping term on the relative motion of the blocks,

$$\eta\frac{\mathrm{d}(x_{j+1} - x_j)}{\mathrm{d}t}, \tag{B.20}$$

where x_j is the position of block j and η is a damping coefficient whose value will be chosen such that oscillations are underdamped.

If there are no external forces, the equation of motion for the jth block is

$$m\ddot{x}_j = k\left(x_{j+1} - 2x_j + x_{j-1}\right) + \eta\left(\dot{x}_{j+1} - 2\dot{x}_j + \dot{x}_{j-1}\right). \tag{B.21}$$

A trial solution is

$$x_j(t) = e^{i(\kappa ja - \omega_\kappa t)}e^{-\alpha_\kappa t} \tag{B.22}$$

$$= e^{i\kappa ja}e^{-(\alpha_\kappa + i\omega_\kappa)t}, \tag{B.23}$$

with α_κ as a positive constant to be determined. Inserting this trial solution in (B.21) gives

$$m\alpha_\kappa^2 + 2im\alpha_\kappa\omega_\kappa - m\omega_\kappa^2 = k\left(e^{i\kappa a} - 2 + e^{-i\kappa a}\right) - (\alpha_\kappa + i\omega_\kappa)\eta\left(e^{i\kappa a} - 2 + e^{-i\kappa a}\right). \tag{B.24}$$

As

$$e^{i\kappa a} - 2 + e^{-i\kappa a} = \left(e^{i\kappa a/2} - e^{-i\kappa a/2}\right)^2 \tag{B.25}$$

$$= \left(2i\sin\left(\frac{\kappa a}{2}\right)\right)^2 \tag{B.26}$$

$$= -4\sin^2\left(\frac{\kappa a}{2}\right) \tag{B.27}$$

the real and imaginary parts of (B.24) are easily separated. They are

$$m\alpha_\kappa^2 - m\omega_\kappa^2 = -4(k - \eta\alpha_\kappa)\sin^2\left(\frac{\kappa a}{2}\right), \tag{B.28}$$

$$2im\alpha_\kappa\omega_\kappa = 4i\eta\omega_\kappa\sin^2\left(\frac{\kappa a}{2}\right), \tag{B.29}$$

which give

$$\alpha_\kappa = 2\frac{\eta}{m}\sin^2\left(\frac{\kappa a}{2}\right), \tag{B.30}$$

$$\omega_\kappa^2 = 4\sin^2\left(\frac{\kappa a}{2}\right)\left(\frac{k}{m} - \frac{\eta^2}{m^2}\sin^2\left(\frac{\kappa a}{2}\right)\right). \tag{B.31}$$

The shortest possible wavelength on the grid is $\lambda = 2a$, which corresponds to

$$\kappa = \frac{2\pi}{\lambda} = \frac{\pi}{a}. \tag{B.32}$$

In the undamped system ($\eta = 0$) this has the cut-off frequency. This mode is critically damped when $\omega_{\text{cut-off}} = 0$, which means

$$\eta = \sqrt{km}. \tag{B.33}$$

It is also the mode which is critically damped for the lowest value of η, making it a suitable candidate for choosing η. I introduced the viscous damping to get rid of oscillations, but I want to minimise the effect on other parts of the dynamics. Critical or overcritical damping will remove oscillations completely, an unwanted consequence, while too small an η will not remove oscillations satisfactorily. Some trade-off has to be made and η is not determined completely by this analysis. I have followed Knopoff and Ni, who suggest using the value

$$\frac{\eta}{\sqrt{km}} = \sqrt{0.1}. \tag{B.34}$$

B.4 Effective stiffness at a corner in 1+1D

In Section 6.2 I use the effective stiffness at the lower left corner of the 1+1D lattice. Here I derive it by calculating the net force on the lower left block if it is displaced a small distance.

In Figure B.2 the forces on block 1 from the other three blocks if these are assumed stationary and block 1 is displaced a small distance Δx to the right are

$$F_{12,x} = -k\Delta x, \tag{B.35}$$

$$F_{13,x} = -k\left(r_{13} - l\right)\frac{\Delta x}{r_{13}}, \qquad r_{13} = \sqrt{l^2 + \Delta x^2} \approx l + \frac{\Delta x^2}{2l}, \tag{B.36}$$

$$= 0, \tag{B.37}$$

$$F_{14,x} = \frac{k}{2}\left(r_{14} - \sqrt{2}l\right)\frac{l - \Delta x}{r_{14}}, \qquad r_{14} = \sqrt{(l - \Delta x)^2 + l^2} \approx \sqrt{2}l - \frac{\Delta x}{\sqrt{2}}, \tag{B.38}$$

$$= -\frac{1}{4}k\Delta x, \tag{B.39}$$

where only terms to first order in Δx have been kept. Summing these gives the horisontal force $-\frac{5}{4}k\Delta x$ on node 1, which corresponds to an effective stiffness $k_{\text{eff}} = \frac{5}{4}k$.

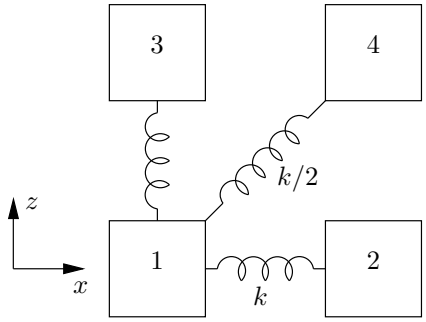

Figure B.2: The lower left corner of a 1+1D slider.

Appendix C

Additional remarks

C.1 Details of the implementation: stopping and starting of each block

As there is no randomness in my models, minor differences in roundoff error and the fine details of the implementation of the starting and stopping of each block become important to the exact details of figures like the lower panel of Figure 4.4. Here, I give the details of my implementation.

A block at the sliding interface is either pinned by static friction, slipping or not in contact with the track (the latter only happens in the 1+1D model), and I store the state of the block in a variable I call its sliding flag. The RK4 algorithm involves the calculation of intermediate or trial time steps, which require force calculations; the value of the sliding flag is important to these force calculations. *I only change the value of the sliding flags at the main time steps.*

At the beginning of a time step I calculate the net force on each block. The simplest case is if the net normal force is zero: then, no friction force acts on the block. If there is a net normal force, and the net shear force exceeds the static friction threshold, the block starts to slide. If, while sliding, the horizontal velocity of the block changes sign from one time step to the next, it stops sliding. It is allowed, in the final time step, to move back in the direction from which it came.

C.2 Code optimisation in 1D

This section discusses the runtime of the 1D models and how it can be reduced with no changes to the output.

C.2.1 Scaling of the computation time with N

Because of the way the stiffness of the interconnecting springs is defined, increasing N does not change the stiffness of the system as a whole. Neither does it change the total mass M. We would like to use a large N in order to get a good resolution, but increasing N means increasing the computation time.

Firstly, the computation time grows with N because of the increasing number of interactions. Since the system is one-dimensional and coupling is between nearest neighbours only, the number of force calculations in each loop scales linearly with N.

Secondly, the time step length has to be modified as the resolution is increased, and this increases the time by another factor of N, which can be seen as follows: In order for a numerical integration to capture the dynamics of the system, the time step length must be significantly shorter than the period of oscillations in the system. The scaling is obtained by considering the period T of a harmonic oscillator with mass m and stiffness k,

$$T = \frac{1}{\nu} = \frac{2\pi}{\omega} = 2\pi\sqrt{\frac{m}{k}} \tag{C.1}$$

$$= 2\pi\sqrt{\frac{M/N}{(N-1)EA/L}} \tag{C.2}$$

$$\sim \frac{1}{N}. \tag{C.3}$$

The computation time is therefore $O(N^2)$.

C.2.2 Skipping time steps where nothing interesting happens

The number of time steps needed to solve the 1D model on the computer is large because there exist different time scales in the problem. The shortest time scale, which determines the temporal resolution required to keep truncation errors in the integration algorithms acceptably small, is the period of oscillation of a single block, which to first approximation is $2\pi\sqrt{m/k}$. The long time scale is related to the driving speed V of the point P. For slow driving, the position X should stay roughly the same during each event. As a direct consequence of keeping these time scales separate, the number of time steps between events becomes large. Nothing interesting happens during these time steps, just a build up of force. By exploiting the fact that the first interesting time step (the first where a block moves) can be found analytically, the intervening force build-up period can be skipped entirely. Depending on the relation between the time scales, this can reduce the computation time dramatically; if there were a hundred times as many time steps between events as time steps resolving interesting dynamics, the computation time can be reduced to 1 percent.

The external spring force on a block i connected to the driving stage is (equations (4.4) and (4.27))

$$F_{X,i}(t) = \bar{K}_i(Vt - x_i), \tag{C.4}$$

where $\bar{K}_i = K/N$ if the system is driven from the top and $\bar{K}_1 = K, \bar{K}_{i\neq 0} = 0$ if the system is driven from the side. If $\mathcal{J}$ is the set of blocks that are connected to the driving stage the force on the driving stage is

$$F_X(t) = \sum_{j\in\mathcal{J}} F_{X,j}(t) = \sum_{j\in\mathcal{J}} \bar{K}_j(Vt - x_j) = Vt \sum_{j\in\mathcal{J}} \bar{K}_j - \sum_{j\in\mathcal{J}} \bar{K}_j x_j. \tag{C.5}$$

The force on block i from its neighbours remains constant during the force build up and can be denoted by $F_{S,i}(t_{\text{stop}})$. The static friction threshold is (equation (4.6)) $f^{(i)}_{s,\max} = \mu_s w_i$. The time $t^{(i)}_{\text{start}}$ of fracture of the ith contact is the solution of

$$F_{X,i}(t^{(i)}_{\text{start}}) + F_{S,i}(t_{\text{stop}}) = \mu_s w_i(t^{(i)}_{\text{start}}). \tag{C.6}$$

If a torque effect is included, the normal force w_i becomes time dependent. A more general form of equation (4.38) is

$$w_i(t) = w_0 + \frac{g}{N}\frac{2i - N - 1}{N - 1} F_X(t). \tag{C.7}$$

Here, w_0 is the static load, which could be asymmetric. Introducing the function $\text{lin ramp}(i, N) = \frac{2i-N-1}{N-1}$ and inserting $F_X(t)$ gives

$$w_i(t) = w_0 + \frac{g}{N}\,\text{lin ramp}(i, N) Vt \sum_{j\in\mathcal{J}} \bar{K}_j - \frac{g}{N}\,\text{lin ramp}(i, N) \sum_{j\in\mathcal{J}} \bar{K}_j x_j. \tag{C.8}$$

Using this and solving equation (C.6) for $t^{(i)}_{\text{start}}$ gives

$$\boxed{t^{(i)}_{\text{start}} = \frac{\mu_s w_0 + \bar{K}_i x_i - \mu_s \frac{g}{N}\,\text{lin ramp}(i, N) \sum_{j\in\mathcal{J}} \bar{K}_j x_j - F_{S,i}(t_{\text{stop}})}{\bar{K}_i V - \mu_s \frac{g}{N}\,\text{lin ramp}(i, N) V \sum_{j\in\mathcal{J}} \bar{K}_j}.} \tag{C.9}$$

Upon all blocks coming to rest one can immediately jump to the time

$$t_{\text{start}} = \min(t^{(i)}_{\text{start}}). \tag{C.10}$$

C.3 L_p–F_X for different h with $\mu_s = \mu_k$ in 1+1D

In Section 5.7 I showed that changing the pushing height h changed the number of precursors while the shape of the L_p–F_X curves stayed the same. This is observed experimentally, see Figure 5.13.

As h is increased, the curves start at increasing values of F_X/F_Z and of L_p/L; the first event occurs later and goes further. Setting $\mu_s = \mu_k$ as in Section 5.7.2 gives the curve in the whole range $L_p \in [0, 1]$. This is shown in Figure C.1. Note that the solid lines for $\mu_s = \mu_k$ show that the events trigger away from the trailing edge and that the slipping region then grows bilaterally. The figure indicates that if experiments are carried out on materials with μ_s closer to μ_k, the conservation of L_p–F_X with changes in h is likely to break down.

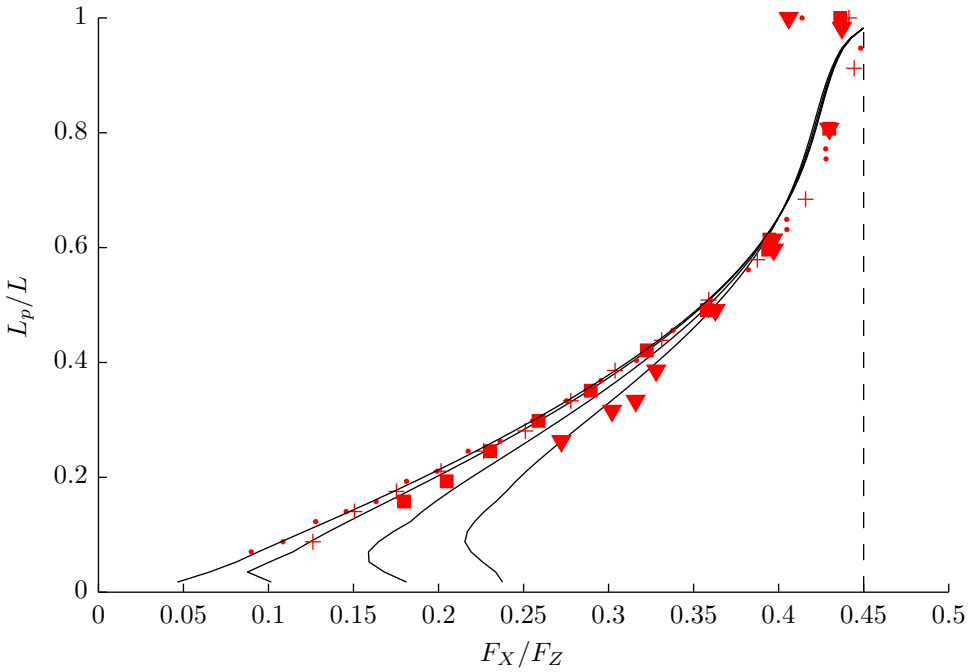

Figure C.1: When $\mu_s = \mu_k$, different h give different L_p–F_X shapes (drawn lines). Markers denote pushing heights $h = 2.5(\bullet)$, $5(+)$, $7.5(\square)$ and $15(\triangledown)$ mm for runs with $\mu_s = 0.7$, $\mu_k = 0.45$. (Note that the third drawn line from the left has $h = 10$ mm.) The dashed vertical line has the value of the local dynamic friction coefficient μ_k. $N_z = 31$, $k_{\text{ps}} = k$, $\Delta t = 2 \cdot 10^{-7}$ s, remaining parameters as II in Table 5.1. Top loading: spring mattress. F_X was measured at the arrest time of the events.

C.4 Anomalous crack front velocities in 1+1D

In Figure 5.31 of Section 5.10.1 I showed data collapse of the rupture front velocity v_{crack} for simulations with different values of normal load F_Z, sample length L, pushing height h and the friction coefficients μ_s and μ_k. Figure C.2, included for completeness, shows that the simulations also produce data that do not fit as well on the master curve as the data in Figure 5.31.

From detailed investigations of the deviations from the master curve, I find that they are associated with events triggered differently than the majority. The increase in v_{crack} at $\tau/\sigma \approx 0.4$ was seen in Figure 5.29 as well and explained by reflected waves, Figure 5.30. The complicated shapes at $\tau/\sigma \approx 0.5$ correspond to events triggered during the oscillations of the stress profiles discussed in Section 5.9.1, immediately after the arrest point of the preceding events. Because they are actually part of the relaxation of the preceding events, they should be excluded; however, finding a robust algorithm for identifying them is not trivial. Finally, the $v_{\text{crack}} \approx 0$ measurements are due to events initially arresting near the leading edge while still slipping at the trailing edge, and then a second wave reaching the right end; this makes the definition of $\Delta t^{\text{trigger}}$ in equation (5.39b) poor.

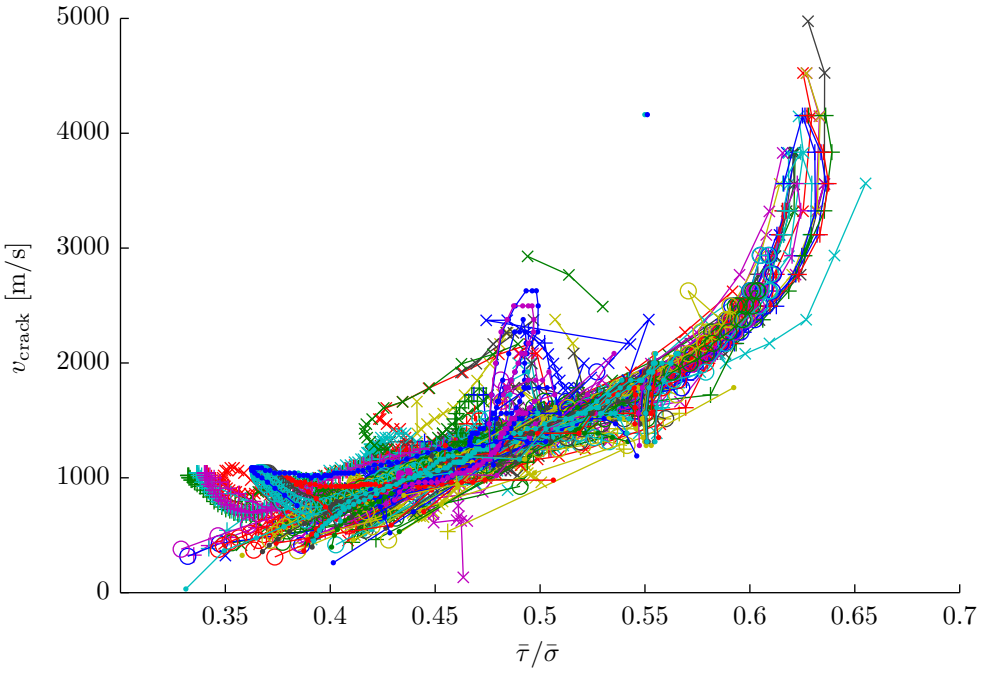

Figure C.2: Some rupture fronts deviate from the master curve. Data for four pushing heights $h = 2.5$ mm ($\times$), $h = 5$ mm ($+$), $h = 10$ mm ($\circ$) and $h = 12.5$ mm ($\cdot$), all from simulations with $N_z = 31$, $k_{\text{ps}} = k$, $\Delta t = 2 \cdot 10^{-7}$ s and remaining parameters as III in Table 5.1. Top loading: spring mattress.

Bibliography

[1] D. S. Amundsen. Modelling the onset of dynamic friction: A study of rupture velocities. Master's thesis, University of Oslo, Oslo, 2011.

[2] J. F. Archard. Elastic deformation and the laws of friction. *Proceedings of the Royal Society of London, Series A, Mathematical and Physical Sciences*, 243(1233):190–205, 1957. ISSN 00804630. URL `http://www.jstor.org/stable/100445`.

[3] P. Bak, C. Tang, and K. Wiesenfeld. Self-organized criticality: An explanation of the 1/f noise. *Phys. Rev. Lett.*, 59(4):381–384, July 1987. doi: 10.1103/PhysRevLett.59.381.

[4] T. Baumberger and C. Caroli. Solid friction from stick–slip down to pinning and aging. *Advances in Physics*, 55(3):279–348, 2006. ISSN 0001-8732. URL `http://www.informaworld.com/10.1080/00018730600732186`.

[5] T. Baumberger, C. Caroli, and O. Ronsin. Self-healing slip pulses along a gel/glass interface. *Phys. Rev. Lett.*, 88(7):075509, Feb. 2002. doi: 10.1103/PhysRevLett.88.075509.

[6] J. Behrendt, C. Weiss, and N. Hoffmann. A numerical study on stick-slip motion of a brake pad in steady sliding. *Journal of Sound and Vibration*, 330(4):636 – 651, 2011. ISSN 0022-460X. doi: 10.1016/j.jsv.2010.08.030. URL `http://www.sciencedirect.com/science/article/pii/S0022460X10005572`.

[7] O. Ben-David, G. Cohen, and J. Fineberg. The dynamics of the onset of frictional slip. *Science*, 330(6001):211–214, Oct. 2010. doi: 10.1126/science.1194777. URL `http://www.sciencemag.org/cgi/content/abstract/330/6001/211`.

[8] O. Ben-David, S. M. Rubinstein, and J. Fineberg. Slip-stick and the evolution of frictional strength. *Nature*, 463(7277):76–79, Jan. 2010. ISSN 0028-0836. doi: 10.1038/nature08676. URL `http://dx.doi.org/10.1038/nature08676`.

[9] R. Bennewitz, J. David, C.-F. de Lannoy, B. Drevniok, P. Hubbard-Davis, T. Miura, and O. Trichtchenko. Dynamic strain measurements in a sliding microstructured contact. *Journal of Physics: Condensed Matter*, 20(1):015004, 2008. URL `http://stacks.iop.org/0953-8984/20/i=1/a=015004`.

[10] B. Bhushan. History of tribology and micro/nanotribology. In Bhushan, Bharat, editor, *Micro/Nanotribology and Its Applications*, volume 330 of *NATO Advanced Science Institutes Series, Series E, Applied Sciences*, pages 1–16, Dordrecht, 1997. Kluwer Academic Publishers.

[11] E. Bouchbinder, E. A. Brener, I. Barel, and M. Urbakh. Cracklike dynamics at the onset of frictional sliding. *ArXiv e-prints*, Mar. 2011. URL `http://arxiv.org/abs/1103.3942v1`.

[12] F. P. Bowden and D. Tabor. *The Friction and Lubrication of Solids*. Clarendon Press, Oxford, 2001. First published 1950.

[13] W. F. Brace and J. D. Byerlee. Stick-slip as a mechanism for earthquakes. *Science*, 153(3739):990–992, 1966. ISSN 00368075. URL `http://www.jstor.org/stable/1719360`.

[14] O. M. Braun and M. Peyrard. Modeling friction on a mesoscale: Master equation for the earthquakelike model. *Phys. Rev. Lett.*, 100(12):125501, Mar. 2008. doi: 10.1103/PhysRevLett.100.125501.

[15] O. M. Braun and M. Peyrard. Master equation approach to friction at the mesoscale. *Phys. Rev. E*, 82(3):036117, Sept. 2010. doi: 10.1103/PhysRevE.82.036117.

[16] O. M. Braun and M. Peyrard. Dependence of kinetic friction on velocity: Master equation approach. *Phys. Rev. E*, 83(4):046129, Apr. 2011. doi: 10.1103/PhysRevE.83.046129.

[17] O. M. Braun and J. Röder. Transition from stick-slip to smooth sliding: An earthquakelike model. *Phys. Rev. Lett.*, 88(9):096102, Feb. 2002. doi: 10.1103/PhysRevLett.88.096102.

[18] O. M. Braun, I. Barel, and M. Urbakh. Dynamics of transition from static to kinetic friction. *Phys. Rev. Lett.*, 103(19):194301, Nov. 2009. doi: 10.1103/PhysRevLett.103.194301.

[19] R. Burridge and L. Knopoff. Model and theoretical seismicity. *Bulletin of the Seismological Society of America*, 57(3):341–371, 1967. URL `http://www.bssaonline.org/cgi/content/abstract/57/3/341`.

[20] J. M. Carlson and J. S. Langer. Mechanical model of an earthquake fault. *Phys. Rev. A*, 40(11):6470–6484, Dec. 1989. doi: 10.1103/PhysRevA.40.6470.

[21] J. M. Carlson, J. S. Langer, and B. E. Shaw. Dynamics of earthquake faults. *Reviews of Modern Physics*, 66(2):657–670, Apr. 1994. ISSN 0034-6861.

[22] A. Chateauminois, C. Fretigny, and L. Olanier. Friction and shear fracture of an adhesive contact under torsion. *Phys. Rev. E*, 81(2):026106, Feb. 2010. doi: 10.1103/PhysRevE.81.026106.

[23] D. Dawson. *History of Tribology*. Professional Engineering Publishing Limited, London and Bury St Edmunds, UK, second edition, 1998.

[24] J. H. Dieterich. Modeling of rock friction 1. Experimental results and constitutive equations. *J. Geophys. Res.*, 84(B5):2161–2168, 1979. ISSN 0148-0227. doi: 10.1029/JB084iB05p02161. URL `http://dx.doi.org/10.1029/JB084iB05p02161`.

[25] E. M. Dunham. Conditions governing the occurrence of supershear ruptures under slip-weakening friction. *Journal of Geophysical Research-Solid Earth*, 112(B7), July 2007. ISSN 0148-0227. doi: 10.1029/2006JB004717.

[26] S. Elliott. *The Physics and Chemistry of Solids*. Wiley, West Sussex, 1998.

[27] A. E. Filippov, J. Klafter, and M. Urbakh. Friction through dynamical formation and rupture of molecular bonds. *Phys. Rev. Lett.*, 92(13):135503, Mar. 2004. doi: 10.1103/PhysRevLett.92.135503.

[28] E. Fukuyama and R. Madariaga. Rupture dynamics of a planar fault in a 3d elastic medium: Rate- and slip-weakening friction. *Bulletin of the Seismological Society of America*, 88(1):1–17, 1998. URL `http://www.bssaonline.org/cgi/content/abstract/88/1/1`.

[29] E. Gerde and M. Marder. Friction and fracture. *Nature*, 413(6853):285–288, Sept. 2001. ISSN 0028-0836. doi: 10.1038/35095018. URL `http://dx.doi.org/10.1038/35095018`.

[30] H. Gould, J. Tobochnik, and W. Christian. *An Introduction to Computer Simulation Methods: Applications to Physical Systems*. Addison Wesley, San Fransisco, third edition, 2007.

[31] J. A. Greenwood and J. B. P. Williamson. Contact of nominally flat surfaces. *Proceedings of the Royal Society of London, Series A, Mathematical and Physical Sciences*, 295(1442):300–319, 1966. doi: 10.1098/rspa.1966.0242. URL `http://rspa.royalsocietypublishing.org/content/295/1442/300.abstract`.

[32] W. Humphrey, A. Dalke, and K. Schulten. VMD: Visual molecular dynamics. *Journal of Molecular Graphics*, 14(1):33 – 38, 1996. ISSN 0263-7855. doi: DOI: 10.1016/0263-7855(96)00018-5. URL `http://www.sciencedirect.com/science/article/B6VNC-3VJRDJX-5/2/247595492d1cae80b34bed4d649bf0b2`.

[33] L. Knopoff and X. X. Ni. Numerical instability at the edge of a dynamic fracture. *Geophysical Journal International*, 147(3):1–6, 2001. ISSN 1365-246X. doi: 10.1046/j.1365-246x.2001.01567.x. URL `http://dx.doi.org/10.1046/j.1365-246x.2001.01567.x`.

[34] L. Knopoff, J. O. Mouton, and R. Burridge. The dynamics of a one-dimensional fault in the presence of friction. *Geophysical Journal of the Royal Astronomical Society*, 35(1-3):169–184, 1973. ISSN 1365-246X. doi: 10.1111/j.1365-246X.1973.tb02420.x. URL `http://dx.doi.org/10.1111/j.1365-246X.1973.tb02420.x`.

[35] H. P. Langtangen. *Computational Partial Differential Equations: Numerical Methods and Diffpack Programming*. Springer, Berlin, second edition, 2002.

[36] S. Maegawa, A. Suzuki, and K. Nakano. Precursors of global slip in a longitudinal line contact under non-uniform normal loading. *Tribology Letters*, 38(3):313–323, June 2010. ISSN 1023-8883. doi: 10.1007/s11249-010-9611-7. URL `http://dx.doi.org/10.1007/s11249-010-9611-7`.

[37] C. Marone. Laboratory-derived friction laws and their application to seismic faulting. *Annual Review of Earth and Planetary Sciences*, 26:643–696, 1998.

[38] L. Monette and M. P. Anderson. Elastic and fracture properties of the two-dimensional triangular and square lattices. *Modelling and Simulation in Materials Science and Engineering*, 2(1):53, 1994. URL `http://stacks.iop.org/0965-0393/2/i=1/a=004`.

[39] C. B. Muratov. Traveling wave solutions in the Burridge–Knopoff model. *Phys. Rev. E*, 59(4):3847–3857, Apr. 1999. doi: 10.1103/PhysRevE.59.3847.

[40] Z. Olami, H. J. S. Feder, and K. Christensen. Self-organized criticality in a continuous, nonconservative cellular automaton modeling earthquakes. *Phys. Rev. Lett.*, 68(8):1244–1247, Feb. 1992. doi: 10.1103/PhysRevLett.68.1244.

[41] B. N. J. Persson. Theory of friction: The role of elasticity in boundary lubrication. *Phys. Rev. B*, 50(7):4771–4786, Aug. 1994. doi: 10.1103/PhysRevB.50.4771.

[42] B. N. J. Persson. Theory of friction: Stress domains, relaxation, and creep. *Phys. Rev. B*, 51(19):13568–13585, May 1995. doi: 10.1103/PhysRevB.51.13568.

[43] B. N. J. Persson. *Sliding Friction*. Springer, Berlin, 1998.

[44] W. H. Press, S. A. Teukolsky, W. T. Vetterling, and B. P. Flannery. *Numerical Recipes*. Cambridge University Press, New York, third edition, 2007.

[45] S. M. Rubinstein, G. Cohen, and J. Fineberg. Detachment fronts and the onset of dynamic friction. *Nature*, 430(7003):1005–1009, Aug. 2004. ISSN 0028-0836. doi: 10.1038/nature02830. URL `http://dx.doi.org/10.1038/nature02830`.

[46] S. M. Rubinstein, M. Shay, G. Cohen, and J. Fineberg. Crack-like processes governing the onset of frictional slip. *International Journal of Fracture*, 140: 201–212, 2006. ISSN 0376-9429. doi: 10.1007/s10704-006-0049-8. URL `http://dx.doi.org/10.1007/s10704-006-0049-8`.

[47] S. M. Rubinstein, G. Cohen, and J. Fineberg. Dynamics of precursors to frictional sliding. *Phys. Rev. Lett.*, 98(22):226103, June 2007. doi: 10.1103/PhysRevLett.98.226103.

[48] S. M. Rubinstein, G. Cohen, and J. Fineberg. Visualizing stick–slip: Experimental observations of processes governing the nucleation of frictional sliding. *Journal of Physics D: Applied Physics*, 42(21):214016, 2009. URL `http://stacks.iop.org/0022-3727/42/i=21/a=214016`.

[49] A. Ruina. Slip instability and state variable friction laws. *J. Geophys. Res.*, 88 (B12):10359–10370, 1983. ISSN 0148-0227. doi: 10.1029/JB088iB12p10359. URL `http://dx.doi.org/10.1029/JB088iB12p10359`.

[50] J. Scheibert and D. K. Dysthe. Role of friction-induced torque in stick-slip motion. *Europhysics Letters*, 92(5):54001, 2010. URL `http://stacks.iop.org/0295-5075/92/i=5/a=54001`.

[51] J. Scheibert, G. Debregeas, and A. Prevost. Micro-slip field at a rough contact driven towards macroscopic sliding. *ArXiv e-prints*, Sept. 2008. URL `http://arxiv.org/abs/0809.3188v1`.

[52] C. H. Scholz. *The Mechanics of Earthquakes and Faulting*. Cambridge University Press, Cambridge, second edition, 2002.

[53] Z. Shi, Y. Ben-Zion, and A. Needleman. Properties of dynamic rupture and energy partition in a solid with a frictional interface. *Journal of the Mechanics and Physics of Solids*, 56(1):5–24, Jan. 2008. ISSN 0022-5096. doi: 10.1016/j.jmps.2007.04.006.

[54] K. Thøgersen. Modeling the onset of dynamic friction: Contact mechanics. Master's thesis, University of Oslo, Oslo, 2011.

[55] S. P. Timoshenko and J. N. Goodier. *Theory of Elasticity*. McGraw-Hill, Singapore, third edition, 1970. First published 1934.

[56] J. Trømborg, J. Scheibert, D. S. Amundsen, K. Thøgersen, and A. Malthe-Sørenssen. Transition from static to kinetic friction: insights from a 2D model. *ArXiv e-prints*, May 2011. URL `http://arxiv.org/abs/1105.3325v1`.

[57] M. Urbakh, J. Klafter, D. Gourdon, and J. Israelachvili. The nonlinear nature of friction. *Nature*, 430(6999):525–528, July 2004. ISSN 0028-0836. doi: 10.1038/nature02750. URL `http://dx.doi.org/10.1038/nature02750`.

[58] F. Wu-Bavouzet, J. Cayer-Barrioz, A. Le Bot, F. Brochard-Wyart, and A. Buguin. Effect of surface pattern on the adhesive friction of elastomers. *Phys. Rev. E*, 82 (3):031806, Sept. 2010. doi: 10.1103/PhysRevE.82.031806.

[59] H. D. Young and R. A. Freedman. *University Physics*. Addison Wesley, San Francisco, eleventh edition, 2004.